Potential vegetation changes in the permafrost areas over the Tibetan Plateau under future climate warming

Rui Chen[1], Jan Nitzbon[2], Schneider von Deimling Thomas[1], Simone Maria Stuenzi[1], Ngai-Ham Chan[1], Julia Boike[3], and Moritz Langer[4]

[1]Alfred Wegener Institute, Helmholtz Centre for Polar and Marine Research
[2]Alfred Wegener Institute Helmholtz Centre for Polar and Marine Research
[3]Alfred-Wegener Institute
[4]Alfred Wegener Institute

April 23, 2024

Abstract

Permafrost degradation on the Tibetan Plateau is well-documented and expected to continue throughout this century. However, the impact of thawing permafrost on the distribution, composition, and resilience of vegetation communities in this region is not well understood. In this study, we combined a transient numerical permafrost model with machine learning algorithms to project the near-future thermal state of permafrost and vegetation (represented by the Normalized Difference Vegetation Index [NDVI]) changes under two contrasting climate pathways (Shared Socioeconomic Pathway 1–2.6 [SSP1–2.6] and SSP5–8.5). The contribution of climatic and terrestrial variables to vegetation evolution was quantified using ridge regression. By 2100, permafrost areas were expected to decrease by 21±4%, and 55±2% under the SSP1–2.6 and SSP5–8.5 scenarios, respectively, relative to the baseline period (2000–2018). Under the SSP1–2.6 scenarios, the mean annual ground temperature and active layer thickness were projected to fluctuate stably, while under the SSP5–8.5 scenarios, a significant increasing trend was anticipated. Satellite-based observations indicated an increasing trend of NDVI within the permafrost areas from 2000 to 2018 (0.01 per decade), mainly attributed to climatic factors. In the future, vegetation greenness was expected to possibly remain stable under SSP1–2.6 scenarios, whereas a rising trend was likely noted under SSP5–8.5 scenarios during 2019–2050, mainly controlled by the surface air temperature and liquid water content at the root zone during the growing season. Our modeling work provides a potential approach for investigating future vegetation changes and offers more possibilities to improve understanding of the interaction between soil-vegetation-atmosphere in cold regions.

Potential vegetation changes in the permafrost areas over the Tibetan Plateau under future climate warming

Rui Chen[1,2], Jan Nitzbon[1], Thomas Schneider von Deimling[1], Simone Maria Stuenzi[1], Ngai-Ham Chan[1], Julia Boike[1,2], and Moritz Langer[1,3]

[1]Permafrost Research Section, Alfred Wegener Institute Helmholtz Centre for Polar and Marine Research, Potsdam, Germany
[2]Geography Department, Humboldt-Universität zu Berlin, Berlin, Germany
[3]Department of Earth Sciences, Vrije Universiteit Amsterdam, Amsterdam, the Netherlands

Key Points:

- By 2100, the permafrost areas will thaw at 0.23 ± 0.04 and $0.60 \pm 0.02 \times 10^{6}\ km^2$ under SSP1–2.6 and SSP5–8.5, respectively.
- By 2050, NDVI in the permafrost areas likely stay stable under SSP1–2.6 scenarios and likely show a rising trend under SSP5–8.5 scenarios.
- Surface air temperature and liquid water content at the root zone are the dominant features affecting NDVI changes in the permafrost areas.

Corresponding author: Rui Chen, `rui.chen@awi.de`

Abstract

Permafrost degradation on the Tibetan Plateau is well-documented and expected to continue throughout this century. However, the impact of thawing permafrost on the distribution, composition, and resilience of vegetation communities in this region is not well understood. In this study, we combined a transient numerical permafrost model with machine learning algorithms to project the near-future thermal state of permafrost and vegetation (represented by the Normalized Difference Vegetation Index [NDVI]) changes under two contrasting climate pathways (Shared Socioeconomic Pathway 1–2.6 [SSP1–2.6] and SSP5–8.5). The contribution of climatic and terrestrial variables to vegetation evolution was quantified using ridge regression. By 2100, permafrost areas were expected to decrease by $21 \pm 4\%$, and $55 \pm 2\%$ under the SSP1–2.6 and SSP5–8.5 scenarios, respectively, relative to the baseline period (2000–2018). Under the SSP1–2.6 scenarios, the mean annual ground temperature and active layer thickness were projected to fluctuate stably, while under the SSP5–8.5 scenarios, a significant increasing trend was anticipated. Satellite-based observations indicated an increasing trend of NDVI within the permafrost areas from 2000 to 2018 (0.01 per decade), mainly attributed to climatic factors. In the future, vegetation greenness was expected to possibly remain stable under SSP1–2.6 scenarios, whereas a rising trend was likely noted under SSP5–8.5 scenarios during 2019–2050, mainly controlled by the surface air temperature and liquid water content at the root zone during the growing season. Our modeling work provides a potential approach for investigating future vegetation changes and offers more possibilities to improve understanding of the interaction between soil-vegetation-atmosphere in cold regions.

Plain Language Summary

About 40% of the Tibetan Plateau is underlain by permafrost, which has undergone significant degradation and is estimated to experience substantial thawing by the end of this century. The thawing permafrost has impacted vegetation growth. To date, it has not been clear how the Normalized Difference Vegetation Index (NDVI; representing vegetation) changes with climate warming and permafrost degradation. Here, we used a land surface model and machine learning algorithms to simulate future permafrost thermal regimes and variations in the NDVI for future growing seasons and assess the most important variables influencing NDVI variability. We found that permafrost areas were projected to shrink by $21 \pm 4\%$ under the SSP1–2.6 scenarios and $55 \pm 2\%$ under the SSP5–8.5 scenarios by 2100, compared to the baseline period (2000–2018). Our results suggested that under mild climate conditions (SSP1–2.6), NDVI in the permafrost areas likely remained stable from 2019 to 2050, while NDVI in the permafrost areas likely showed an increasing trend under harsh climate conditions (SSP5–8.5), which was mainly due to increasing surface air temperature and liquid water content at the root zone on the Tibetan Plateau.

1 Introduction

The Tibetan Plateau (TP; Figure 1) hosts the world's most extensive high-altitude permafrost areas, estimated at $1.15 \times 10^6\, km^2$ (2005–2015) (Ran et al., 2021). Previous studies showed that permafrost had undergone significant degradation due to anthropogenic warming (Smith et al., 2022; X. Wang et al., 2022; Baral et al., 2023), as evidenced by increased mean annual ground temperature (MAGT) (Q. Wu & Zhang, 2008; Zhao et al., 2021), increased active layer thickness (ALT) (Q. Wu & Zhang, 2010; Qin et al., 2017), reduced permafrost thickness and areas (D. Guo & Wang, 2013; Ran et al., 2018), and altered geomorphological features (T. Gao et al., 2021; Xia et al., 2022). According to state-of-the-art Earth System Models (ESMs), the mean annual surface air temperature over the TP is projected to rise by $1.9\,^{\circ}C$ under the Shared Socioeconomic Pathway 1–2.6 (SSP1–2.6) and by as much as $6.3\,^{\circ}C$ under SSP5–8.5 by the end of the

21st century, relative to the baseline period of 1981–2010 (R. Chen, Li, et al., 2022). Such warming is expected to exacerbate the thawing and warming of the permafrost. Compared to the baseline period (2006–2015), the MAGT and ALT are estimated to increase by $0.8\,^{\circ}C$ to $2.6\,^{\circ}C$ and $0.7\,m$ to $3.0\,m$, respectively, in the period 2091–2100 under the SSP2–4.5 to SSP5–8.5 scenarios (G. Zhang et al., 2022), corresponding with a decline in permafrost areas by 44% to 71% (G. Zhang et al., 2022). This degradation is expected to cause major impacts on the carbon budget (Mu et al., 2020; T. Wang et al., 2020), hydrological dynamics (Song et al., 2022; T. Wang et al., 2023), ecosystem (Cuo et al., 2022; T. Wang et al., 2022), and infrastructure stability (Ran, Cheng, et al., 2022; R. Chen et al., 2023) on the regional scale. Vegetation covers approximately 81 % of the permafrost areas on the TP, rendering it the predominant surface characteristic (Z. Wang et al., 2016). With methodological innovations, sophisticated models, and a surge in observational data, our understanding of permafrost–vegetation interactions is improving (Heijmans et al., 2022). On the one hand, vegetation significantly influences the hydrothermal regime, carbon, and nutrient dynamics in permafrost environments. This influence is exerted through alterations in the surface energy balance (Chang et al., 2015; Stuenzi, Boike, Cable, et al., 2021), regulation of snow cover dynamics (Lawrence & Swenson, 2011; Grünberg et al., 2020), and impacts on both ecosystem carbon uptake (Ding et al., 2017; D. Wei et al., 2021) and ecosystem respiration processes (Gagnon et al., 2019; Prager et al., 2020). On the other hand, the evolution of permafrost significantly affects vegetation patterns, either promoting greening or browning (Myers-Smith et al., 2020). This is primarily mediated by its control over soil temperature and liquid water content in the root zone (Yi et al., 2014; de Vrese et al., 2023), alterations in landscape morphology (van der Kolk et al., 2016; Mu et al., 2017; Loranty et al., 2018), impacts on microbial stability (M. Wu et al., 2021), and influences on carbon and nitrogen cycling processes (Mekonnen et al., 2018; L. Liu et al., 2022; Mauclet et al., 2022).

Continuous vegetation greening and enhanced carbon uptake were also observed on the TP along with climate warming and permafrost degradation since the 1980s (Teng et al., 2021; Cuo et al., 2022; Shi et al., 2023; Z. Jin et al., 2023; Y. Wang et al., 2023). Notably, the Normalized Difference Vegetation Index (NDVI) exhibited an upward trend of 0.011 per decade from 1982 to 2015 (Teng et al., 2021). Similarly, the Enhanced Vegetation Index (EVI; which was developed to optimize the vegetation signal with improved sensitivity in high-biomass regions) increased by 0.01 per decade from 2000 to 2020 (Shi et al., 2023), and the Net Primary Productivity (NPP) demonstrated a positive trend of $0.51\,g\,C\,m^{-2}$ per decade from 1982 to 2014 (Cuo et al., 2022). While many studies have identified warming temperatures and increasing precipitation to be the main drives of greening (Teng et al., 2021; X. Li et al., 2022; T. Wang et al., 2022) and plant phenology changes (Q. Zhang et al., 2018; M. Shen et al., 2022; T. Wang et al., 2022) across the TP, vegetation greening on the global scale is thought to be mainly induced by CO_2 fertilization (Piao et al., 2020). In addition to the climatic factors, the hydrothermal conditions of the permafrost would also affect the vegetation dynamics through the permafrost-vegetation interactions (J. Wang & Liu, 2022; T. Wang et al., 2022). All of these studies have significantly improved our understanding of the characteristics and drivers of the vegetation greenness on the TP. However, it is still largely unknown how the vegetation cover will evolve under further destabilizing permafrost conditions on the TP accounting for future climate scenarios at a larger spatial scale. This uncertainty persists since the very complex vegetation physiological processes which are often tied to specific local conditions are not yet well represented in generalistic ESMs (Piao et al., 2020). With machine learning approaches increasingly being used to analyze complex spatiotemporal data and explore future environmental change (Pearson et al., 2013; Nitze et al., 2018; J. Guo et al., 2023; C. Shen et al., 2023), coupling the model-based and data-driven methods allows us to deal with the complex permafrost-vegetation interactions and quantify the vegetation dynamics and its dominant factors under different climate scenarios.

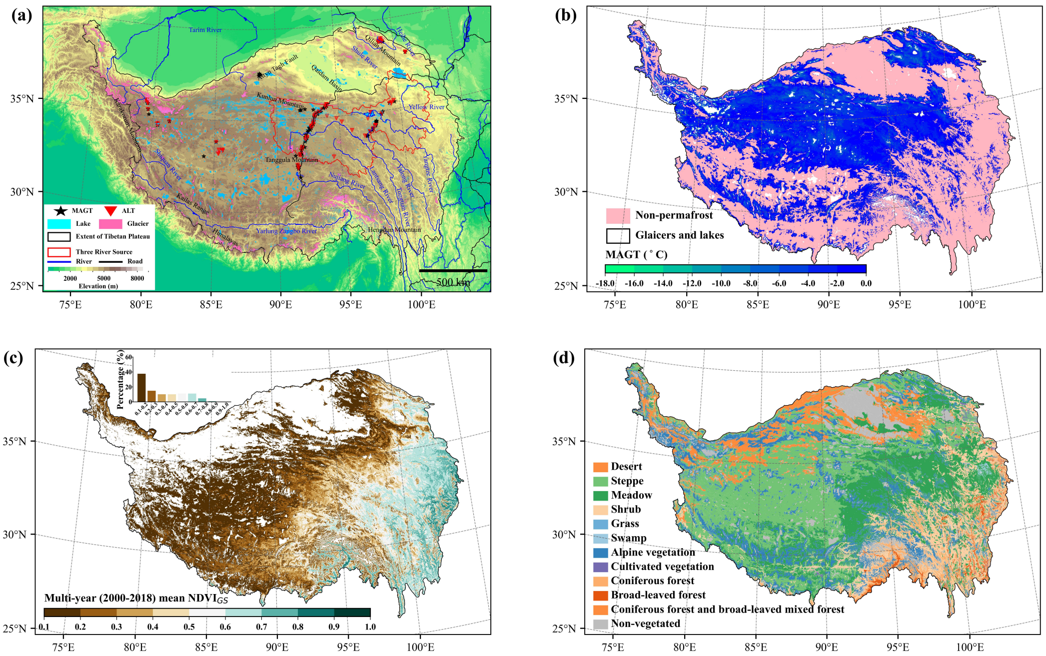

Figure 1. (a) Topography of study areas and location of observation sites over the Tibetan Plateau. Black stars and red triangles stand for the mean annual ground temperature (MAGT) and active layer thickness (ALT) of the monitoring sites, respectively. The digital elevation model, glacier, lake, river, and the boundary of the Tibetan Plateau data and the boundary of Three River Sources are obtained from the National Tibetan Plateau Data Center `https://data.tpdc.ac.cn` and are licensed under CC BY 4.0. The road data is available from the national 1:1000000 public basic geographic database of China (version 2017). (b) Spatial distributions of permafrost and non-permafrost areas on the Tibetan Plateau. Data source: (Obu et al., 2019). (c) Spatial distribution of the multi-year (2000–2018) mean of the growing season (May to September) NDVI on the Tibetan Plateau at 1km^2 scale from MODIS satellite imagery, the sub barplot represents the percentage of the number of grid cells of NDVI in each interval to the total number of grid cells. (d) Maps of vegetation types in the Tibetan Plateau adapted from the 1:1000000 vegetation map of China (Zhou et al., 2022)

In this study, we combined a physically-based permafrost model (CryoGridLite) (Langer et al., 2024) and machine-learning approaches for predicting the vegetation evolution (represented by the NDVI) over the permafrost areas on the TP. Firstly, we applied the CryoGridLite, driven by historical and future forcing datasets under the two different SSPs scenarios (SSP1–2.6 and SSP5–8.5) from two ESMs (AWI-CM-1-1-MR and MPI-ESM1-2-HR), to assess the potential shifts in permafrost distribution and its thermal state over the TP. Then, based on the output of the CryoGridLite model, we used machine-learning algorithms, which are Light Gradient Boosting Machine (LightGBM) (Ke et al., 2017) and Extreme Gradient Boosting Machine (XGBoost) (T. Chen & Guestrin, 2016), to quantify the prospective changes in NDVI within the permafrost areas of the TP. Finally, we elucidated the dominant factors influencing NDVI variations and quantified the contribution of each explanatory variable to the NDVI change.

2 Methods

2.1 CryoGridLite

We applied the one-dimensional transient permafrost model CryoGridLite (Langer et al., 2024) to simulate the trajectory of permafrost evolution over the TP. CryoGridLite was a fast version that was inherited from CryoGrid3 (Westermann et al., 2016) and the CryoGrid community model (Westermann et al., 2023), reducing computational costs and thus making it more suitable for regional (e.g., TP) to hemispherical scale (e.g., Pan-Arctic; Nitzbon et al. (2023)) permafrost modeling. In the following, we briefly describe the main aspects of CryoGridLite and provide the model setup for this work. Further detailed descriptions of model structures and physical processes can be found in Langer et al. (2024).

2.1.1 Model description

In this tailored version of CryoGridLite, we implemented the surface energy balance module, which was driven by the time series of forcing data (i.e. surface air temperature ($^\circ C$), rainfall and snowfall rate ($m\,h^{-1}$), ($kg\,kg^{-1}$), surface air pressure (Pa), incoming shortwave and longwave radiation ($W\,m^{-1}$), and wind ($m\,s^{-1}$)), to provide the upper boundary condition of the model (detailed description can be seen in Supporting Information Text S1.1). Unlike the heat condition equation implemented in CryoGrid3, the CryoGridLite used enthalpy instead of temperature as the state variable to solve the one-dimensional subsurface heat transfer:

$$\frac{\partial H}{\partial t} - \frac{\partial}{\partial z}(k(z,T)\frac{\partial T(H)}{\partial z}) = 0 \tag{1}$$

where $H\,(J\,m^{-3})$ is the volumetric enthalpy including sensible and latent heat contents of the ground, $t\,(s)$ is time, $z\,(m)$ is the vertical subsurface depth, $k\,(z,T)(W\,m^{-1}\,K^{-1})$ is the effective thermal conductivity derived from volumetric soil fractions of mineral, organic, water, ice and air in a given soil depth, and $T\,(k)$ is the ground temperature. The lower boundary condition was defined by constant geothermal heat flux. The implemented snowpack scheme allowed the model to simulate snow accumulation, ablation, melt-water routing, and refreezing within the snow cover. Once the snow had filled the first grid cell above the soil surface, the surface albedo changed from that of the soil to that of the fresh snow and decreased over time towards that of the albedo of old snow (Westermann et al., 2016). Besides, we applied a simple bucket scheme (a detailed description can be seen in Supporting Information Text S1.2) with only downward vertical water flow driven by gravity to compute the dynamics of soil water content rather than constant water contents used in (Langer et al., 2024).

2.1.2 Model setup

In this study, we synthesized the China Meteorological Forcing dataset (CMFD; selected period: 1979–2018 to represent historical climate conditions; resolution: 3 hours and $0.1^\circ \times 0.1^\circ$) (He et al. (2020); `https://www.tpdc.ac.cn`), along with two ESMs from CMIP6 (AWI-CM-1-1-MR and MPI-ESM1-2-HR; selected period: 2019–2100 to portray future climate conditions; resolution: monthly and $0.9375^\circ \times 0.9375^\circ$) (Müller et al. (2018); Semmler et al. (2020); `https://esgf-data.dkrz.de`) following the two SSP scenarios (SSP1–2.6 and SSP5–8.5) to construct the completely forcing data (period: 1979–2100; resolution: hourly and $0.1^\circ \times 0.1^\circ$). Compared with other ESMs, AWI-CM-1-1-MR, and MPI-ESM1-2-HR presented the best performance in depicting the spatiotemporal patterns of mean annual and seasonal surface air temperature on the TP in the past decades (R. Chen, Li, et al., 2022). To ensure model stability and consistency of the forcing data from 1979 to 2100, we performed a linear interpolation on the CMFD data from a 3-hour to an hourly resolution. Further, we utilized the approach from Westermann et al. (2016) by combining baseline climate data (from CMFD) with monthly climate anomalies (from ESMs) to generate the forcing data for this study. The time series of all forcing variables under the two SSPs and two ESMs for the period 1979–2100 is shown in Supporting Information Figure S1.

For the soil domain of the model, the vertical resolution of grid cells increased with thickness from the soil surface (0m) to the lower boundary of the model (100m) (0.02m in 0–2m depth; 0.05m in 2–4m depth; 0.1m in 4–10m depth; 0.2m in 10–20m depth; 1m in 20–30m depth; 5m in 30–50m depth; 10m in 50–100m depth). The soil stratigraphies were specified as mineral, organic, initial water/ice, and air volumetric fractions. The initial water/ice content according to Langer et al. (2023) was assumed halfway between field capacity and porosity for the soil layer above the water table depth, which was provided by a global groundwater table depths product (Fan et al. (2013); `https://thredds-gfnl.usc.es/thredds/catalog/GLOBALWTDFTP/catalog.html`), and saturated with the soil layer below the water table depth. The soil properties were derived from a new version of the global high-resolution dataset of soil hydraulic and thermal parameters dataset for land surface modeling (Y. Dai, Xin, et al. (2019); Y. Dai, Wei, et al. (2019); `https://globalchange.bnu.edu.cn`). The spatial resolution of this dataset was 0.00833° covering from 90°N to 90°S, 180°W to 180°E, and the vertical soil profile was provided in 8 layers (0–0.0451m, 0.0451–0.0906m, 0.0906–0.1655m, 0.1655–0.2891m, 0.2891–0.4929m, 0.4929–0.8289m, 0.8289–1.3828m and 1.3828–3.8019m). This dataset directly provided the volumetric fraction of soil organic matter and soil porosity. At the same time, mineral content and field capacity were calculated based on the approach in Y. Dai et al. (2013); Y. Dai, Xin, et al. (2019); Y. Dai, Wei, et al. (2019). Besides, we assumed the soil stratigraphy from 3.8019m to the bedrock depth Yan et al. (2020) was the same as that of the soil layer above it (i.e.1.3828–3.8019m). Below the bedrock depth, we assumed no soil organic matter existed, the soil porosity was arbitrarily set to 0.1, and the soil mineral content was set to 0.9. We utilized the geothermal gradient (0.031$^\circ C\,m^{-1}$; Y. Pang et al. (2022)) to interpolate the four-layer ERA5Land soil temperature (Muñoz-Sabater et al., 2021) in January 1979 to the whole soil profile as the initial ground temperature profile. The constant geothermal heat flux was extracted from the Terrestrial Heat Flow Dataset Lucazeau (2019) to describe the lower boundary condition.

To depict snowpack dynamics over time, five empty grid cells were set above the soil surface in the initial state to represent the maximum snow depth of 0.1m with a vertical resolution of 0.02m (Orsolini et al., 2019). We assumed a constant snow density (150 $\mathrm{kg\,m^{-3}}$) across the snowpack (L. Dai et al., 2018; Yin et al., 2021) and the fresh snow albedo was set to 0.82 (W. Wang et al., 2020). The parameters used in this study for model setup are summarized in the Supporting Information Table S1. We applied nearest-neighbor interpolation for all input datasets (detailed information is provided in Table 1) and further masked them with shape files of the boundary (Y. Zhang et al. (2014); `https://www.geodoi.ac.cn`), glaciers (W. Guo et al. (2015); `https://www.tpdc.ac.cn`), and lakes (G. Zhang et al. (2019); `https://www.tpdc.ac.cn`) of the TP to finalize the model setup for each grid cell in our simulations.

2.2 Machine learning model

In this study, we adopted two regression-based machine learning approaches to project the future NDVI change on the permafrost areas over the TP, which have been widely used in the prediction of future climate as well as environmental variables (Ukkonen & Mäkelä, 2019; Kondylatos et al., 2022; F. Chen et al., 2023; Veigel et al., 2023; C. Chen et al., 2024). The NDVI was collected from the Moderate Resolution Imaging Spectroradiometer (MODIS; MOD13A2; Didan (2015)) with a 1km spatial resolution from 2000–2018 to match up the period of CMFD and be regarded as the baseline period in this study. We processed the raw NDVI data to aggregate them into monthly intervals, which was the time resolution used in our machine learning approaches, using the maximum value composition approach (G. Pang et al., 2022) and further applied a Savitzky-Golay

Table 1. Overview of datasets used in this study

Datasets	Variable/Parameter	Reference/Source	Comments
China Meteorological Forcing Dataset	meteorological forcing	He et al. (2020)	Historical forcing 1979–2018
AWI-CM-1-1-MR MPI-ESM1-2-HR	meteorological forcing	Semmler et al. (2020) Müller et al. (2018)	Future forcing 2019–2100
Global high-resolution dataset of soil hydraulic and thermal parameters	Volumetric fractions of mineral, organic, porosity, and field capacity	Y. Dai, Xin, et al. (2019) Y. Dai, Wei, et al. (2019)	Soil stratigraphy
Global watertable depth dataset	Watertable depth	Fan et al. (2013)	Used to determine initial water/ice content
Terrestrial Heat Flow Dataset	Geothermal heat flux	Lucazeau (2019)	Lower boundary conditions
A Global Depth to Bedrock Dataset for Earth System Modeling	Bedrock depth	Yan et al. (2020)	Used to constrain soil depth
ERA5-Land	Four-layer soil temperature	Muñoz-Sabater et al. (2021)	Initial soil temperature
MODIS NDVI (MOD13A2, Version 6.1, 1km spatial resolution)	NDVI	Didan (2015)	Vegetation condition
Vegetation map from a digitized 1:1000000 vegetation atlas of China	Vegetation types	Zhou et al. (2022)	Analyzing NDVI changes and driving factors across various vegetation types

filter to smooth the NDVI time series (T. Wang et al., 2022). In addition, we assumed that there was no vegetation in the area with a multi-year (2000–2018) average growing season NDVI (from May to September, $NDVI_{GS}$; Teng et al. (2021)) lower than 0.1 (T. Wang et al., 2022). The spatiotemporal trend of $NDVI_{GS}$ over the TP (excluding the non-vegetation areas) from 2000 to 2018 based on the MODIS dataset is shown in the Supporting Information Figure S2. We incorporated six variables as explanatory factors in the machine-learning model based on previous studies (J. Wang & Liu, 2022; T. Wang et al., 2022; Y. Wang et al., 2023). Among them, surface air temperature (SAT), total precipitation (PRE), and incoming shortwave radiation (SIN) originated from climate-forcing data. Furthermore, the soil temperature (ST) and liquid water content (LWC) at the root zone (0–20cm; T. Wang et al. (2022)), and ALT are derived from the output of the CryoGridLite model for each grid cell. The time interval of these six variables was monthly, corresponding with the temporal resolution of the NDVI. The flow of the machine learning approach was as follows: First, the MODIS NDVI dataset and six explanatory variables that correspond with the same grid cell were divided into two groups: data from 2000 to 2014 served as the training dataset (about 80% of the data), and the remaining data (2015–2018) as the testing dataset (about 20% of the data). Then, according to the results from the CryoGridLite in the baseline period, we constructed the training and testing datasets on permafrost and non-permafrost areas (excluded ALT). For tuning the hyperparameters of each machine learning model in the training dataset in each area, we used Bayesian optimization (Python; Optuna package) with 500 iterations and set the early stopping and pruning strategy. The range of possible values for the part of hyperparameters and the final best hyperparameters can be seen in the Supporting Information Table S2. In each iteration, we used mean squared error as a scoring criterion and performed 5-fold cross-validation using the TimeSeriesSplit (Python; Scikit-learn package) approach due to there being a time dependence within the NDVI data. The optimal model parameter combinations resulting from each iteration were recorded and utilized to train the final model. Moreover, we introduced a weighting parameter for each model to enhance the model's emphasis on the growing season $NDVI_{GS}$ associated with individual grid cells. In comparison to the monthly NDVI values, our preference was for the model to exhibit superior performance when modeling the $NDVI_{GS}$ value. Similar to the hyperparameters used for each model, this weighting parameter was employed to obtain the optimal solution during the Bayesian optimization process. To evaluate the performance of each model, we employed root mean squared error (RMSE), bias (BIAS), coefficient of determination (R^2), and Kling-Gupta efficiency (KGE; Gupta et al. (2009)) as the evaluation metrics.

$$RMSE = \sqrt{\frac{1}{N}\sum_{i=1}^{N}(S_i - O_i)^2} \tag{2}$$

$$BIAS = \frac{1}{n}\sum_{i=1}^{n}(S_i - O_i) \tag{3}$$

$$R^2 = 1 - \frac{\sum_{i=1}^{n}(S_i - O_i)^2}{\sum_{i=1}^{n}(O_i - \bar{O})^2} \tag{4}$$

$$KGE = 1 - \sqrt{(r-1)^2 + \left(\frac{S}{O} - 1\right)^2 + \left(\frac{\sigma_S}{\sigma_O} - 1\right)^2} \tag{5}$$

where N is the number of validation data, S_i and $O_i (i = 1, 2, ..., N)$ are the values of simulated and observed data, respectively, S and O are the mean values of simulated and observed data, respectively, r is the Pearson correlation coefficient, σ_S, and σ_O are the standard deviations of simulated and observed data, respectively. We utilized the optimal machine learning model and future explanatory data to produce the NDVI for each grid cell within the permafrost and non-permafrost region over the TP.

2.3 Statistical analysis

We employed three indices including the MAGT ($^{\circ}C$), ALT (m), and permafrost areas (km^2) to quantify permafrost degradation. In this study, we obtained the MAGT from the depth of zero annual amplitude, which was typically at the 10–15m soil depth on the TP (Q. Wu & Zhang, 2010; Qin et al., 2017). We defined a grid cell as permafrost if its MAGT lies below the 0°C isotherm at the specific year (Ran, Li, et al., 2022). The ALT was quantified as the maximum thaw depth within the upper 10m of the subsurface (Langer et al., 2024) and there is no existing ALT and permafrost when the MAGT exceeds 0°C at the specific year at a grid cell. We employed the Albers Equal Area projection for area calculations to accurately represent permafrost areas. To better track the dynamics of vegetation conditions across the permafrost and non-permafrost areas on the TP, we used the annual NDVI_{GS} to represent the vegetation at individual years for each grid cell. In this study, we used ridge regression to robustly estimate the individual contributions of explanatory variables (mean or sum value at the growing season, i.e. SAT_{GS}, PRE_{GS}, SIN_{GS}, ST_{GS}, LWC_{GS}, and ALT_{GS}) to the variability in annual NDVI_{GS} across the permafrost and non-permafrost region (T. Wang et al., 2022; J. Li et al., 2023). This approach effectively mitigated the issue of multicollinearity inherent among the predictors. The incorporation of a regularization penalty term (λ) served to apportion variance across the coefficients efficiently, thereby enhancing the precision of the estimated impacts of the explanatory variables on NDVI_{GS}. Preceding the regression analysis, standardized explanatory variables and corresponding NDVI_{GS} served as inputs for the ridge regression model. The optimal regularization parameter, λ, was systematically determined through 5-fold cross-validation and the Grid Search algorithm, ensuring the most robust model performance. Variables exhibiting the largest absolute values of the regression coefficients post-regularization were interpreted as the dominant factors influencing NDVI_{GS} within the specific grid cells. A comprehensive range of the λ values explored during the model tuning phase was from 1×10^{-6} to 1×10^{6}. Besides, trend estimations of time series in this study were based on Sen's slope, which was selected over linear regression for its robustness against outliers and its nonparametric nature (Y. Wang et al., 2023). The flowchart of this study is shown in Figure 2.

3 Results

3.1 Model evaluations

3.1.1 CryoGridLite

For this study, we synthesized observational data, including MAGT and ALT, from a range of literature and public resources across the TP to assess the effectiveness of the CryoGridLite model (Q. Wu et al., 2020; H. Chen et al., 2015; J. Chen et al., 2016; Qin et al., 2017; Luo et al., 2018; Z. Zhang et al., 2020; Zhao et al., 2021; Mu & Peng, 2022; Y. Gao et al., 2023). Ultimately, we selected a total of $n_{MAGT} = 84$ and $n_{ALT} = 66$ different grid cells comprising 151 MAGT and 86 ALT data records within various permafrost regions of the TP from 2000 to 2015 in our model domain (Detailed information see Supporting Information Table S3). Figure 1 (a) displays the geographical distribution of these sites across the TP. For MAGT, we utilized the model output at the depth closest to the measured for comparison while for ALT, we considered the annual maximum thaw depth to compare the observed. Our modeling results indicated the simulated MAGT at most sites (53.6 %) in the range of $\pm\,1^{\circ}\,C$ of the observed value (Figure 3 (a)), and there was a positive correlation between simulated and observed MAGT (Pearson correlation coefficient = 0.46, $p < 0.01$). However, we noted that our model tended to underestimate observed MAGT across the TP (Bias = -0.77 $^{\circ}\,C$), which could be attributed to inaccuracies of forcing, soil stratigraphy dataset, and imitated processes representation (Langer et al., 2024) and setting for the maximum snow height (0.1m). Overall, our model displayed the ability to reproduce the MAGT in the TP permafrost

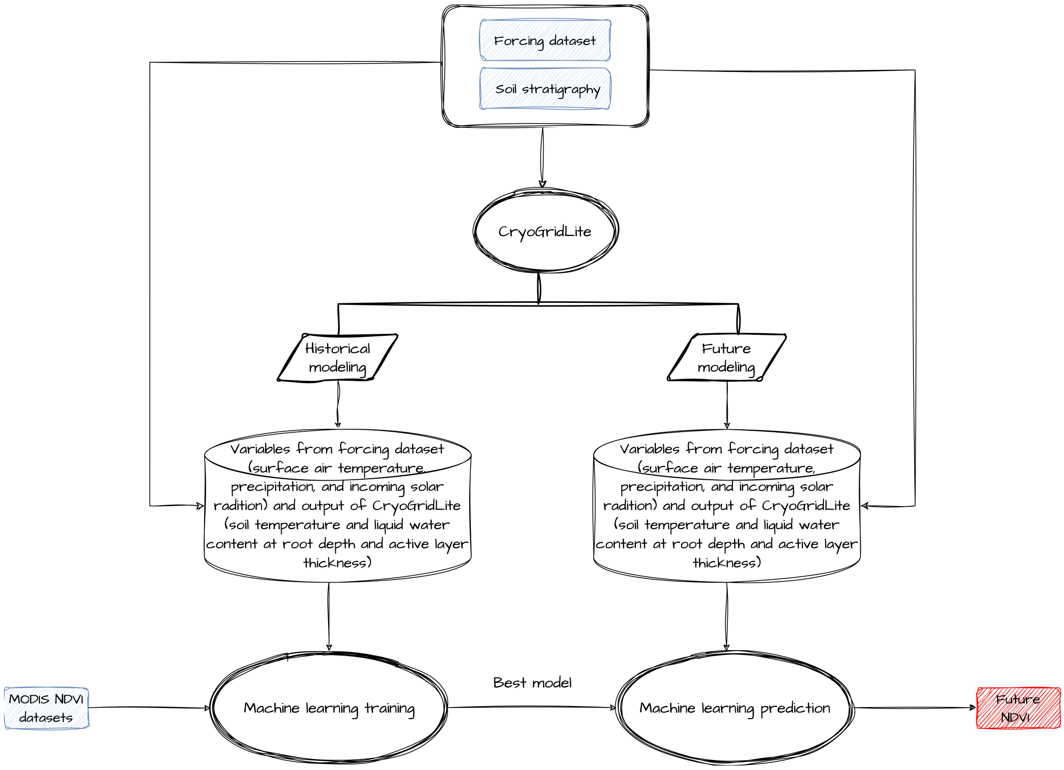

Figure 2. Flowchart of the process used to estimate the future vegetation change

areas well. Compared with the model capability on the MAGT, there was a poorer relationship between simulated and observed ALT, with a Pearson correlation coefficient of 0.17 (Figure 3 (b)). Similarly, the model exhibited a trend of underestimating the measured ALT compared to the observed values (Bias = -0.03 m), which aligns with the simulated cold bias for MAGT. The deviations between measured and modeled ALT were likely to be explained by inadequate forcing and soil dataset, shortcomings of the model (Langer et al., 2024), the cooling effect of shallow snow cover (0.1m), and high spatial heterogeneity of ALT on the TP (B. Cao et al., 2017; Ni et al., 2021). Nevertheless, our model reproduced the observed ALT on the TP, with modeled ALT deviations of $\pm 1\,m$ for most sites (59.1 %). A more detailed model evaluation was conducted for the soil temperature at upper soil depth across the TP due to the soil temperature at the root zone as an input index in machine learning (see Supporting Information Table S4 and Figure S3). In this research, CryoGridLite, driven by CMFD data, was employed to model the distribution of permafrost across the TP during the historical period (Figure 3 (c)). To demonstrate the capability of CryoGridLite to reproduce spatial permafrost occurrence, we juxtaposed our simulation results with five contemporary maps of permafrost distribution based on different approaches, thereby providing a comprehensive comparison and validation of our modeling results (Zou et al. (2017); Ran et al. (2018); Obu et al. (2019); Ni et al. (2021); Z. Cao et al. (2023); Figure 3 (d-h)). The comparison largely confirmed that the projected area of permafrost was consistent between our results and those of previous studies. Our modeling results indicated that the most likely permafrost areas on the TP were $1.10 \times 10^{6}\,km^2$ for the period 2000–2018 (excluding lakes and glaciers), which agreed well with other five studies (1.04–$1.28 \times 10^{6}\,km^2$). However, local differences were found between our results and other permafrost maps, which were most pronounced in the southern TP and along the southeast margin of the zone of continuous permafrost. It can be explained in several parts, first, spatial resolution and study period differences; lower resolutions (i.e., 0.1 °) make it difficult to capture the dynamics of permafrost changes at the boundaries of permafrost zones (Ni et al., 2021) and study period leads a slight discrepancy for the modeled results. Second, simulated approach differences; our results offer a dynamic, transient modeling perspective. In contrast, other models, such as the temperature at the top of the permafrost model and the surface frost number model, while simpler and requiring less data input, are not as equipped to capture transient effects or to project the evolution of permafrost accurately (Smith et al., 2022). Besides, the permafrost-modeled results of the machine learning model have data dependence and the risk of overfitting (Ni et al., 2021). Third, the definition of permafrost differences; we diagnose the absence or presence of permafrost relying on the MAGT at the zero depth of annual amplitude. Other studies adopt different criteria to determine the permafrost exists (e.g., the MAGT at the top of permafrost or the $10\,m$ depth). In summary, despite limitations our model provides a reasonable basis for describing spatially and temporally transient conditions of permafrost on the TP as input variable for the following analysis.

3.1.2 Machine learning model

We utilized the pre-partitioned test dataset to evaluate the performance of two machine-learning algorithms in modeling the NDVI_{GS} over the permafrost and non-permafrost areas of the TP (Figure 4). A comparison analysis of the two results (Figure 4 (a-b)) revealed that each algorithm proficiently captured the satellite-derived NDVI_{GS} values on the permafrost areas. The performance metrics (with $\mathrm{R}^2 >= 0.65$, $\mathrm{BIAS} <= 0.01$, $\mathrm{RMSE} <= 0.08$, and $\mathrm{KGE} >= 0.59$) suggested each model demonstrated robust capabilities in capturing the NDVI_{GS} dynamics over the permafrost regions of the TP. In comparison, the LightGBM model has better performance. Consequently, we selected the lightGBM model for further analysis of the spatial and temporal variability of NDVI_{GS} and its underlying drivers under different future climate scenarios. Additionally, complimentary assessments conducted for NDVI_{GS} over the non-permafrost areas underscored the simulation ability of both algorithms were remarkably similar and both can well repeat the changes in NDVI_{GS} (Figure 4 (c-d)).

3.2 Spatial and temporal patterns of the permafrost dynamics on the TP

To elucidate the spatiotemporal dynamics of permafrost variability on the TP throughout this century, we executed four distinct simulations driven by the AWI-CM-1-1-MR (Figure 5) and MPI-ESM1-2-HR (Supporting Information Figure S4) models, under both the SSP1–2.6 and SSP5–8.5 scenarios. Our findings revealed that spatial variability of permafrost distribution under the AWI-CM-1-1-MR, particularly by mid-century (2041–2060), manifested as a moderate reduction relative to the baseline period (2000–2018). This reduction was predominantly observed along the northern boundary of the continuous permafrost zone, southern regions of the TP, and the Three Rivers Sources (TRS) region (the red box in Figure 1 (a)), with negligible disparities between the lower and higher emission pathways (Figure 5 (a, c, e, g)). In contrast, by the end of the century (2081–2100), the majority of the permafrost areas were projected to remain relatively intact under SSP1-2.6, while areas that experienced permafrost thaw by mid-century continued to show visible degradation (Figure 5 (b, f)). Under a scenario of intensified climate warming, substantial thawing of existing permafrost was anticipated, particularly in the southwestern and southern parts of the TP, where the MAGT at the depth of zero annual amplitude was likely to approach or even exceed $0\ ^\circ C$ (Figure 5 (d, h)). The TRS region, in particular, was expected to undergo extensive permafrost degradation. Conversely, the northwestern areas of the Changtang Plateau and the Qilian Mountains were projected to maintain their permafrost coverage (Figure 5 (d, h)). In examining the projected changes in MAGT under the AWI-CM-1-1-MR, significant spatial heterogeneity

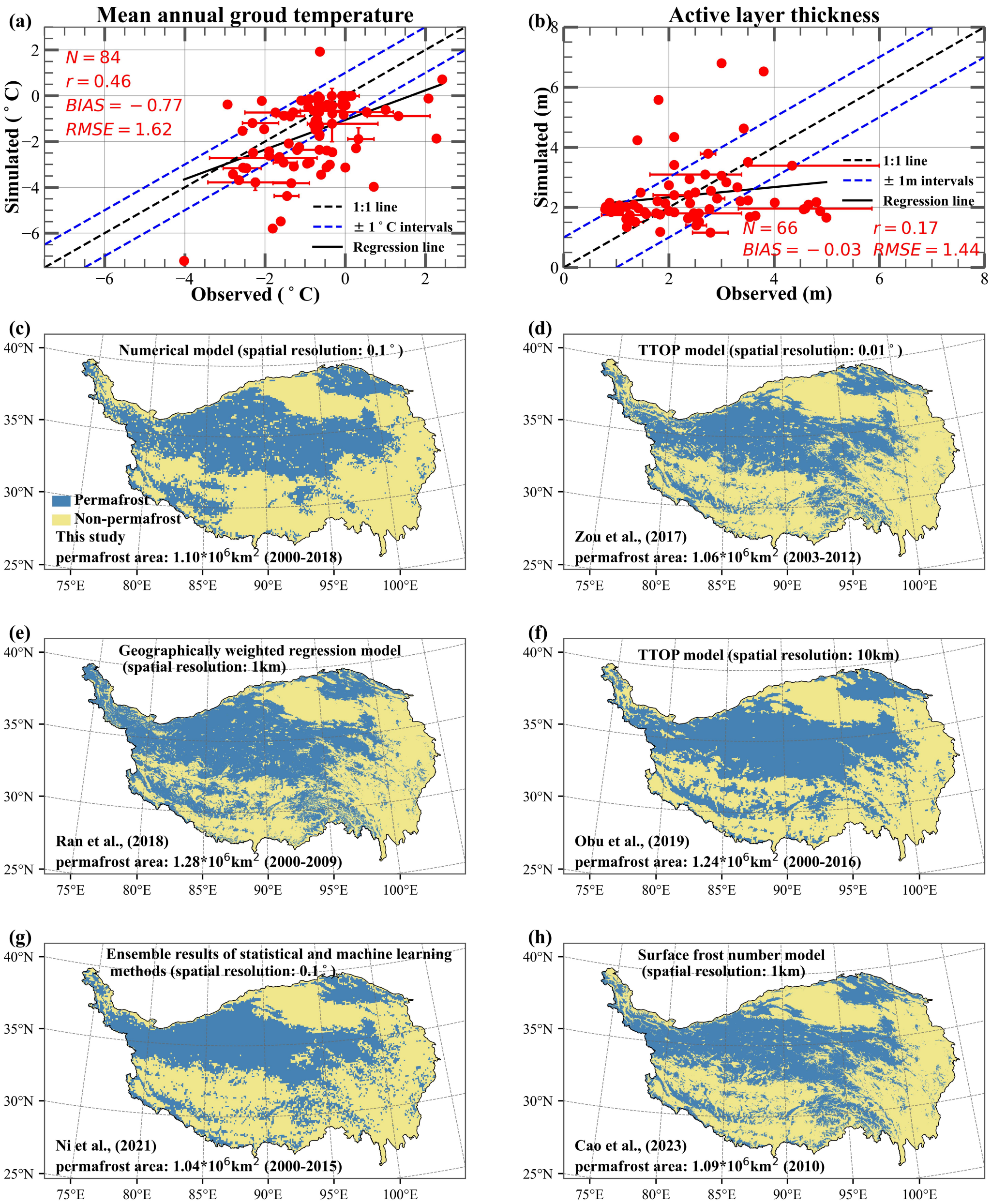

Figure 3. (a) Scatter plot illustrates the comparison results between the observed and simulated mean annual ground temperature (MAGT) for 151 records located within 84 different grid cells. (b) Scatter plot compares the observed and modeled active layer thickness (ALT) for 86 records located within 66 different grid cells. (c) Spatial distribution of permafrost during 2000–2018 over the Tibetan Plateau based on CryoGridLite model. (d-h) Spatial distribution of permafrost on the Tibetan Plateau from other studies. In (a) and (b), each point indicates the average value of observed and modeled MAGT/ALT in the same grid cell. The horizontal error bars represent the range of all observed MAGT/ALT located in the same grid cell, and vertical error bars indicate the range of simulated MAGT/ALT in the same grid cell.

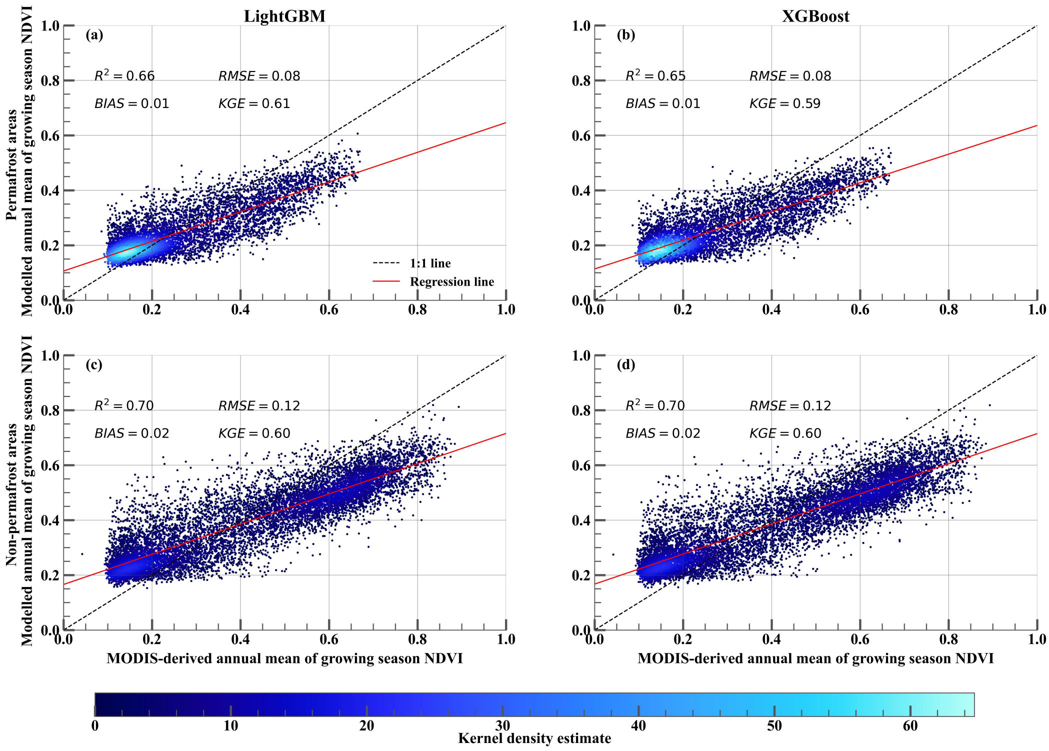

Figure 4. Density scatter plot for comparison between observed and modeled mean annual $NDVI_{GS}$ in the permafrost and non-permafrost areas from 2015 to 2018. (a, c) LightGBM, (b, d) XGBoost. The black dashed line indicates a 1:1 line. The red line represents the regression line.

was observed across the permafrost regions. Under the SSP1–2.6 scenarios, this variability contrasted with the SSP5–8.5 scenarios; specifically, the eastern permafrost regions were trending warmer, whereas the central Changtang Plateau and the Pamir Mountains experiencing cooling trends (Figure 5 (a-b)). The future dynamics of MAGT in these permafrost areas were expected to be largely influenced by the extent of climatic warming (Figure 5 (c-d)). Figure 5 (e-h) depicts the changes in ALT across the permafrost areas on the TP under the AWI-CM-1-1-MR for both mid-century and end-century, under two contrasting scenarios, relative to the 2000–2018 baseline period. The pattern of ALT changes mirrored that of MAGT, with a notable increase in ALT observed in the TRS region and along the Qinghai-Tibet Engineering Corridor (QTEC), throughout the century under both scenarios. Therefore, additional actions are needed to maintain the stability of infrastructure in the QTEC in the future. However, in the western TP, the evolutionary trajectory of ALT was contingent upon the extent of climate warming, i.e. ALT was likely to decrease under stable climatic conditions, while it tended to increase in scenarios of ongoing climate warming. The spatial distribution of MAGT, ALT, and permafrost areas under both scenarios under the MPI-ESM1-2-HR was in correspondence with the results from AWI-CM-1-1-MR (Supporting Information Figure S4).

We further detected the time evolution of permafrost areas, MAGT, and ALT across the TP from 2019 to 2100 under SSP1–2.6 and SSP5–8.5 scenarios (Figure 5 (i-k)). The projected permafrost area consistently showed a decreasing trend across different climate scenarios; however, the rate of this decline varied. Permafrost areas decreased gradually from $1.06 \pm 0.00 \times 10^{6}\,km^2$ (mean ± standard deviation) to $0.87 \pm 0.04 \times 10^{6}\,km^2$ under SSP1-2.6 and $0.49 \pm 0.02 \times 10^{6}\,km^2$ under SSP5-8.5 during 2019–2100 at a rate of $-0.02 \pm 0.00 \times 10^{6}\,km^2$ per decade (SSP1-2.6) and $-0.07 \pm 0.00 \times 10^{6}\,km^2$ per decade (SSP5-8.5) under the lower and higher emission pathway, respectively (Figure 5 (i)). By 2100, the permafrost areas, under SSP1-2.6 and SSP5-8.5, were projected to decrease by $22 \pm 3\,\%$ and $56 \pm 2\,\%$, respectively, compared to the baseline period.

Figure 5 (j) presents the changes in MAGT during the period 2019–2100. Although projected MAGT based on AWI-CM-1-1-MR and MPI-ESM1-2-HR varies considerably under SSP1–2.6, MAGT increases slightly in the first half-century and decreases further until the end of the century, with insignificant changes in MAGT throughout the century. Under SSP5–8.5 scenarios, MAGT increased significantly to around $-1.0\,^{\circ}C$ by 2100. Relative to the mean MAGT ($-2.26 \pm 0.17\,^{\circ}C$) in the baseline period, MAGT decreased by about $-0.07 \pm 0.18\,^{\circ}C$ and $-0.26 \pm 0.15\,^{\circ}C$ under SSP1–2.6 by mid-century (2041–2060) and end-century (2081–2100), respectively, while, under SSP5–8.5, MAGT increases by about $0.28 \pm 0.03\,^{\circ}C$ and $1.20 \pm 0.05\,^{\circ}C$ by the period 2041–2060 and 2081–2100, respectively.

The time series of simulated ALT in the permafrost areas are shown in Figure 5 (k). The temporal variation of ALT was different in both climate scenarios. Under the lower emission pathway, ALT had no evident change throughout this century, while increasing to around 5.0 m by 2100 under severe climate warming. By the middle of this century, ALT in the permafrost areas of the TP increased by approximately 0.03 ± 0.17 m to 0.37 ± 0.07 m under SSP1–2.6 and SSP5–8.5 scenarios, respectively. However, ALT decreased by about 0.24 ± 0.11 m under SSP1–2.6 and increased by about 1.87 ± 0.14 m under SSP5–8.5 by the end of this century.

3.3 Spatial and temporal patterns of the vegetation in the permafrost areas on the TP

Analysis of satellite imagery data at the grid cell level (i.e. $0.1\,^{\circ}$) revealed that, during the period from 2000 to 2018, $NDVI_{GS}$ trends in the majority of permafrost areas (67.17%) on the TP did not exhibit significant changes (p-value $>$ 0.05). A portion of the permafrost areas, constituting 31.55%, displayed an increase in $NDVI_{GS}$ (p-value $<$

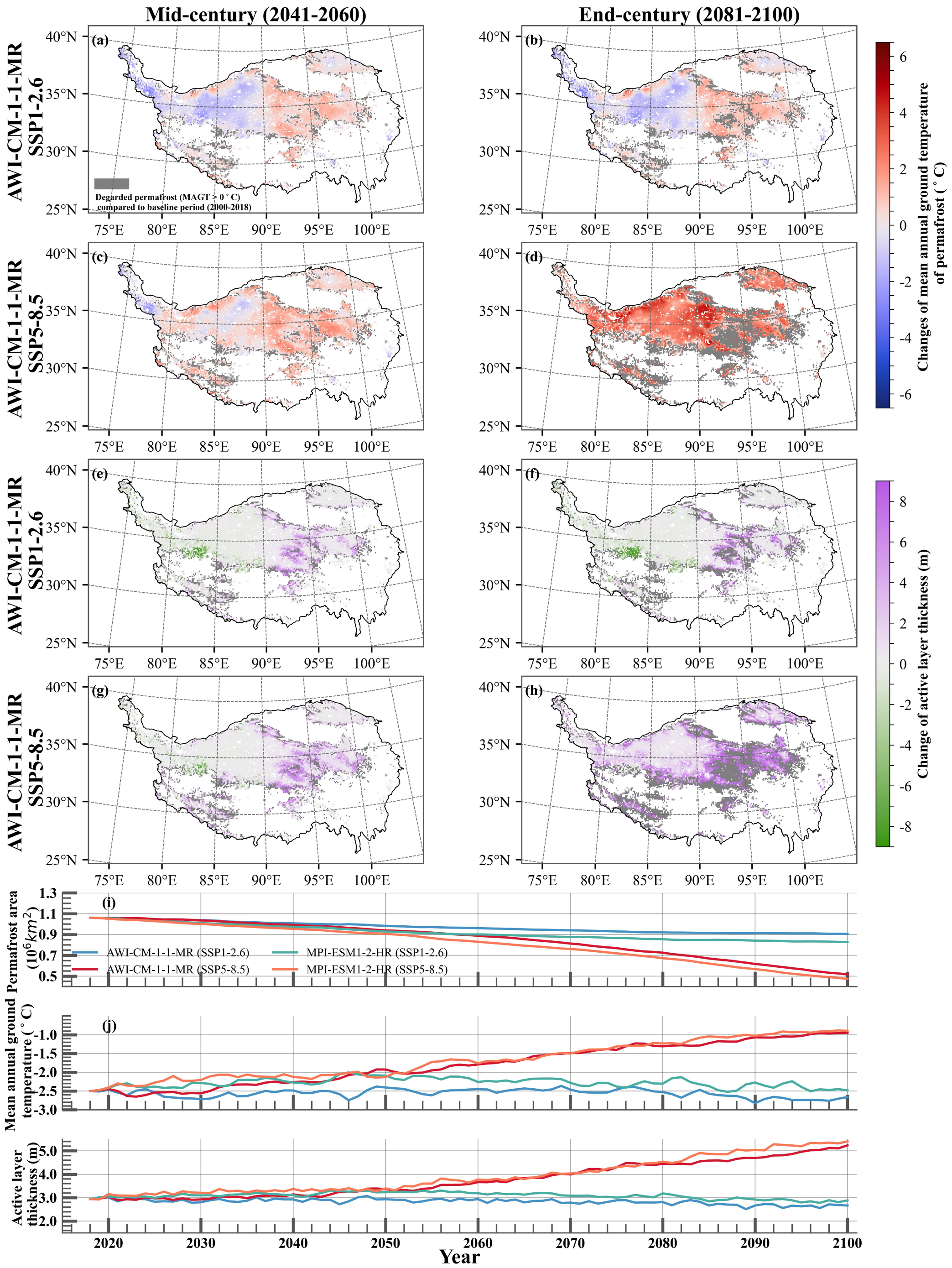

Figure 5. Spatial changes of the mean annual ground temperature (a-d) and active layer thickness (e-h) on the Tibetan Plateau by mid-century (2041–2060) and end-century(2081–2100) under SSP1–2.6 and SSP5–8.5 scenarios from AWI-CM-1-1-MR, related to the baseline period (2000–2018), respectively. (i-k) Time evolution of the changes in permafrost areas, mean annual ground temperature, and active layer thickness from 2019 to 2100 under the SSP1-2.6 and SSP5-8.5 scenarios. The grey area indicates degraded permafrost areas compared with the baseline by the mid-century (2041–2060) and end-century (2081–2100), and the blue, red, green, and orange lines represent the SSP1–2.6 and SSP5–8.5 scenarios from AWI-CM-1-1-MR and SSP1–2.6 and SSP5–8.5 scenarios from MPI-ESM1-2-HR, respectively.

0.05), whereas a minimal area, representing only 1.28% experienced a decline in $NDVI_{GS}$ (p-value < 0.05) (Figure 6 (c)). Within the non-permafrost areas, 18.96% and 2.24% proportion of the area experienced an increased and decreased $NDVI_{GS}$, respectively, during the same period (Figure 6 (d)). Although we utilized data from both permafrost and non-permafrost areas across all grid cells to construct our training dataset, the predictive accuracy for extrapolations beyond the training data range was notably constrained, especially under the high-emission SSP5–8.5 scenarios, due to the inherent data dependency in machine learning. To enhance the robustness of our future NDVI change simulations, we narrowed down our predictions to 2050. Our machine learning analysis, based on the SSP1–2.6 scenarios using two ESMs, indicated a stable $NDVI_{GS}$ (ensemble mean) across the permafrost areas, with no significant alterations anticipated from 2019 through 2050 (p-value > 0.05), maintaining an average $NDVI_{GS}$ of 0.25 ± 0.03 (Figure 6 (a); blue and green line). Spatial distribution analysis of the mean annual $NDVI_{GS}$ trend under both ESMs showed no considerable shifts in vegetation conditions over 85–97% of the permafrost regions up to the middle of the century (Figure 6 (e) and Supporting Information Figure S5 (a)), this stability likely attributable to the relatively stable climatic conditions associated with lower emission trajectories. In contrast, under the SSP5–8.5 scenarios, results from the Mann-Kendall test suggested a marginally increasing trend in the ensemble mean of the $NDVI_{GS}$ anomaly time series ($0.05 <$ p-value < 0.10), with a rate of 0.01 ± 0.00 per decade (Figure 6 (a); orange and red line). Moreover, over 7–29% of the permafrost areas exhibited increased $NDVI_{GS}$, while a significant decrease in $NDVI_{GS}$ was observed in only about 0.33–1.17% of the area under both scenarios (Figure 6 (g) and Supporting Information Figure S5 (c)). Consequently, our findings hint at a potential slightly increased $NDVI_{GS}$ within the permafrost areas over the TP, amidst the ongoing severe climate warming projected by the middle of the century. Figure 6 (b, f, h) and Supporting Information Figure S5 (b, d) outline the time series of the $NDVI_{GS}$ anomaly and spatial distribution of the mean annual $NDVI_{GS}$ trend across the non-permafrost areas. From 2019 to 2050, the ensemble mean of the time series for mean annual $NDVI_{GS}$ anomaly in the majority of non-permafrost areas was expected to remain relatively stable under SSP1–2.6 scenarios (p-value > 0.05), while a slight increase in $NDVI_{GS}$ trend, similar with the permafrost areas, is anticipated under SSP5–8.5 scenarios ($0.05 <$ p-value < 0.10). Spatially, 1.90–5.03% permafrost and 6.10–8.77% non-permafrost areas showed an increasing trend under the SSP1–2.6 and SSP5–8.5 scenarios, respectively. In summary, $NDVI_{GS}$ trends in most permafrost and non-permafrost areas were expected to remain stable under lower emission pathways till the midpoint of this century. Conversely, under higher emission pathways, $NDVI_{GS}$ was likely to exhibit an increasing trend in permafrost and non-permafrost areas. According to the vegetation types dataset of the TP Zhou et al. (2022), the alpine meadow and alpine steppe constituted the primary vegetation in the permafrost areas. We further detected the annual $NDVI_{GS}$ change for different vegetation types (alpine steppe and alpine meadow) in the permafrost areas (Supporting Information Figure S6). Our results showed that areas with increased mean annual $NDVI_{GS}$ outnumbered those with decreased mean annual $NDVI_{GS}$ for both vegetation types, although the extent of this disparity varied under the two scenarios.

3.4 Important features of spatiotemporal variability of the vegetation in the permafrost areas on the TP

The evolution of vegetation is influenced by an interplay of various climatic and terrestrial factors (Hawinkel et al., 2016; Y. Wei et al., 2022; Higgins et al., 2023). We performed ridge regression for both permafrost and non-permafrost areas to identify the absolute values of the contribution of each explanatory factor and detect the most important variables to $NDVI_{GS}$ change. For the baseline period, climate variables (i.e. SAT_{GS}, PRE_{GS}, and SIN_{GS}) contributed notably (59.34% of permafrost areas and 68.65% of non-permafrost areas) to the $NDVI_{GS}$ change, specifically, the contribution of SAT_{GS} was the largest (22.99%) in the permafrost and was the secondary important factor (21.53%)

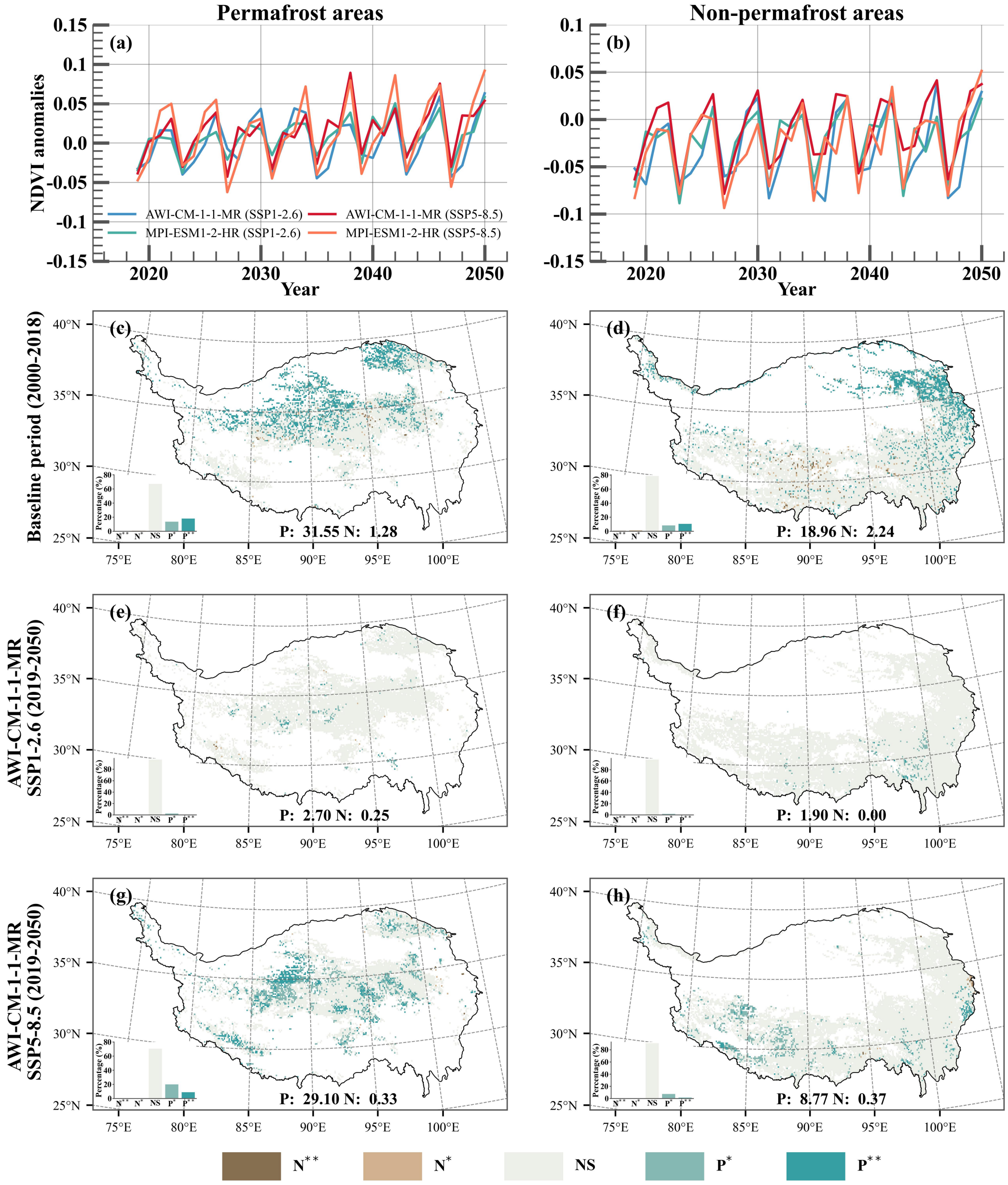

Figure 6. (a-b) Time series of mean annual $NDVI_{GS}$ anomalies (minus the mean value during 2000–2018) from 2019 to 2050 under the future climate conditions on the permafrost and non-permafrost areas over the TP. The blue, red, green, and orange lines represent SSP1–2.6 and SSP5–8.5 scenarios from AWI-CM-1-1-MR and MPI-ESM1-2-HR, respectively. (c-h) Spatial patterns of mean annual $NDVI_{GS}$ trend across the permafrost and non-permafrost areas during the baseline (2000–2018) and future periods (2019–2050) under different climate scenarios from AWI-CM-1-1-MR. N, NS, and P indicate negative, non-significant, and positive trends. * and ** represent significance at p-value < 0.05 and 0.01, respectively

in the non-permafrost area of the plateau, the PRE_{GS} was identified as the third important factor and made similar contributions (17.52% and 19.67%) in the permafrost and non-permafrost areas, the SIN_{GS} had more contributions to the NDVI_{GS} change in the non-permafrost areas (27.45%) than that of in the permafrost areas (18.84%) (Figure 7 (a-d)). For the terrestrial variables (i.e. ST_{GS}, LWC_{GS}, and ALT_{GS} [excluded in non-permafrost areas]), they contributed to the NDVI_{GS} change of approximately 40% of the permafrost areas and 30% of the non-permafrost areas. We used the same method to examine the dominant factors controlling the change of annual NDVI_{GS} during 2019–2050 under different climate scenarios and different ESMs (Figure 7 (e-l) and Supporting Information Figure S7 (a-h)). The results revealed that predominant factors affecting the future NDVI_{GS} changes in permafrost and non-permafrost areas under the different scenarios remained largely consistent. That is, under the SSP1–2.6 and SSP5–8.5 scenarios, it was found that SAT_{GS} and LWC_{GS} emerged as the primary determinants of the interannual variability in NDVI_{GS} across permafrost areas, influencing between 61.24% and 76.26% of these areas. In non-permafrost areas on the TP, SIN_{GS} was identified as the predominant driver behind NDVI_{GS} interannual variability, affecting 33.38% to 45.59% of the areas under both scenarios. Supporting Information Figure S8 depicts the spatial patterns and relative importance of each explanatory variable across diverse vegetation types. The NDVI_{GS} interannual variation in both vegetation types was responsive to variations of climatic factors in the baseline period (approximately 60%). Aiming at the future periods, SAT_{GS} and LWC_{GS} explained a much larger portion of the NDVI_{GS} variations than other factors in both vegetation types (Supporting Information Figure S8 (e-l)). Overall, the interannual variability of the NDVI_{GS} tended to be predominantly controlled by the climate variables in both permafrost and non-permafrost areas from 2000 to 2018. Compared to the baseline period, our study indicated that SAT_{GS}, LWC_{GS} and SIN_{GS} were the main contributors to the NDVI_{GS} change in the permafrost and non-permafrost areas in the future periods (Figure 7 (e-l), Supporting Information Figure S7 (a-h)). Consequently, surface air temperature, liquid water content at the root zone, and incoming solar radiation played an important role in future NDVI_{GS} evolution on the TP.

4 Discussion

4.1 Comparison with previous modeling studies of the permafrost state and vegetation conditions on the TP

In this study, we utilized a computationally efficient numerical permafrost model (CryoGridLite) driven by climatic forcing data to simulate the thermal state of permafrost and ALT over the TP from 1979 to 2100. Table S5 summarizes the simulation results of the thermal state of permafrost and ALT on the TP under present and future climate conditions in the past 10 years based on different approaches. For the historical period, our results fell within the range of these studies for the permafrost state (MAGT: [-3.32° C, -1.35° C]; Permafrost areas: [$1.01 \times 10^6\,km^2$, $1.66 \times 10^6\,km^2$]) and ALT [1.24m, 3.23m]. As previously mentioned, the differences among these simulation results can be attributed to spatial resolution and study period, study approaches, and the definition of the permafrost state and ALT, etc. For the future period, although there were variations in magnitude and trends for the permafrost state and ALT between our study and others, all demonstrated that permafrost degradation over the TP would be an inevitable consequence in the 21st century under the SSP5–8.5/Representative Concentration Pathway (RCP) 8.5 scenarios. Meanwhile, under the SSP1–2.6/RCP2.6 scenarios, permafrost was anticipated to exhibit relative stability or only slight warming until the end of the century and was most likely aggradation in the northwest of the plateau due to the cooling surface air temperature under the SSP1-2.6 scenarios. In addition to the reasons mentioned above, the divergence in projections could largely be explained by the disparities among the ESMs employed in these studies. For instance, G. Zhang et al. (2022) used

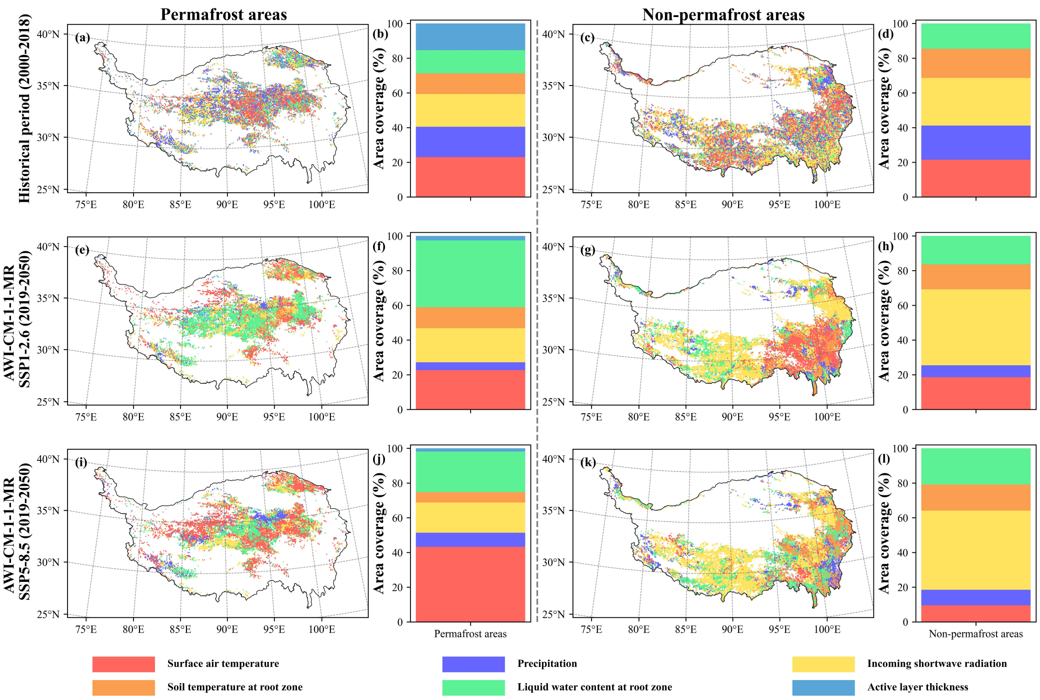

Figure 7. Spatial distribution of the dominant factors to the $NDVI_{GS}$ changes over different periods in the permafrost and non-permafrost areas. (a, c) Baseline period (2000–2018). (e, g) Future period (SSP1–2.6; AWI-CM-1-1-MR). (i,k) Future period (SSP5–8.5; AWI-CM-1-1-MR). The barplot (b, d, f, h, j, l) represents the proportion of the contribution of each variable in the permafrost and non-permafrost areas under AWI-CM-1-1-MR.

the Noah-LSM driven by five ESMs to project permafrost stability on the TP throughout this century. Their findings revealed significant variances among the ESMs' projections under identical scenarios (e.g. under the SSP5-8.5 scenarios, simulations driven by CESM2 and EC-Earth3 suggested that permafrost was highly likely to vanish by 2100, while, projections based on MPI-ESM1-2-HR (also used in our study) indicated that approximately $0.5 \times 10^{6}\, km^2$ (similar with our results) of permafrost might persist by the end of the century).

To project the NDVI in the future on the TP, we employed statistical models trained by machine-learning algorithms under two contrasting climate scenarios in this study. For the historical period (2000–2018), MODIS imagery indicated that the NDVI_{GS} showed an increasing trend over the TP, with a rate of 0.01 per decade, and 24% proportion of the area covered by plants exhibits greening (Supporting Information Figure S2 (a-c)). In addition to the MODIS NDVI data, other ecological indicators (e.g. LAI, NPP, EVI, fractional vegetation coverage [FVC]) demonstrated that vegetation greenness increased on the TP since 2000 (Piao et al., 2020; M. Shen et al., 2022; Yang et al., 2023; X. Zhang & Li, 2023). Regarding vegetation evolution in the future, although few studies have elucidated the magnitude and trends of NDVI in the permafrost areas on the TP (H. Li et al., 2024), studies based on other vegetation factors and methods showed that under the background of future climate change, there was a potential for vegetation greening on the TP (Q. Gao et al., 2016; Mahowald et al., 2016; W. Liu et al., 2020; Cuo et al., 2022; M. Shen et al., 2022; Kong et al., 2023), which aligns with our study. For example, Q. Gao et al. (2016) and Cuo et al. (2022) applied the Lund-Potsdam-Jena dynamic global vegetation model (LPJ-DGVM) to quantify the annual NPP changes on the TP under CMIP5/CMIP6 scenarios. Their findings indicated a general increase in annual NPP, with a notable shift in the dominant vegetation, as alpine shrubs are projected to replace alpine meadows and steppes. The simulation results from ESMs (CMIP5) and regional climate models indicated a continued increasing trend of LAI by the end of the century in the northern temperate region (25–50° N: including the TP) and TP (Mahowald et al., 2016; W. Liu et al., 2020). Kong et al. (2023) constructed a framework of machine learning algorithms to predict the evolution trajectory of FVC in China under four SSP scenarios from 2019 to 2060, with FVC showing an increasing trend except for the east region of China. H. Li et al. (2024) indicated that under the various climate scenarios, along with significant permafrost degradation, the TP exhibited a greening (NDVI) trend in vegetation which persists until the end of the century. In addition to employing the vegetation indices to analyze future vegetation greenness, a recent review summarized the potential plant phenology changes on the TP in this century, which included the advanced start of the growing season and the delayed end of the growing season, causing vegetation greening on the TP (M. Shen et al., 2022). Besides, we would like to point out that there are ongoing debates regarding the continued vegetation greening phenomenon that occurs on the TP and the prospect of the TP becoming a net carbon sink in the future, especially considering carbon released by thawing permafrost and enhanced soil and plant respiration (X. Jin et al., 2021; D. Wei et al., 2021; Ehlers et al., 2022; T. Wang et al., 2022). Consequently, an enhanced focus on the vegetation conditions within the permafrost regions of the Tibetan Plateau is warranted in future studies.

4.2 Important features of vegetation greening

In our study, we used ridge regression to discern the absolute values of the contributions of the driving factors for the NDVI changes on the TP. For the baseline period, the climatic variables were the important features of NDVI_{GS} on the TP in both permafrost (approximately 60%) and non-permafrost areas (approximately 70%) (Figure 7, Supporting Information Figure S7). Piao et al. (2020) noted that dynamic global vegetation models suggested that CO_2 fertilization (a phenomenon widely acknowledged for enhancing vegetation growth) continued to be the predominant factor driving vegetative greening on a global scale. However, in northern high latitudes and the TP, it is the increasing temperatures that primarily contributed to the observed greening trends (LAI). Statistical analysis (Teng et al., 2021; X. Li et al., 2022; M. Shen et al., 2022; T. Wang et al., 2022) and sensitivity experiments (Y. Wang et al., 2023) also demonstrated that climate change played an important role in vegetation growth over the past 40 years on the TP, albeit with contributions of varying magnitudes. This variability in quantitative contributions was attributed to the differential impact of various input explanatory variables (e.g. climate variables, terrain, soil properties) and different data sources (e.g. MODIS data, Global Inventory Modeling and Mapping Studies NDVI product [GIMMS NDVI], and SPOT VEGETATION imagery [SPOT-VEG NDVI]). For the future period, our findings indicated that, compared with the baseline period, NDVI_{GS} showed a potential increasing trend likely occurring in the permafrost areas under the SSP5–8.5 scenarios, mainly attributed to the change of SAT_{GS} and LWC_{GS}. Supporting Information Figure S9 and S10 indicate the spatiotemporal distribution of LWC_{GS} and SAT_{GS} in the permafrost areas from 2019 to 2050. In the vast majority of permafrost regions, both the SATGS and the LWCGS have exhibited an increasing trend. This was in agreement with the results from J. Gao et al. (2017), who combined the LPJ-DGVM with the geographical regression, and R. Cao et al. (2023), who conducted multiple sensitivity experiments based on machine learning algorithms. All indicated that temperature would more significantly affect vegetation changes over the TP. One potential explanation is that warmer temperatures extend the duration of growing seasons, enhance photosynthetic activity, and lead to greater biomass accumulation ((J. Gao et al., 2017; X. Li et al., 2022; M. Shen et al., 2022)). Additionally, our results emphasized the important role of LWC_{GS} in vegetation growing in the permafrost areas. Besides, it is important to acknowledge that in this study we only considered the impact of a few variables on NDVI_{GS} change over the TP, without taking into account other factors. Future studies should synthesize more driving factors and implement more analysis methods (e.g. partial correlation analysis or structural equation model) to improve our understanding of the vegetation change on the TP.

4.3 Model limitation and uncertainty

While the CryoGridLite model capably replicates the mean state (Figure 3 (a-b), Table S4) and temporal evolution (Supporting Information Figure S3) of the permafrost thermal regime across the TP, there is a need for further development and enhancements to diminish the uncertainty of simulations. For instance, the single offline simulation driven by singular meteorological forcing data (He et al., 2020) and soil stratigraphy datasets (Y. Dai, Xin, et al., 2019; Y. Dai, Wei, et al., 2019) and a fixed maximum snow depth (i.e., 0.1 m) and snow density (i.e., $150\,kg\,m^{-3}$) for all grid cells may introduce a large degree of uncertainty for simulation (W. Wang et al., 2016; Lu et al., 2020; Langer et al., 2024). Hence, conducting ensemble parameter simulations (including forcing, soil, and snow properties datasets) should be the direction of our subsequent research endeavors (Nitzbon et al., 2023; Langer et al., 2024). This approach is crucial for a more accurate quantification of the permafrost thermal state across the TP. Furthermore, compared with Nitzbon et al. (2023) and Langer et al. (2024), in this tailored version of CryoGridLite, we implemented the surface energy balance (Supporting Information Text S1.1) and "bucket" scheme (Supporting Information Text S1.2) to calculate the dynamics of upper boundary conditions and groundwater changes, respectively. However, as pointed out by Langer et al. (2024), the model calculated the ground freezing by an enthalpy–temperature relation of free water instead of accurate soil freezing characteristic curves, and the model does not account for the interactions between permafrost and vegetation (Stuenzi, Boike, Cable, et al., 2021; Stuenzi, Boike, Gädeke, et al., 2021), subsidence processes following excess ice melting (Nitzbon et al., 2019), and sub-grid lateral fluxes (Nitzbon et al., 2021), which are known to affect permafrost thaw trajectories in complex landscapes. Further detailed descriptions of model limitation and uncertainty can be found in Langer et al. (2024). Moreover, for future permafrost simulations, we employed two ESMs (AWI-CM-

1-1-MR and MPI-ESM1-2-HR) to drive our CryoGridLite model. These ESMs have demonstrated their capability in accurately reproducing mean annual and seasonal surface air temperatures over recent decades (R. Chen, Li, et al., 2022). However, significant discrepancies were observed in their representation of precipitation changes (R. Chen, Duan, et al., 2022), introducing a notable degree of uncertainty into our permafrost projections. This is due to the permafrost's thermal state being highly sensitive not only to air temperature but also to precipitation; increased rainfall can significantly mitigate permafrost degradation on the Tibetan Plateau (TP) (G. Zhang et al., 2021; Hamm et al., 2023). Therefore, to enhance our understanding of permafrost evolution on the TP, it is imperative to conduct additional simulations using a variety of ESMs

Regarding the NDVI changes predicted by our model, we acknowledge a certain degree of uncertainty inherent in the outputs of our machine learning algorithms. Primarily, these models are challenged by their reliance on data-driven approaches, which may lack a solid physical basis, transparency, interpretability, and a heightened sensitivity to outliers, potentially leading to instability or inaccurate predictions (G. Zhang et al., 2022; C. Shen et al., 2023). Therefore, in our study, although we implemented several strategies to overcome the inherent shortcomings of machine learning algorithms, to make our results more robust, we extrapolated the predicted NDVI only to 2050. In addition, while NDVI data are extensively utilized for assessing the vegetative state of the TP (Teng et al., 2021; T. Wang et al., 2022; Yang et al., 2023), the reliability of this satellite-derived data is considerably impacted by factors such as sensor characteristics, atmospheric interference, and soil background effects (Sha et al., 2020). Therefore, it is crucial for future research to incorporate a broad spectrum of vegetation indices (e.g. LAI, EVI, NPP, soil-adjusted vegetation index) and apply more data to feed machine learning model to reduce these errors and enable a more comprehensive analysis of vegetative dynamics on the TP, particularly against the backdrop of ongoing climatic warming. Moreover, we would like to point out that NDVI_{GS} predictions in this study were based on MODIS satellite imagery. Owing to the data dependency of the machine learning model, the use of alternative NDVI products as response variables might yield divergent results. This is particularly evident in the study of Yang et al. (2023), which employed multi-source data to investigate vegetation changes on the TP since 2000, revealing significant spatiotemporal discrepancies among MODIS data, GIMMS NDVI, and SPOT-VEG NDVI (e.g. SPOT-VEG NDVI ($p < 0.001$) and MODIS NDVI ($p < 0.05$) indicated a significant increasing trend, while GIMMS NDVI data ($p < 0.534$) did not show a significant increasing trend in NDVI on the TP). Meanwhile, the selection of explanatory variables significantly influences the determination of the quantitative contributions of predominant factors. Additionally, vegetation browning events induced by abrupt permafrost thaw (Heijmans et al., 2022) and vegetation greening occurring in thermokarst-drained lake basins (Y. Chen et al., 2023) are not considered in our study, which play an important role in controlling vegetation growth. Despite several shortcomings in our permafrost model and machine learning algorithms, our results attempt to provide a framework for exploring future vegetation changes in cold regions and identified limitations give opportunities for future improvements in our modeling approach.

5 Conclusions

In this study, we combined a numerical permafrost model (CryoGridLite) with machine-learning algorithms to analyze the vegetation conditions in the permafrost areas over the TP under various climate scenarios. Our model simulations, when compared with observational data, efficiently captured the spatiotemporal patterns of permafrost across the TP during the baseline period (2000–2018), and the machine learning algorithm effectively reproduced the interannual NDVI_{GS} for the testing period (2015–2018). Forced by different climate conditions, our CryoGridLite model projected a continual decline in the permafrost areas on the TP in response to future climate warming. Under the SSP1-

2.6 scenario, mean annual ground temperature and active layer thickness appeared stable on average, but with regionally different responses i.e mean annual ground temperature and active layer thickness tended to increase in the Three River Source region and Qinghai-Tibet Engineering Corridor and decrease in the northwest of TP. However, under the SSP5-8.5 scenarios, there was a notable increase in both mean annual ground temperature and active layer thickness. Remote sensing imagery from MODIS suggested that approximately 30% of the permafrost areas on the TP showed an increasing trend in NDVI_{GS} over the baseline period. The results of machine learning indicated that under the low emission scenario (SSP1–2.6), no significant change in NDVI_{GS} was expected for >85% permafrost areas in the future. In contrast, under the high emission scenario, an increasing trend in NDVI_{GS} in the future in about 7.31–29.10% of the permafrost areas, with less than 2% of the area experiencing a significantly decreased NDVI. Analysis of the contributory factors revealed that climatic factors during the growing season were the primary influence on NDVI alterations within the permafrost areas for the baseline period (2000–2018). For the future periods (2019–2050), it was found that the surface air temperature and liquid water content at the root zone during the growing season were anticipated to play a crucial, undeniable role in the NDVI_{GS} changes within the permafrost areas. Although our approach has not yet fully accounted for the processes affecting the thermal state of permafrost and vegetation growth on the TP, the coupling of process-based and data-driven models provides a potential and meaningful pathway for detecting future vegetation evolution on the plateau. Our future research will aim to address the limitations of our methodology and deliver more accurate predictions, thereby enhancing our understanding of the carbon budget of the TP.

Open Research Section

The China Meteorological Forcing Dataset is available at `https://data.tpdc.ac.cn/zh-hans/data/8028b944-daaa-4511-8769-965612652c49`. The AWI-CM-1-1-MR and MPI-ESM1-2-HR datasets are available at `https://esgf-data.dkrz.de/search/cmip6-dkrz/`. The Vegetation types data is available at `https://www.resdc.cn/data.aspx?DATAID=122`. The shapefile of the boundary of the Tibetan Plateau is available at `https://www.geodoi.ac.cn/WebCn/doi.aspx?Id=135`. The shape file of lakes on the Tibetan Plateau is available at `https://www.tpdc.ac.cn/zh-hans/data/da4ffc9a-91fb-4ae9-8da5-c57aa92c8d2b`. The shape file of the glacier on the Tibetan Plateau is available at `https://www.tpdc.ac.cn/zh-hans/data/f92a4346-a33f-497d-9470-2b357ccb4246`. The Global high-resolution dataset of soil hydraulic and thermal parameters dataset is available at `http://globalchange.bnu.edu.cn/research/soil5.jsp`. The Global watertable depth dataset is available at `https://glowasis.deltares.nl/thredds/catalog/opendap/opendap/Equilibrium_Water_Table/catalog.html`. The Terrestrial heat flow dataset is available at `https://doi.org/10.1029/2019GC008389`. The ERA5-Land dataset is available at `https://cds.climate.copernicus.eu/cdsapp#!/dataset/reanalysis-era5-land?tab=overview`. The MODIS NDVI (MOD13A2, Version 6.1) is available from Google Earth Engine at `https://developers.google.com/earth-engine/datasets/catalog/MODIS_061_MOD13A2`. The CryoGridLite model code, machine-learning algorithms, and ridge regression method used for the simulations and analysis in this work are archived on Zenodo (`https://doi.org/10.5281/zenodo.10928146`).

Acknowledgments

Rui Chen was supported by the China Scholarship Council (No. 201904910442). Simone M. Stuenzi was supported by the Bundesministerium für Bildung und Forschung (grant no. 03F0931A).

References

Baral, P., Allen, S., Steiner, J. F., Gurung, T. R., & McDowell, G. (2023). Climate change impacts and adaptation to permafrost change in high mountain asia: a comprehensive review. *Environmental Research Letters*, *18*, 093005. doi: https://doi.org/10.1088/1748-9326/acf1b4

Cao, B., Gruber, S., Zhang, T., Li, L., Peng, X., Wang, K., ... Guo, H. (2017). Spatial variability of active layer thickness detected by ground-penetrating radar in the qilian mountains, western china. *Journal of Geophysical Research: Earth Surface*, *122*, 574–591. doi: https://doi.org/10.1002/2016JF004018

Cao, R., Ling, X., Liu, L., Wang, W., Li, L., & Shen, M. (2023). Remotely sensed vegetation green-up onset date on the tibetan plateau: Simulations and future predictions. *IEEE Journal of Selected Topics in Applied Earth Observations and Remote Sensing*, *16*, 8125–8134. doi: https://doi.org/10.1109/JSTARS.2023.3310617

Cao, Z., Nan, Z., Hu, J., Chen, Y., & Zhang, Y. (2023). A new 2010 permafrost distribution map over the qinghai–tibet plateau based on subregion survey maps: a benchmark for regional permafrost modeling. *Earth System Science Data*, *15*, 3905–3930. doi: https://doi.org/10.5194/essd-15-3905-2023

Chang, X., Jin, H., Zhang, Y., He, R., Luo, D., Wang, Y., ... Zhang, Q. (2015). Thermal impacts of boreal forest vegetation on active layer and permafrost soils in northern da xing'anling (hinggan) mountains, northeast china. *Arctic, Antarctic, and Alpine Research*, *47*, 267–279. doi: https://doi.org/10.1657/AAAR00C-14-016

Chen, C., Peng, X., Frauenfeld, O. W., Chu, X., Chen, G., Huang, Y., ... Tian, W. (2024). Simulations and prediction of historical and future maximum freeze depth in the northern hemisphere. *Journal of Geophysical Research: Atmospheres*, *129*, e2023JD039420. doi: https://doi.org/10.1029/2023JD039420

Chen, F., Zhang, X., & Chen, Z. (2023). High-temperature exposure and land transactions in china. *Earth's Future*, *11*, e2022EF003008. doi: https://doi.org/10.1029/2022EF003008

Chen, H., Nan, Z., Zhao, L., Ding, Y., Chen, J., & Pang, Q. (2015). Noah modelling of the permafrost distribution and characteristics in the west kunlun area, qinghai-tibet plateau, china. *Permafrost and Periglacial Processes*, *26*, 160–174. doi: https://doi.org/10.1002/ppp.1841

Chen, J., Zhao, L., Sheng, Y., Li, J., Wu, X., Du, E., ... Pang, Q. (2016). Some characteristics of permafrost and its distribution in the gaize area on the qinghai-tibet plateau, china. *Arctic, Antarctic, and Alpine Research*, *48*, 395–409. doi: https://doi.org/10.1657/AAAR0014-023

Chen, R., Duan, K., Shang, W., Shi, P., Meng, Y., & Zhang, Z. (2022). Increase in seasonal precipitation over the tibetan plateau in the 21st century projected using cmip6 models. *Atmospheric Research*, *277*, 106306. doi: https://doi.org/10.1016/j.atmosres.2022.106306

Chen, R., Li, H., Wang, X., Gou, X., Yang, M., & Wan, G. (2022). Surface air temperature changes over the tibetan plateau: Historical evaluation and future projection based on cmip6 models. *Geoscience Frontiers*, *13*, 101452. doi: https://doi.org/10.1016/j.gsf.2022.101452

Chen, R., von Deimling, T. S., Boike, J., Wu, Q., & Langer, M. (2023). Simulating the thermal regime of a railway embankment structure on the tibetan plateau under climate change. *Cold Regions Science and Technology*, *212*, 103881. doi: https://doi.org/10.1016/j.coldregions.2023.103881

Chen, T., & Guestrin, C. (2016). Xgboost: A scalable tree boosting system. In *Proceedings of the 22nd acm sigkdd international conference on knowledge discovery and data mining* (p. 785–794). New York, NY, USA: Association for Computing Machinery. Retrieved from `https://doi.org/10.1145/2939672.2939785` doi: 10.1145/2939672.2939785

Chen, Y., Cheng, X., Liu, A., Chen, Q., & Wang, C. (2023). Tracking lake drainage events and drained lake basin vegetation dynamics across the arctic. *Nature Communications*, *14*, 7359. doi: https://doi.org/10.1038/s41467-023-43207-0

Cuo, L., Zhang, Y., & Li, N. (2022). Historical and future vegetation changes in the degraded frozen soil and the entire tibetan plateau and climate drivers. *Journal of Geophysical Research: Biogeosciences*, *127*, e2022JG006987. doi: https://doi.org/10.1029/2022JG006987

Dai, L., Che, T., Xie, H., & Wu, X. (2018). Estimation of snow depth over the qinghai-tibetan plateau based on amsr-e and modis data. *Remote Sensing*, *10*, 1989. doi: https://doi.org/10.3390/rs10121989

Dai, Y., Shangguan, W., Duan, Q., Liu, B., Fu, S., & Niu, G. (2013). Development of a china dataset of soil hydraulic parameters using pedotransfer functions for land surface modeling. *Journal of Hydrometeorology*, *14*, 869–887.

Dai, Y., Wei, N., Yuan, H., Zhang, S., Shangguan, W., Liu, S., ... Xin, Y. (2019). Evaluation of soil thermal conductivity schemes for use in land surface modeling. *Journal of Advances in Modeling Earth Systems*, *11*, 3454–3473. doi: https://doi.org/10.1029/2019MS001723

Dai, Y., Xin, Q., Wei, N., Zhang, Y., Shangguan, W., Yuan, H., ... Lu, X. (2019). A global high-resolution data set of soil hydraulic and thermal properties for land surface modeling. *Journal of Advances in Modeling Earth Systems*, *11*, 2996–3023. doi: https://doi.org/10.1029/2019MS001784

de Vrese, P., Georgievski, G., Rouco, J. F. G., Notz, D., Stacke, T., Steinert, N. J., ... Brovkin, V. (2023). Representation of soil hydrology in permafrost regions may explain large part of inter-model spread in simulated arctic and subarctic climate. *The Cryosphere*, *17*, 2095–2118. doi: https://doi.org/10.5194/tc-17-2095-2023

Didan, K. (2015). *Mod13a2 modis/terra vegetation indices 16-day l3 global 1km sin grid v006.* doi: https://doi.org/10.5067/MODIS/MOD13A2.061

Ding, J., Chen, L., Ji, C., Hugelius, G., Li, Y., Liu, L., ... Yang, Y. (2017). Decadal soil carbon accumulation across tibetan permafrost regions. *Nature Geoscience*, *10*, 420–424. doi: https://doi.org/10.1038/ngeo2945

Ehlers, T. A., Chen, D., Appel, E., Bolch, T., Chen, F., Diekmann, B., ... Zhu, L. (2022). Past, present, and future geo-biosphere interactions on the tibetan plateau and implications for permafrost. *Earth-Science Reviews*, *234*, 104197. doi: https://doi.org/10.1016/j.earscirev.2022.104197

Fan, Y., Li, H., & Miguez-Macho, G. (2013). Global patterns of groundwatertable depth. *Science*, *339*, 940–943. doi: https://doi.org/10.1126/science.1229881

Gagnon, M., Domine, F., & Boudreau, S. (2019). The carbon sink due to shrub growth on arctic tundra: a case study in a carbon-poor soil in eastern canada. *Environmental Research Communications*, *1*, 091001. doi: https://doi.org/10.1088/2515-7620/ab3cdd

Gao, J., Jiao, K., Wu, S., Ma, D., Zhao, D., Yin, Y., & Dai, E. (2017). Past and future effects of climate change on spatially heterogeneous vegetation activity in china. *Earth's Future*, *5*, 679–692. doi: https://doi.org/10.1002/2017EF000573

Gao, Q., Guo, Y., Xu, H., Ganjurjav, H., Li, Y., Wan, Y., ... Liu, S. (2016). Climate change and its impacts on vegetation distribution and net primary productivity of the alpine ecosystem in the qinghai-tibetan plateau. *Science of The Total Environment*, *554–555*, 34–41. doi: https://doi.org/10.1016/j.scitotenv.2016.02.131

Gao, T., Zhang, Y., Kang, S., Abbott, B. W., Wang, X., Zhang, T., ... Gustafsson, Ö. (2021). Accelerating permafrost collapse on the eastern tibetan plateau. *Environmental Research Letters*, *16*, 054023. doi: https://doi.org/10.1088/1748-9326/abf7f0

Gao, Y., Luo, D., Chen, F., Lei, W., & Jin, H. (2023). Characteristics of the thermal regime and freeze-thaw cycles on the ground surface in permafrost regions in the headwater area of the yellow river. *Acta Geographica Sinica*, *78*, 604–619. doi: https://geog.com.cn/EN/10.11821/dlxb202303007

Grünberg, I., Wilcox, E. J., Zwieback, S., Marsh, P., & Boike, J. (2020). Linking tundra vegetation, snow, soil temperature, and permafrost. *Biogeosciences*, *17*, 4261–4279. doi: https://doi.org/10.5194/bg-17-4261-2020

Guo, D., & Wang, H. (2013). Simulation of permafrost and seasonally frozen ground conditions on the tibetan plateau, 1981–2010. *Journal of Geophysical Research: Atmospheres*, *118*, 5216–5230. doi: https://doi.org/10.1002/jgrd.50457

Guo, J., Zhai, L., Sang, H., Cheng, S., & Li, H. (2023). Effects of hydrothermal factors and human activities on the vegetation coverage of the qinghai-tibet plateau. *Scientific Reports*, *13*, 12488. doi: https://doi.org/10.1038/s41598-023-39761-8

Guo, W., Liu, S., Xu, J., Wu, L., Shangguan, D., Yao, X., ... Jiang, Z. (2015). The second chinese glacier inventory: data, methods and results. *Journal of Glaciology*, *61*, 357–372. doi: https://doi.org/10.3189/2015JoG14J209

Gupta, H. V., Kling, H., K, K., Yilmaz, & Martinez, G. F. (2009). Decomposition of the mean squared error and nse performance criteria: Implications for improving hydrological modelling. *Journal of Hydrology*, *377*, 80–91. doi: https://doi.org/10.1016/j.jhydrol.2009.08.003

Hamm, A., Magnússon, R. Í., Khattak, A. J., & Frampton, A. (2023). Continentality determines warming or cooling impact of heavy rainfall events on permafrost. *Nature Communications*, *14*, 3578. doi: https://doi.org/10.1038/s41467-023-39325-4

Hawinkel, P., Thiery, W., Lhermitte, S., Swinnen, E., Verbist, B., Orshoven, J. V., & Muys, B. (2016). Vegetation response to precipitation variability in east africa controlled by biogeographical factors. *Journal of Geophysical Research: Biogeosciences*, *121*, 2422–2444. doi: https://doi.org/10.1002/2016JG003436

He, J., Yang, K., Tang, W., Lu, H., Qin, J., Chen, Y., & Li, X. (2020). The first high-resolution meteorological forcing dataset for land process studies over china. *Scientific Data*, *7*, 25. doi: https://doi.org/10.1038/s41597-020-0369-y

Heijmans, M. M. P. D., Magnússon, R. Í., Lara, M. J., Frost, G. V., Myers-Smith, I. H., van Huissteden, J., ... Limpens, J. (2022). Tundra vegetation change and impacts on permafrost. *Nature Reviews Earth & Environment*, *3*, 68–84. doi: https://doi.org/10.1038/s43017-021-00233-0

Higgins, S. I., Conradi, T., & Muhoko, E. (2023). Shifts in vegetation activity of terrestrial ecosystems attributable to climate trends. *Nature Geoscience*, *16*, 147–153. doi: https://doi.org/10.1038/s41561-022-01114-x

Jin, X., Jin, H., Iwahana, G., Marchenko, S. S., Luo, D., Li, X., & Liang, S. (2021). Impacts of climate-induced permafrost degradation on vegetation: A review. *Advances in Climate Change Research*, *12*, 29–47. doi: https://doi.org/10.1016/j.accre.2020.07.002

Jin, Z., You, Q., Zuo, Z., Li, M., Sun, G., Pepin, N., & Wang, L. (2023). Weakening amplification of grassland greening to transpiration fraction of evapotranspiration over the tibetan plateau during 2001-2020. *Agricultural and Forest Meteorology*, *341*, 109661. doi: https://doi.org/10.1016/j.agrformet.2023.109661

Ke, G., Meng, Q., Finley, T., Wang, T., Chen, W., Ma, W., ... Liu, T. (2017). Lightgbm: A highly efficient gradient boosting decision tree. In *Proceedings of the 31st international conference on neural information processing systems* (pp. 3149–3157). Red Hook, NY, USA: Curran Associates Inc.

Kondylatos, S., Prapas, I., Ronco, M., Papoutsis, I., Camps-Valls, G., Piles, M., ... Carvalhais, N. (2022). Wildfire danger prediction and understanding with deep learning. *Geophysical Research Letters*, e2022GL099368. doi: https://doi.org/10.1029/2022GL099368

Kong, Z., Liang, H., Deng, M., Han, F., Yan, J., Deng, X., ... Wang, W. (2023).

Past and projected future patterns of fractional vegetation coverage in china. *Science of The Total Environment*, *902*, 166133. doi: https://doi.org/10.1016/j.scitotenv.2023.166133

Langer, M., Nitzbon, J., Groenke, B., Assmann, L.-M., von Deimling, T. S., Stuenzi, S. M., & Westermann, S. (2024). The evolution of arctic permafrost over the last 3 centuries from ensemble simulations with the cryogridlite permafrost model. *The Cryosphere*, *18*, 363–385. doi: https://doi.org/10.5194/tc-18-363-2024

Langer, M., von Deimling, T. S., Westermann, S., Rolph, R., Ralph, R., Antonova, S., … Grosse, G. (2023). Thawing permafrost poses environmental threat to thousands of sites with legacy industrial contamination. *Nature Communications*, *14*, 1721. doi: https://doi.org/10.1038/s41467-023-37276-4

Lawrence, D. M., & Swenson, S. C. (2011). Permafrost response to increasing arctic shrub abundance depends on the relative influence of shrubs on local soil cooling versus large-scale climate warming. *Environmental Research Letters*, *6*, 045504. doi: https://doi.org/10.1088/1748-9326/6/4/045504

Li, H., Pan, X., Washakh, R. M. A., & Nie, X. (2024). A new method of diagnosing the historical and projected changes in permafrost on the tibetan plateau. *Earth's Future*, *12*, e2023EF003897. doi: https://doi.org/10.1029/2023EF003897

Li, J., Wu, C., nuelas, J. P., Ran, Y., & Zhang, Y. (2023). The start of frozen dates over northern permafrost regions with the changing climate. *Global Change Biology*, *29*, 4556–4568. doi: https://doi.org/10.1111/gcb.16752

Li, X., Zhang, K., & Li, X. (2022). Responses of vegetation growth to climate change over the tibetan plateau from 1982 to 2018. *Environmental Research Communications*, *4*, 045007.

Liu, L., Zhuang, Q., Zhao, D., Zheng, D., Kou, D., & Yang, Y. (2022). Permafrost degradation diminishes terrestrial ecosystem carbon sequestration capacity on the qinghai-tibetan plateau. *Global Biogeochemical Cycles*, *36*, e2021GB007068. doi: https://doi.org/10.1029/2021GB007068

Liu, W., Wang, G., Yu, M., Chen, H., & Jiang, Y. (2020). Multimodel future projections of the regional vegetation-climate system over east asia: Comparison between two ensemble approaches. *Journal of Geophysical Research: Atmospheres*, *125*, e2019JD031967. doi: https://doi.org/10.1029/2019JD031967

Loranty, M. M., Abbott, B. W., Blok, D., Douglas, T. A., Epstein, H. E., Forbes, B. C., … Walker, D. A. (2018). Reviews and syntheses: Changing ecosystem influences on soil thermal regimes in northern high-latitude permafrost regions. *Biogeosciences*, *15*, 5287–5313. doi: https://doi.org/10.5194/bg-15-5287-2018

Lu, H., Zheng, D., Yang, K., & Yang, F. (2020). Last-decade progress in understanding and modeling the land surface processes on the tibetan plateau. *Hydrology and Earth System Sciences*, *24*, 5745–5758. doi: https://doi.org/10.5194/hess-24-5745-2020

Lucazeau, F. (2019). Analysis and mapping of an updated terrestrial heat flow data set. *Geochemistry, Geophysics, Geosystems*, *20*, 4001–4024. doi: https://doi.org/10.1029/2019GC008389

Luo, D., Jin, H., Jin, X., He, R., Li, X., Muskett, R. R., … Romanovsky, V. E. (2018). Elevation-dependent thermal regime and dynamics of frozen ground in the bayan har mountains, northeastern qinghai-tibet plateau, southwest china. *Permafrost and Periglacial Processes*, *29*, 257–270. doi: https://doi.org/10.1002/ppp.1988

Mahowald, N., Lo, F., Zheng, Y., Harrison, L., Funk, C., Lombardozzi, D., & Goodale, C. (2016). Projections of leaf area index in earth system models. *Earth System Dynamics*, *7*, 211–229. doi: https://doi.org/10.5194/esd-7-211-2016

Mauclet, E., Agnan, Y., Hirst, C., Monhonval, A., Pereira, B., Vandeuren, A., …

Opfergelt, S. (2022). Changing sub-arctic tundra vegetation upon permafrost degradation: impact on foliar mineral element cycling. *Biogeosciences*, *19*, 2333–2351. doi: https://doi.org/10.5194/bg-19-2333-2022

Mekonnen, Z. A., Riley, W. J., & Grant, R. F. (2018). Accelerated nutrient cycling and increased light competition will lead to 21st century shrub expansion in north american arctic tundra. *Journal of Geophysical Research: Biogeosciences*, *123*, 1683–1701. doi: https://doi.org/10.1029/2017JG004319

Mu, C., Abbott, B. W., Norris, A. J., Mu, M., Fan, C., Chen, X., ... Wu, X. (2020). The status and stability of permafrost carbon on the tibetan plateau. *Earth-Science Reviews*, *211*, 103433. doi: https://doi.org/10.1016/j.earscirev.2020.103433

Mu, C., Abbott, B. W., Zhao, Q., Su, H., Wang, S., Wu, Q., ... Wu, X. (2017). Permafrost collapse shifts alpine tundra to a carbon source but reduces n_2o and ch_4 release on the northern qinghai-tibetan plateau. *Geophysical Research Letters*, *44*, 8945–8952. doi: https://doi.org/10.1002/2017GL074338

Mu, C., & Peng, X. (2022). *A synthesis dataset of frozen ground and soil carbon in heihe river basin qilian mountainous (2011–2020).* National Tibetan Plateau Data Center. doi: https://doi.org/10.11888/Cryos.tpdc.272840

Müller, W. A., Jungclaus, J. H., Mauritsen, T., Baehr, J., Bittner, M., Budich, R., ... Marotzke, J. (2018). A higher-resolution version of the max planck institute earth system model (mpi-esm1.2-hr). *Journal of Advances in Modeling Earth Systems*, *10*, 1383–1413. doi: https://doi.org/10.1029/2017MS001217

Muñoz-Sabater, J., Dutra, E., Agustí-Panareda, A., Albergel, C., Arduini, G., Balsamo, G., ... Thépaut, J.-N. (2021). Era5-land: a state-of-the-art global reanalysis dataset for land applications. *Earth System Science Data*, *13*, 4349–4383. doi: https://doi.org/10.5194/essd-13-4349-2021

Myers-Smith, I. H., Kerby, J. T., Phoenix, G. K., Bjerke, J. W., Epstein, H. E., Assmann, J. J., ... Wipf, S. (2020). Complexity revealed in the greening of the arctic. *Nature Climate Change*, *10*, 106–117. doi: https://doi.org/10.1038/s41558-019-0688-1

Ni, J., Wu, T., Zhu, X., Hu, G., Zou, D., Wu, X., ... Yang, C. (2021). Simulation of the present and future projection of permafrost on the qinghai-tibet plateau with statistical and machine learning models. *Journal of Geophysical Research: Atmospheres*, *126*, e2020JD033402. doi: https://doi.org/10.1029/2020JD033402

Nitzbon, J., Krinner, G., von Deimling, T. S., Werner, M., & Langer, M. (2023). First quantification of the permafrost heat sink in the earth's climate system. *Geophysical Research Letters*, *50*, e2022GL102053. doi: https://doi.org/10.1029/2022GL102053

Nitzbon, J., Langer, M., Martin, L. C. P., Westermann, S., von Deimling, T. S., & Boike, J. (2021). Effects of multi-scale heterogeneity on the simulated evolution of ice-rich permafrost lowlands under a warming climate. *The Cryosphere*, *15*, 1399–1422. doi: https://doi.org/10.5194/tc-15-1399-2021

Nitzbon, J., Langer, M., Westermann, S., Martin, L., Aas, K. S., & Boike, J. (2019). Pathways of ice-wedge degradation in polygonal tundra under different hydrological conditions. *The Cryosphere*, *13*, 1089–1123. doi: https://doi.org/10.5194/tc-13-1089-2019

Nitze, I., Grosse, G., Jones, B. M., Romanovsky, V. E., & Boike, J. (2018). Remote sensing quantifies widespread abundance of permafrost region disturbances across the arctic and subarctic. *Nature Communications*, *9*, 5423. doi: https://doi.org/10.1038/s41467-018-07663-3

Obu, J., Westermann, S., Bartsch, A., Berdnikov, N., Christiansen, H. H., Dashtseren, A., ... Zou, D. (2019). Northern hemisphere permafrost map based on ttop modelling for 2000–2016 at $1km^2$ scale. *Earth-Science Reviews*, *193*, 299–316. doi: https://doi.org/10.1016/j.earscirev.2019.04.023

Orsolini, Y., Wegmann, M., Dutra, E., Liu, B., Balsamo, G., Yang, K., … Arduini, G. (2019). Evaluation of snow depth and snow cover over the tibetan plateau in global reanalyses using in situ and satellite remote sensing observations. *The Cryosphere*, *13*, 2221–2239. doi: https://doi.org/10.5194/tc-13-2221-2019

Pang, G., Chen, D., Wang, X., & Lai, H. (2022). Spatiotemporal variations of land surface albedo and associated influencing factors on the tibetan plateau. *Science of The Total Environment*, *804*, 150100. doi: https://doi.org/10.1016/j.scitotenv.2021.150100

Pang, Y., Zou, K., Guo, X., Chen, Y., Zhao, J., Zhou, F., … Yang, G. (2022). Geothermal regime and implications for basin resource exploration in the qaidam basin, northern tibetan plateau. *Journal of Asian Earth Sciences*, *239*, 105400. doi: https://doi.org/10.1016/j.jseaes.2022.105400

Pearson, R. G., Phillips, S. J., Loranty, M. M., Beck, P. S. A., Damoulas, T., Knight, S. J., & Goetz, S. J. (2013). Shifts in arctic vegetation and associated feedbacks under climate change. *Nature Climate Change*, *3*, 673–677. doi: https://doi.org/10.1038/nclimate1858

Piao, S., Wang, X., Park, T., Chen, C., Lian, X., He, Y., … Myneni, R. B. (2020). Characteristics, drivers and feedbacks of global greening. *Nature Reviews Earth & Environment*, *1*, 14–27. doi: https://doi.org/10.1038/s43017-019-0001-x

Prager, C. M., Boelman, N. T., Eitel, J. U. H., Gersony, J. T., Greaves, H. E., Heskel, M. A., … Griffin, K. L. (2020). A mechanism of expansion: arctic deciduous shrubs capitalize on warming-induced nutrient availability. *Oecologia*, *192*, 671–685. doi: https://doi.org/10.1007/s00442-019-04586-8

Qin, Y., Wu, T., Zhao, L., Wu, X., Li, R., Xie, C., … Hao, J. (2017). Numerical modeling of the active layer thickness and permafrost thermal state across qinghai-tibetan plateau. *Journal of Geophysical Research: Atmospheres*, *122*, 11604–11620. doi: https://doi.org/10.1002/2017JD026858

Ran, Y., Cheng, G., Dong, Y., Hjort, J., Lovecraft, A. L., Kang, S., … Li, X. (2022). Permafrost degradation increases risk and large future costs of infrastructure on the third pole. *Communications Earth & Environment*, *3*, 238. doi: https://doi.org/10.1038/s43247-022-00568-6

Ran, Y., Li, X., & Cheng, G. (2018). Climate warming over the past half century has led to thermal degradation of permafrost on the qinghai–tibet plateau. *The Cryosphere*, *12*, 595–608. doi: https://doi.org/10.5194/tc-12-595-2018

Ran, Y., Li, X., Cheng, G., Che, J., Aalto, J., Karjalainen, O., … Chang, X. (2022). New high-resolution estimates of the permafrost thermal state and hydrothermal conditions over the northern hemisphere. *Earth System Science Data*, *14*, 865–884. doi: https://doi.org/10.5194/essd-14-865-2022

Ran, Y., Li, X., Cheng, G., Nan, Z., Che, J., Sheng, Y., … Wu, X. (2021). Mapping the permafrost stability on the tibetan plateau for 2005–2015. *Science China Earth Sciences*, *64*, 62–79. doi: https://doi.org/10.1007/s11430-020-9685-3

Semmler, T., Danilov, S., Gierz, P., Goessling, H. F., Hegewald, J., Hinrichs, C., … Jung, T. (2020). Simulations for cmip6 with the awi climate model awi-cm-1-1. *Journal of Advances in Modeling Earth Systems*, *12*, e2019MS002009. doi: https://doi.org/10.1029/2019MS002009

Sha, H., Lina, T., P, H. J., Yang, W., & Guofan, S. (2020). A commentary review on the use of normalized difference vegetation index (ndvi) in the era of popular remote sensing. *Journal of Forestry Research*, *32*, 1–6. doi: https://doi.org/10.1007/s11676-020-01155-1

Shen, C., Appling, A. P., Gentine, P., Bandai, T., Gupta, H., Tartakovsky, A., … Lawson, K. (2023). Differentiable modelling to unify machine learning and physical models for geosciences. *Nature Reviews Earth & Environment*, *4*, 552–567. doi: https://doi.org/10.1038/s43017-023-00450-9

Shen, M., Wang, S., Jiang, N., Sun, J., Cao, R., Ling, X., … Fu, B. (2022). Plant phenology changes and drivers on the qinghai–tibetan plateau. *Nature Re-*

views Earth & Environment, *3*, 633–651. doi: https://doi.org/10.1038/s43017-022-00317-5

Shi, S., Wang, P., Zhan, X., Han, J., Guo, M., & Wang, F. (2023). Warming and increasing precipitation induced greening on the northern qinghai-tibet plateau. *Catena*, *233*, 107483. doi: https://doi.org/10.1016/j.catena.2023.107483

Smith, S. L., O'Neill, H. B., Isaksen, K., Noetzli, J., & Romanovsky, V. E. (2022). The changing thermal state of permafrost. *Nature Reviews Earth & Environment*, *3*, 10–23. doi: https://doi.org/10.1038/s43017-021-00240-1

Song, L., Wang, L., Zhou, J., Luo, D., & Li, X. (2022). Divergent runoff impacts of permafrost and seasonally frozen ground at a large river basin of tibetan plateau during 1960–2019. *Environmental Research Letters*, *17*, 124038. doi: https://doi.org/10.1088/1748-9326/aca4eb

Stuenzi, S. M., Boike, J., Cable, W., Herzschuh, U., Kruse, S., Pestryakova, L. A., … Langer, M. (2021). Variability of the surface energy balance in permafrost-underlain boreal forest. *Biogeosciences*. doi: https://doi.org/10.5194/bg-18-343-2021

Stuenzi, S. M., Boike, J., Gädeke, A., Herzschuh, U., Kruse, S., Pestryakova, L. A., … Langer, M. (2021). Sensitivity of ecosystem-protected permafrost under changing boreal forest structures. *Environmental Research Letters*, *16*, 085045. doi: https://doi.org/10.1088/1748-9326/ac153d

Teng, H., Luo, Z., Chang, J., Shi, Z., Chen, S., Zhou, Y., … Tian, H. (2021). Climate change-induced greening on the tibetan plateau modulated by mountainous characteristics. *Environmental Research Letters*, *16*, 064064. doi: https://doi.org/10.1088/1748-9326/abfeeb

Ukkonen, P., & Mäkelä, A. (2019). Evaluation of machine learning classifiers for predicting deep convection. *Journal of Advances in Modeling Earth Systems*, *11*, 1784–1802. doi: https://doi.org/10.1029/2018MS001561

van der Kolk, H.-J., Heijmans, M. M. P. D., van Huissteden, J., Pullens, J. W. M., & Berendse, F. (2016). Potential arctic tundra vegetation shifts in response to changing temperature, precipitation and permafrost thaw. *Biogeosciences*, *13*, 6229–6245. doi: https://doi.org/10.5194/bg-13-6229-2016

Veigel, N., Kreibich, H., & Cominola, A. (2023). Interpretable machine learning reveals potential to overcome reactive flood adaptation in the continental us. *Earth's Future*, *11*, e2023EF003571. doi: https://doi.org/10.1029/2023EF003571

Wang, J., & Liu, D. (2022). Vegetation green-up date is more sensitive to permafrost degradation than climate change in spring across the northern permafrost region. *Global Change Biology*, *28*, 1569–1582. doi: https://doi.org/10.1111/gcb.16011

Wang, T., Yang, D., Yang, Y., Piao, S., Li, X., Cheng, G., & Fu, B. (2020). Permafrost thawing puts the frozen carbon at risk over the tibetan plateau. *Science Adcances*, *6*, eaaz3513. doi: https://doi.org/10.1126/sciadv.aaz3513

Wang, T., Yang, D., Yang, Y., Zheng, G., Jin, H., Li, X., … Cheng, G. (2023). Pervasive permafrost thaw exacerbates future risk of water shortage across the tibetan plateau. *Earth's Future*, *11*, e2022EF003463. doi: https://doi.org/10.1029/2022EF003463

Wang, T., Yang, D., Zheng, G., & Shi, R. (2022). Possible negative effects of earlier thaw onset and longer thaw duration on vegetation greenness over the tibetan plateau. *Agricultural and Forest Meteorology*, *326*, 109192. doi: https://doi.org/10.1016/j.agrformet.2022.109192

Wang, W., Rinke, A., Moore, J. C., Cui, X., Ji, D., Li, Q., … Decharme, B. (2016). Diagnostic and model dependent uncertainty of simulated tibetan permafrost area. *The Cryosphere*, *10*, 287–306. doi: https://doi.org/10.5194/tc-10-287-2016

Wang, W., Yang, K., Zhao, L., Zheng, Z., Lu, H., Mamtimin, A., … Moore, J. C.

(2020). Characterizing surface albedo of shallow fresh snow and its importance for snow ablation on the interior of the tibetan plateau. *Journal of Hydrometeorology*, *21*, 815–827. doi: https://doi.org/10.1175/JHM-D-19-0193.1

Wang, X., Ran, Y., Pang, G., Chen, D., Su, B., Chen, R., … Luo, D. (2022). Contrasting characteristics, changes, and linkages of permafrost between the arctic and the third pole. *Earth-Science Reviews*, *230*, 104042. doi: https://doi.org/10.1016/j.earscirev.2022.104042

Wang, Y., Xiao, J., Ma, Y., Ding, J., Chen, X., Ding, Z., & Luo, Y. (2023). Persistent and enhanced carbon sequestration capacity of alpine grasslands on earth's third pole. *Science Advances*, *9*, eade6875. doi: https://doi.org/10.1126/sciadv.ade6875

Wang, Z., Wang, Q., Zhao, L., Wu, X., Yue, G., Zou, D., … Zhang, Y. Z. . L. (2016). Mapping the vegetation distribution of the permafrost zone on the qinghai-tibet plateau. *Journal of Mountain Science*, *13*, 1035–1046. doi: https://doi.org/10.1007/s11629-015-3485-y

Wei, D., Qi, Y., Ma, Y., & Wang, X. (2021). Plant uptake of co_2 outpaces losses from permafrost and plant respiration on the tibetan plateau. *Proceedings of the National Academy of Sciences*, *118*, e2015283118. doi: https://doi.org/10.1073/pnas.2015283118

Wei, Y., Lu, H., Wang, J., Wang, X., & Sun, J. (2022). Dual influence of climate change and anthropogenic activities on the spatiotemporal vegetation dynamics over the qinghai-tibetan plateau from 1981 to 2015. *Earth's Future*, *10*, e2021EF002566. doi: https://doi.org/10.1029/2021EF002566

Westermann, S., Ingeman-Nielsen, T., Scheer, J., Aalstad, K., Aga, J., Chaudhary, N., … Langer, M. (2023). The cryogrid community model (version 1.0) – a multi-physics toolbox for climate-driven simulations in the terrestrial cryosphere. *Geoscientific Model Development*, *16*, 2607–2647. doi: https://doi.org/10.5194/gmd-16-2607-2023

Westermann, S., Langer, M., Boike, J., Heikenfeld, M., Peter, M., Etzelmüller, B., & Krinner, G. (2016). Simulating the thermal regime and thaw processes of ice-rich permafrost ground with the land-surface model cryogrid3. *Geoscientific Model Development*, *9*, 523–546. doi: https://doi.org/10.5194/gmd-9-523-2016

Wu, M., Chen, S., Chen, J., Xue, K., Chen, S., Wang, X., … Wang, Y. (2021). Reduced microbial stability in the active layer is associated with carbon loss under alpine permafrost degradation. *Proceedings of the National Academy of Sciences*, *118*, e2025321118. doi: https://doi.org/10.1073/pnas.2025321118

Wu, Q., & Zhang, T. (2008). Recent permafrost warming on the qinghai-tibetan plateau. *Journal of Geophysical Research: Atmospheres*, *113*, D13108. doi: https://doi.org/10.1029/2007JD009539

Wu, Q., & Zhang, T. (2010). Changes in active layer thickness over the qinghai-tibetan plateau from 1995 to 2007. *Journal of Geophysical Research: Atmospheres*, *115*, D09107. doi: https://doi.org/10.1029/2009JD012974

Wu, Q., Zhang, T., & Liu, Y. (2020). Thermal state of the active layer and permafrost along the qinghai-xizang (tibet) railway from 2006 to 2010. *The Cryosphere*, *31*, 417–428. doi: https://doi.org/10.1002/ppp.2059

Xia, Z., Huang, L., Fan, C., Jia, S., Lin, Z., Liu, L., … Zhang, T. (2022). Retrogressive thaw slumps along the qinghai–tibet engineering corridor: a comprehensive inventory and their distribution characteristics. *Earth System Science Data*, *14*, 3875–3887. doi: https://doi.org/10.5194/essd-14-3875-2022

Yan, F., Shangguan, W., Zhang, J., & Hu, B. (2020). Depth-to-bedrock map of china at a spatial resolution of 100 meters. *Scientific Data*, *7*, 2. doi: https://doi.org/10.1038/s41597-019-0345-6

Yang, J., Xin, Z., Huang, Y., & Liang, X. (2023). Multi-source remote sensing data shows a significant increase in vegetation on the tibetan plateau since 2000.

Progress in Physical Geography: Earth and Environment, *47*, 597–624. doi: https://doi.org/10.1177/03091333221148052

Yi, S., Wang, X., Qin, Y., Xiang, B., & Ding, Y. (2014). Responses of alpine grassland on qinghai–tibetan plateau to climate warming and permafrost degradation: a modeling perspective. *Environmental Research Letters*, *9*, 074014. doi: https://doi.org/10.1088/1748-9326/9/7/074014

Yin, G., Niu, F., Lin, Z., Luo, J., & Liu, M. (2021). Data-driven spatiotemporal projections of shallow permafrost based on cmip6 across the qinghai–tibet plateau at 1 km^2 scale. *Advances in Climate Change Research*, *12*, 814—827. doi: https://doi.org/10.1016/j.accre.2021.08.009

Zhang, G., Luo, W., Chen, W., & Zheng, G. (2019). A robust but variable lake expansion on the tibetan plateau. *Science Bulletin*, *64*, 1306–1309. doi: https://doi.org/10.1016/j.scib.2019.07.018

Zhang, G., Nan, Z., Hu, N., Yin, Z., Zhao, L., Cheng, G., & Mu, C. (2022). Qinghai-tibet plateau permafrost at risk in the late 21st century. *Earth's Future*, *10*, e2022EF002652. doi: https://doi.org/10.1029/2022EF002652

Zhang, G., Nan, Z., Zhao, L., Liang, Y., & Cheng, G. (2021). Qinghai-tibet plateau wetting reduces permafrost thermal responses to climate warming. *Earth and Planetary Science Letters*, *562*, 116858. doi: https://doi.org/10.1016/j.epsl.2021.116858

Zhang, Q., Kong, D., Shi, P., Singh, V. P., & Sun, P. (2018). Vegetation phenology on the qinghai-tibetan plateau and its response to climate change (1982–2013). *Agricultural and Forest Meteorology*, *248*, 408–417. doi: https://doi.org/10.1016/j.agrformet.2017.10.026

Zhang, X., & Li, X. (2023). Three-dimensional differentiation of the contribution of climatic factors to vegetation change in the pan-tibetan plateau. *Journal of Geophysical Research: Biogeosciences*, *128*, e2022JG007244. doi: https://doi.org/10.1029/2022JG007244

Zhang, Y., Li, B., & Zheng, D. (2014). Datasets of the boundary and area of the tibetan plateau. *Acta Geographica Sinica*, *69*, 65–68. doi: https://doi.org/10.11821/dlxb2014S012

Zhang, Z., Wu, Q., Jiang, G., Gao, S., Chen, J., & Liu, Y. (2020). Changes in the permafrost temperatures from 2003 to 2015 in the qinghai-tibet plateau. *Cold Regions Science and Technology*, *169*, 102904. doi: https://doi.org/10.1016/j.coldregions.2019.102904

Zhao, L., Zou, D., Hu, G., Wu, T., Du, E., Liu, G., . . . Cheng, G. (2021). A synthesis dataset of permafrost thermal state for the qinghai–tibet (xizang) plateau, china. *Earth System Science Data*, *13*, 4207–4218. doi: https://doi.org/10.5194/essd-13-4207-2021

Zhou, J., Zheng, Y., Song, C., Cheng, C., Gao, P., & Ye, S. (2022). *Vegetation map of qinghai tibet plateau in 1980s.* National Tibetan Plateau Data Center. doi: https://doi.org/10.11888/Terre.tpdc.272385

Zou, D., Zhao, L., Sheng, Y., Chen, J., Hu, G., Wu, T., . . . Cheng, G. (2017). A new map of permafrost distribution on the tibetan plateau. *The Cryosphere7*, *11*, 2527–2542. doi: https://doi.org/10.5194/tc-11-2527-2017

Potential vegetation changes in the permafrost areas over the Tibetan Plateau under future climate warming

Rui Chen[1,2], Jan Nitzbon[1], Thomas Schneider von Deimling[1], Simone Maria Stuenzi[1], Ngai-Ham Chan[1], Julia Boike[1,2], and Moritz Langer[1,3]

[1]Permafrost Research Section, Alfred Wegener Institute Helmholtz Centre for Polar and Marine Research, Potsdam, Germany
[2]Geography Department, Humboldt-Universität zu Berlin, Berlin, Germany
[3]Department of Earth Sciences, Vrije Universiteit Amsterdam, Amsterdam, the Netherlands

Key Points:

- By 2100, the permafrost areas will thaw at 0.23 ± 0.04 and $0.60 \pm 0.02 \times 10^6\,km^2$ under SSP1–2.6 and SSP5–8.5, respectively.
- By 2050, NDVI in the permafrost areas likely stay stable under SSP1–2.6 scenarios and likely show a rising trend under SSP5–8.5 scenarios.
- Surface air temperature and liquid water content at the root zone are the dominant features affecting NDVI changes in the permafrost areas.

Corresponding author: Rui Chen, `rui.chen@awi.de`

Abstract

Permafrost degradation on the Tibetan Plateau is well-documented and expected to continue throughout this century. However, the impact of thawing permafrost on the distribution, composition, and resilience of vegetation communities in this region is not well understood. In this study, we combined a transient numerical permafrost model with machine learning algorithms to project the near-future thermal state of permafrost and vegetation (represented by the Normalized Difference Vegetation Index [NDVI]) changes under two contrasting climate pathways (Shared Socioeconomic Pathway 1–2.6 [SSP1–2.6] and SSP5–8.5). The contribution of climatic and terrestrial variables to vegetation evolution was quantified using ridge regression. By 2100, permafrost areas were expected to decrease by $21 \pm 4\%$, and $55 \pm 2\%$ under the SSP1–2.6 and SSP5–8.5 scenarios, respectively, relative to the baseline period (2000–2018). Under the SSP1–2.6 scenarios, the mean annual ground temperature and active layer thickness were projected to fluctuate stably, while under the SSP5–8.5 scenarios, a significant increasing trend was anticipated. Satellite-based observations indicated an increasing trend of NDVI within the permafrost areas from 2000 to 2018 (0.01 per decade), mainly attributed to climatic factors. In the future, vegetation greenness was expected to possibly remain stable under SSP1–2.6 scenarios, whereas a rising trend was likely noted under SSP5–8.5 scenarios during 2019–2050, mainly controlled by the surface air temperature and liquid water content at the root zone during the growing season. Our modeling work provides a potential approach for investigating future vegetation changes and offers more possibilities to improve understanding of the interaction between soil-vegetation-atmosphere in cold regions.

Plain Language Summary

About 40% of the Tibetan Plateau is underlain by permafrost, which has undergone significant degradation and is estimated to experience substantial thawing by the end of this century. The thawing permafrost has impacted vegetation growth. To date, it has not been clear how the Normalized Difference Vegetation Index (NDVI; representing vegetation) changes with climate warming and permafrost degradation. Here, we used a land surface model and machine learning algorithms to simulate future permafrost thermal regimes and variations in the NDVI for future growing seasons and assess the most important variables influencing NDVI variability. We found that permafrost areas were projected to shrink by $21 \pm 4\%$ under the SSP1–2.6 scenarios and $55 \pm 2\%$ under the SSP5–8.5 scenarios by 2100, compared to the baseline period (2000–2018). Our results suggested that under mild climate conditions (SSP1–2.6), NDVI in the permafrost areas likely remained stable from 2019 to 2050, while NDVI in the permafrost areas likely showed an increasing trend under harsh climate conditions (SSP5–8.5), which was mainly due to increasing surface air temperature and liquid water content at the root zone on the Tibetan Plateau.

1 Introduction

The Tibetan Plateau (TP; Figure 1) hosts the world's most extensive high-altitude permafrost areas, estimated at $1.15 \times 10^6\,km^2$ (2005–2015) (Ran et al., 2021). Previous studies showed that permafrost had undergone significant degradation due to anthropogenic warming (Smith et al., 2022; X. Wang et al., 2022; Baral et al., 2023), as evidenced by increased mean annual ground temperature (MAGT) (Q. Wu & Zhang, 2008; Zhao et al., 2021), increased active layer thickness (ALT) (Q. Wu & Zhang, 2010; Qin et al., 2017), reduced permafrost thickness and areas (D. Guo & Wang, 2013; Ran et al., 2018), and altered geomorphological features (T. Gao et al., 2021; Xia et al., 2022). According to state-of-the-art Earth System Models (ESMs), the mean annual surface air temperature over the TP is projected to rise by $1.9\,^\circ C$ under the Shared Socioeconomic Pathway 1–2.6 (SSP1–2.6) and by as much as $6.3\,^\circ C$ under SSP5–8.5 by the end of the

21st century, relative to the baseline period of 1981–2010 (R. Chen, Li, et al., 2022). Such warming is expected to exacerbate the thawing and warming of the permafrost. Compared to the baseline period (2006–2015), the MAGT and ALT are estimated to increase by $0.8\,^{\circ}C$ to $2.6\,^{\circ}C$ and $0.7\,m$ to $3.0\,m$, respectively, in the period 2091–2100 under the SSP2–4.5 to SSP5–8.5 scenarios (G. Zhang et al., 2022), corresponding with a decline in permafrost areas by 44% to 71% (G. Zhang et al., 2022). This degradation is expected to cause major impacts on the carbon budget (Mu et al., 2020; T. Wang et al., 2020), hydrological dynamics (Song et al., 2022; T. Wang et al., 2023), ecosystem (Cuo et al., 2022; T. Wang et al., 2022), and infrastructure stability (Ran, Cheng, et al., 2022; R. Chen et al., 2023) on the regional scale. Vegetation covers approximately 81 % of the permafrost areas on the TP, rendering it the predominant surface characteristic (Z. Wang et al., 2016). With methodological innovations, sophisticated models, and a surge in observational data, our understanding of permafrost–vegetation interactions is improving (Heijmans et al., 2022). On the one hand, vegetation significantly influences the hydrothermal regime, carbon, and nutrient dynamics in permafrost environments. This influence is exerted through alterations in the surface energy balance (Chang et al., 2015; Stuenzi, Boike, Cable, et al., 2021), regulation of snow cover dynamics (Lawrence & Swenson, 2011; Grünberg et al., 2020), and impacts on both ecosystem carbon uptake (Ding et al., 2017; D. Wei et al., 2021) and ecosystem respiration processes (Gagnon et al., 2019; Prager et al., 2020). On the other hand, the evolution of permafrost significantly affects vegetation patterns, either promoting greening or browning (Myers-Smith et al., 2020). This is primarily mediated by its control over soil temperature and liquid water content in the root zone (Yi et al., 2014; de Vrese et al., 2023), alterations in landscape morphology (van der Kolk et al., 2016; Mu et al., 2017; Loranty et al., 2018), impacts on microbial stability (M. Wu et al., 2021), and influences on carbon and nitrogen cycling processes (Mekonnen et al., 2018; L. Liu et al., 2022; Mauclet et al., 2022).

Continuous vegetation greening and enhanced carbon uptake were also observed on the TP along with climate warming and permafrost degradation since the 1980s (Teng et al., 2021; Cuo et al., 2022; Shi et al., 2023; Z. Jin et al., 2023; Y. Wang et al., 2023). Notably, the Normalized Difference Vegetation Index (NDVI) exhibited an upward trend of 0.011 per decade from 1982 to 2015 (Teng et al., 2021). Similarly, the Enhanced Vegetation Index (EVI; which was developed to optimize the vegetation signal with improved sensitivity in high-biomass regions) increased by 0.01 per decade from 2000 to 2020 (Shi et al., 2023), and the Net Primary Productivity (NPP) demonstrated a positive trend of $0.51\,g\,C\,m^{-2}$ per decade from 1982 to 2014 (Cuo et al., 2022). While many studies have identified warming temperatures and increasing precipitation to be the main drives of greening (Teng et al., 2021; X. Li et al., 2022; T. Wang et al., 2022) and plant phenology changes (Q. Zhang et al., 2018; M. Shen et al., 2022; T. Wang et al., 2022) across the TP, vegetation greening on the global scale is thought to be mainly induced by CO_2 fertilization (Piao et al., 2020). In addition to the climatic factors, the hydrothermal conditions of the permafrost would also affect the vegetation dynamics through the permafrost-vegetation interactions (J. Wang & Liu, 2022; T. Wang et al., 2022). All of these studies have significantly improved our understanding of the characteristics and drivers of the vegetation greenness on the TP. However, it is still largely unknown how the vegetation cover will evolve under further destabilizing permafrost conditions on the TP accounting for future climate scenarios at a larger spatial scale. This uncertainty persists since the very complex vegetation physiological processes which are often tied to specific local conditions are not yet well represented in generalistic ESMs (Piao et al., 2020). With machine learning approaches increasingly being used to analyze complex spatiotemporal data and explore future environmental change (Pearson et al., 2013; Nitze et al., 2018; J. Guo et al., 2023; C. Shen et al., 2023), coupling the model-based and data-driven methods allows us to deal with the complex permafrost-vegetation interactions and quantify the vegetation dynamics and its dominant factors under different climate scenarios.

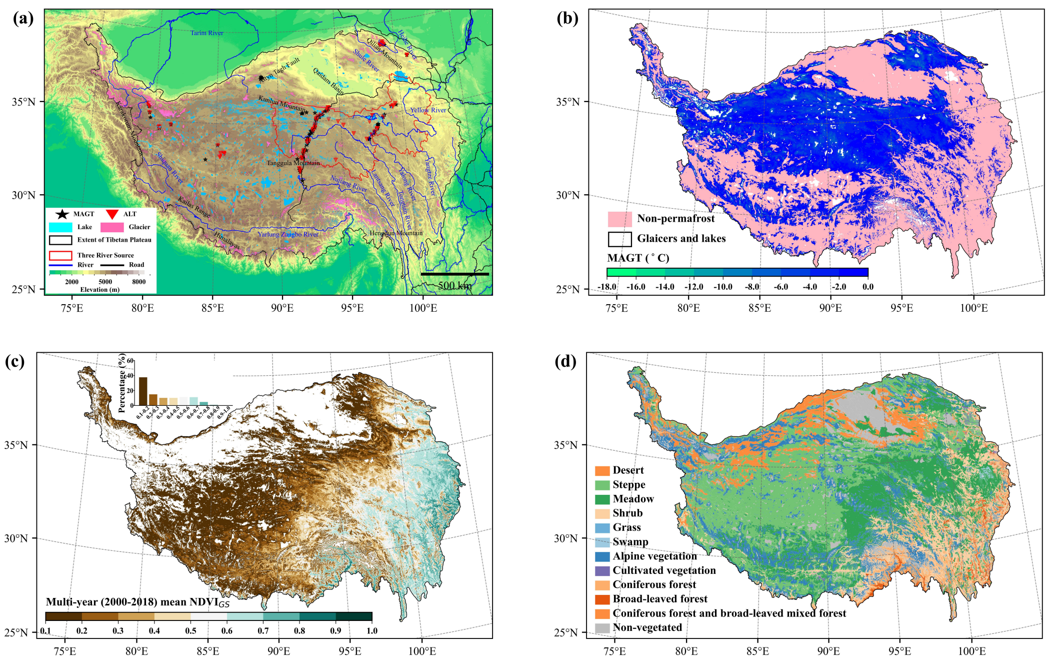

Figure 1. (a) Topography of study areas and location of observation sites over the Tibetan Plateau. Black stars and red triangles stand for the mean annual ground temperature (MAGT) and active layer thickness (ALT) of the monitoring sites, respectively. The digital elevation model, glacier, lake, river, and the boundary of the Tibetan Plateau data and the boundary of Three River Sources are obtained from the National Tibetan Plateau Data Center `https://data.tpdc.ac.cn` and are licensed under CC BY 4.0. The road data is available from the national 1:1000000 public basic geographic database of China (version 2017). (b) Spatial distributions of permafrost and non-permafrost areas on the Tibetan Plateau. Data source: (Obu et al., 2019). (c) Spatial distribution of the multi-year (2000–2018) mean of the growing season (May to September) NDVI on the Tibetan Plateau at 1km^2 scale from MODIS satellite imagery, the sub barplot represents the percentage of the number of grid cells of NDVI in each interval to the total number of grid cells. (d) Maps of vegetation types in the Tibetan Plateau adapted from the 1:1000000 vegetation map of China (Zhou et al., 2022)

In this study, we combined a physically-based permafrost model (CryoGridLite) (Langer et al., 2024) and machine-learning approaches for predicting the vegetation evolution (represented by the NDVI) over the permafrost areas on the TP. Firstly, we applied the CryoGridLite, driven by historical and future forcing datasets under the two different SSPs scenarios (SSP1–2.6 and SSP5–8.5) from two ESMs (AWI-CM-1-1-MR and MPI-ESM1-2-HR), to assess the potential shifts in permafrost distribution and its thermal state over the TP. Then, based on the output of the CryoGridLite model, we used machine-learning algorithms, which are Light Gradient Boosting Machine (LightGBM) (Ke et al., 2017) and Extreme Gradient Boosting Machine (XGBoost) (T. Chen & Guestrin, 2016), to quantify the prospective changes in NDVI within the permafrost areas of the TP. Finally, we elucidated the dominant factors influencing NDVI variations and quantified the contribution of each explanatory variable to the NDVI change.

2 Methods

2.1 CryoGridLite

We applied the one-dimensional transient permafrost model CryoGridLite (Langer et al., 2024) to simulate the trajectory of permafrost evolution over the TP. CryoGridLite was a fast version that was inherited from CryoGrid3 (Westermann et al., 2016) and the CryoGrid community model (Westermann et al., 2023), reducing computational costs and thus making it more suitable for regional (e.g., TP) to hemispherical scale (e.g., Pan-Arctic; Nitzbon et al. (2023)) permafrost modeling. In the following, we briefly describe the main aspects of CryoGridLite and provide the model setup for this work. Further detailed descriptions of model structures and physical processes can be found in Langer et al. (2024).

2.1.1 Model description

In this tailored version of CryoGridLite, we implemented the surface energy balance module, which was driven by the time series of forcing data (i.e. surface air temperature ($^\circ C$), rainfall and snowfall rate ($m\,h^{-1}$), ($kg\,kg^{-1}$), surface air pressure (Pa), incoming shortwave and longwave radiation ($W\,m^{-1}$), and wind ($m\,s^{-1}$)), to provide the upper boundary condition of the model (detailed description can be seen in Supporting Information Text S1.1). Unlike the heat condition equation implemented in CryoGrid3, the CryoGridLite used enthalpy instead of temperature as the state variable to solve the one-dimensional subsurface heat transfer:

$$\frac{\partial H}{\partial t} - \frac{\partial}{\partial z}(k(z,T)\frac{\partial T(H)}{\partial z}) = 0 \tag{1}$$

where $H\,(J\,m^{-3})$ is the volumetric enthalpy including sensible and latent heat contents of the ground, $t\,(s)$ is time, $z\,(m)$ is the vertical subsurface depth, $k\,(z,T)(W\,m^{-1}\,K^{-1})$ is the effective thermal conductivity derived from volumetric soil fractions of mineral, organic, water, ice and air in a given soil depth, and $T\,(k)$ is the ground temperature. The lower boundary condition was defined by constant geothermal heat flux. The implemented snowpack scheme allowed the model to simulate snow accumulation, ablation, melt-water routing, and refreezing within the snow cover. Once the snow had filled the first grid cell above the soil surface, the surface albedo changed from that of the soil to that of the fresh snow and decreased over time towards that of the albedo of old snow (Westermann et al., 2016). Besides, we applied a simple bucket scheme (a detailed description can be seen in Supporting Information Text S1.2) with only downward vertical water flow driven by gravity to compute the dynamics of soil water content rather than constant water contents used in (Langer et al., 2024).

2.1.2 Model setup

In this study, we synthesized the China Meteorological Forcing dataset (CMFD; selected period: 1979–2018 to represent historical climate conditions; resolution: 3 hours and $0.1^\circ \times 0.1^\circ$) (He et al. (2020); `https://www.tpdc.ac.cn`), along with two ESMs from CMIP6 (AWI-CM-1-1-MR and MPI-ESM1-2-HR; selected period: 2019–2100 to portray future climate conditions; resolution: monthly and $0.9375^\circ \times 0.9375^\circ$) (Müller et al. (2018); Semmler et al. (2020); `https://esgf-data.dkrz.de`) following the two SSP scenarios (SSP1–2.6 and SSP5–8.5) to construct the completely forcing data (period: 1979–2100; resolution: hourly and $0.1^\circ \times 0.1^\circ$). Compared with other ESMs, AWI-CM-1-1-MR, and MPI-ESM1-2-HR presented the best performance in depicting the spatiotemporal patterns of mean annual and seasonal surface air temperature on the TP in the past decades (R. Chen, Li, et al., 2022). To ensure model stability and consistency of the forcing data from 1979 to 2100, we performed a linear interpolation on the CMFD data from a 3-hour to an hourly resolution. Further, we utilized the approach from Westermann et al. (2016) by combining baseline climate data (from CMFD) with monthly climate anomalies (from ESMs) to generate the forcing data for this study. The time series of all forcing variables under the two SSPs and two ESMs for the period 1979–2100 is shown in Supporting Information Figure S1.

For the soil domain of the model, the vertical resolution of grid cells increased with thickness from the soil surface (0m) to the lower boundary of the model (100m) (0.02m in 0–2m depth; 0.05m in 2–4m depth; 0.1m in 4–10m depth; 0.2m in 10–20m depth; 1m in 20–30m depth; 5m in 30–50m depth; 10m in 50–100m depth). The soil stratigraphies were specified as mineral, organic, initial water/ice, and air volumetric fractions. The initial water/ice content according to Langer et al. (2023) was assumed halfway between field capacity and porosity for the soil layer above the water table depth, which was provided by a global groundwater table depths product (Fan et al. (2013); `https://thredds-gfnl.usc.es/thredds/catalog/GLOBALWTDFTP/catalog.html`), and saturated with the soil layer below the water table depth. The soil properties were derived from a new version of the global high-resolution dataset of soil hydraulic and thermal parameters dataset for land surface modeling (Y. Dai, Xin, et al. (2019); Y. Dai, Wei, et al. (2019); `https://globalchange.bnu.edu.cn`). The spatial resolution of this dataset was 0.00833° covering from 90°N to 90°S, 180°W to 180°E, and the vertical soil profile was provided in 8 layers (0–0.0451m, 0.0451–0.0906m, 0.0906–0.1655m, 0.1655–0.2891m, 0.2891–0.4929m, 0.4929–0.8289m, 0.8289–1.3828m and 1.3828–3.8019m). This dataset directly provided the volumetric fraction of soil organic matter and soil porosity. At the same time, mineral content and field capacity were calculated based on the approach in Y. Dai et al. (2013); Y. Dai, Xin, et al. (2019); Y. Dai, Wei, et al. (2019). Besides, we assumed the soil stratigraphy from 3.8019m to the bedrock depth Yan et al. (2020) was the same as that of the soil layer above it (i.e.1.3828–3.8019m). Below the bedrock depth, we assumed no soil organic matter existed, the soil porosity was arbitrarily set to 0.1, and the soil mineral content was set to 0.9. We utilized the geothermal gradient ($0.031\,^\circ C\,m^{-1}$; Y. Pang et al. (2022)) to interpolate the four-layer ERA5Land soil temperature (Muñoz-Sabater et al., 2021) in January 1979 to the whole soil profile as the initial ground temperature profile. The constant geothermal heat flux was extracted from the Terrestrial Heat Flow Dataset Lucazeau (2019) to describe the lower boundary condition.

To depict snowpack dynamics over time, five empty grid cells were set above the soil surface in the initial state to represent the maximum snow depth of 0.1m with a vertical resolution of 0.02m (Orsolini et al., 2019). We assumed a constant snow density (150 $\mathrm{kg\,m^{-3}}$) across the snowpack (L. Dai et al., 2018; Yin et al., 2021) and the fresh snow albedo was set to 0.82 (W. Wang et al., 2020). The parameters used in this study for model setup are summarized in the Supporting Information Table S1. We applied nearest-neighbor interpolation for all input datasets (detailed information is provided in Table 1) and further masked them with shape files of the boundary (Y. Zhang et al. (2014); `https://www.geodoi.ac.cn`), glaciers (W. Guo et al. (2015); `https://www.tpdc.ac.cn`), and lakes (G. Zhang et al. (2019); `https://www.tpdc.ac.cn`) of the TP to finalize the model setup for each grid cell in our simulations.

2.2 Machine learning model

In this study, we adopted two regression-based machine learning approaches to project the future NDVI change on the permafrost areas over the TP, which have been widely used in the prediction of future climate as well as environmental variables (Ukkonen & Mäkelä, 2019; Kondylatos et al., 2022; F. Chen et al., 2023; Veigel et al., 2023; C. Chen et al., 2024). The NDVI was collected from the Moderate Resolution Imaging Spectroradiometer (MODIS; MOD13A2; Didan (2015)) with a 1km spatial resolution from 2000–2018 to match up the period of CMFD and be regarded as the baseline period in this study. We processed the raw NDVI data to aggregate them into monthly intervals, which was the time resolution used in our machine learning approaches, using the maximum value composition approach (G. Pang et al., 2022) and further applied a Savitzky-Golay

Table 1. Overview of datasets used in this study

Datasets	Variable/Parameter	Reference/Source	Comments
China Meteorological Forcing Dataset	meteorological forcing	He et al. (2020)	Historical forcing 1979–2018
AWI-CM-1-1-MR MPI-ESM1-2-HR	meteorological forcing	Semmler et al. (2020) Müller et al. (2018)	Future forcing 2019–2100
Global high-resolution dataset of soil hydraulic and thermal parameters	Volumetric fractions of mineral, organic, porosity, and field capacity	Y. Dai, Xin, et al. (2019) Y. Dai, Wei, et al. (2019)	Soil stratigraphy
Global watertable depth dataset	Watertable depth	Fan et al. (2013)	Used to determine initial water/ice content
Terrestrial Heat Flow Dataset	Geothermal heat flux	Lucazeau (2019)	Lower boundary conditions
A Global Depth to Bedrock Dataset for Earth System Modeling	Bedrock depth	Yan et al. (2020)	Used to constrain soil depth
ERA5-Land	Four-layer soil temperature	Muñoz-Sabater et al. (2021)	Initial soil temperature
MODIS NDVI (MOD13A2, Version 6.1, 1km spatial resolution)	NDVI	Didan (2015)	Vegetation condition
Vegetation map from a digitized 1:1000000 vegetation atlas of China	Vegetation types	Zhou et al. (2022)	Analyzing NDVI changes and driving factors across various vegetation types

filter to smooth the NDVI time series (T. Wang et al., 2022). In addition, we assumed that there was no vegetation in the area with a multi-year (2000–2018) average growing season NDVI (from May to September, $NDVI_{GS}$; Teng et al. (2021)) lower than 0.1 (T. Wang et al., 2022). The spatiotemporal trend of $NDVI_{GS}$ over the TP (excluding the non-vegetation areas) from 2000 to 2018 based on the MODIS dataset is shown in the Supporting Information Figure S2. We incorporated six variables as explanatory factors in the machine-learning model based on previous studies (J. Wang & Liu, 2022; T. Wang et al., 2022; Y. Wang et al., 2023). Among them, surface air temperature (SAT), total precipitation (PRE), and incoming shortwave radiation (SIN) originated from climate-forcing data. Furthermore, the soil temperature (ST) and liquid water content (LWC) at the root zone (0–20cm; T. Wang et al. (2022)), and ALT are derived from the output of the CryoGridLite model for each grid cell. The time interval of these six variables was monthly, corresponding with the temporal resolution of the NDVI. The flow of the machine learning approach was as follows: First, the MODIS NDVI dataset and six explanatory variables that correspond with the same grid cell were divided into two groups: data from 2000 to 2014 served as the training dataset (about 80% of the data), and the remaining data (2015–2018) as the testing dataset (about 20% of the data). Then, according to the results from the CryoGridLite in the baseline period, we constructed the training and testing datasets on permafrost and non-permafrost areas (excluded ALT). For tuning the hyperparameters of each machine learning model in the training dataset in each area, we used Bayesian optimization (Python; Optuna package) with 500 iterations and set the early stopping and pruning strategy. The range of possible values for the part of hyperparameters and the final best hyperparameters can be seen in the Supporting Information Table S2. In each iteration, we used mean squared error as a scoring criterion and performed 5-fold cross-validation using the TimeSeriesSplit (Python; Scikit-learn package) approach due to there being a time dependence within the NDVI data. The optimal model parameter combinations resulting from each iteration were recorded and utilized to train the final model. Moreover, we introduced a weighting parameter for each model to enhance the model's emphasis on the growing season $NDVI_{GS}$ associated with individual grid cells. In comparison to the monthly NDVI values, our preference was for the model to exhibit superior performance when modeling the $NDVI_{GS}$ value. Similar to the hyperparameters used for each model, this weighting parameter was employed to obtain the optimal solution during the Bayesian optimization process. To evaluate the performance of each model, we employed root mean squared error (RMSE), bias (BIAS), coefficient of determination (R^2), and Kling-Gupta efficiency (KGE; Gupta et al. (2009)) as the evaluation metrics.

$$RMSE = \sqrt{\frac{1}{N}\sum_{i=1}^{N}(S_i - O_i)^2} \tag{2}$$

$$BIAS = \frac{1}{n}\sum_{i=1}^{n}(S_i - O_i) \tag{3}$$

$$R^2 = 1 - \frac{\sum_{i=1}^{n}(S_i - O_i)^2}{\sum_{i=1}^{n}(O_i - \bar{O})^2} \tag{4}$$

$$KGE = 1 - \sqrt{(r-1)^2 + \left(\frac{S}{O} - 1\right)^2 + \left(\frac{\sigma_S}{\sigma_O} - 1\right)^2} \tag{5}$$

where N is the number of validation data, S_i and $O_i (i = 1, 2, ..., N)$ are the values of simulated and observed data, respectively, S and O are the mean values of simulated and observed data, respectively, r is the Pearson correlation coefficient, σ_S, and σ_O are the standard deviations of simulated and observed data, respectively. We utilized the optimal machine learning model and future explanatory data to produce the NDVI for each grid cell within the permafrost and non-permafrost region over the TP.

2.3 Statistical analysis

We employed three indices including the MAGT ($^{\circ}C$), ALT (m), and permafrost areas (km^2) to quantify permafrost degradation. In this study, we obtained the MAGT from the depth of zero annual amplitude, which was typically at the 10–15m soil depth on the TP (Q. Wu & Zhang, 2010; Qin et al., 2017). We defined a grid cell as permafrost if its MAGT lies below the 0°C isotherm at the specific year (Ran, Li, et al., 2022). The ALT was quantified as the maximum thaw depth within the upper 10m of the subsurface (Langer et al., 2024) and there is no existing ALT and permafrost when the MAGT exceeds 0°C at the specific year at a grid cell. We employed the Albers Equal Area projection for area calculations to accurately represent permafrost areas. To better track the dynamics of vegetation conditions across the permafrost and non-permafrost areas on the TP, we used the annual NDVI_{GS} to represent the vegetation at individual years for each grid cell. In this study, we used ridge regression to robustly estimate the individual contributions of explanatory variables (mean or sum value at the growing season, i.e. SAT_{GS}, PRE_{GS}, SIN_{GS}, ST_{GS}, LWC_{GS}, and ALT_{GS}) to the variability in annual NDVI_{GS} across the permafrost and non-permafrost region (T. Wang et al., 2022; J. Li et al., 2023). This approach effectively mitigated the issue of multicollinearity inherent among the predictors. The incorporation of a regularization penalty term (λ) served to apportion variance across the coefficients efficiently, thereby enhancing the precision of the estimated impacts of the explanatory variables on NDVI_{GS}. Preceding the regression analysis, standardized explanatory variables and corresponding NDVI_{GS} served as inputs for the ridge regression model. The optimal regularization parameter, λ, was systematically determined through 5-fold cross-validation and the Grid Search algorithm, ensuring the most robust model performance. Variables exhibiting the largest absolute values of the regression coefficients post-regularization were interpreted as the dominant factors influencing NDVI_{GS} within the specific grid cells. A comprehensive range of the λ values explored during the model tuning phase was from 1×10^{-6} to 1×10^{6}. Besides, trend estimations of time series in this study were based on Sen's slope, which was selected over linear regression for its robustness against outliers and its nonparametric nature (Y. Wang et al., 2023). The flowchart of this study is shown in Figure 2.

3 Results

3.1 Model evaluations

3.1.1 CryoGridLite

For this study, we synthesized observational data, including MAGT and ALT, from a range of literature and public resources across the TP to assess the effectiveness of the CryoGridLite model (Q. Wu et al., 2020; H. Chen et al., 2015; J. Chen et al., 2016; Qin et al., 2017; Luo et al., 2018; Z. Zhang et al., 2020; Zhao et al., 2021; Mu & Peng, 2022; Y. Gao et al., 2023). Ultimately, we selected a total of $n_{MAGT} = 84$ and $n_{ALT} = 66$ different grid cells comprising 151 MAGT and 86 ALT data records within various permafrost regions of the TP from 2000 to 2015 in our model domain (Detailed information see Supporting Information Table S3). Figure 1 (a) displays the geographical distribution of these sites across the TP. For MAGT, we utilized the model output at the depth closest to the measured for comparison while for ALT, we considered the annual maximum thaw depth to compare the observed. Our modeling results indicated the simulated MAGT at most sites (53.6 %) in the range of $\pm 1^{\circ}C$ of the observed value (Figure 3 (a)), and there was a positive correlation between simulated and observed MAGT (Pearson correlation coefficient = 0.46, $p < 0.01$). However, we noted that our model tended to underestimate observed MAGT across the TP (Bias = -0.77 $^{\circ}C$), which could be attributed to inaccuracies of forcing, soil stratigraphy dataset, and imitated processes representation (Langer et al., 2024) and setting for the maximum snow height (0.1m). Overall, our model displayed the ability to reproduce the MAGT in the TP permafrost

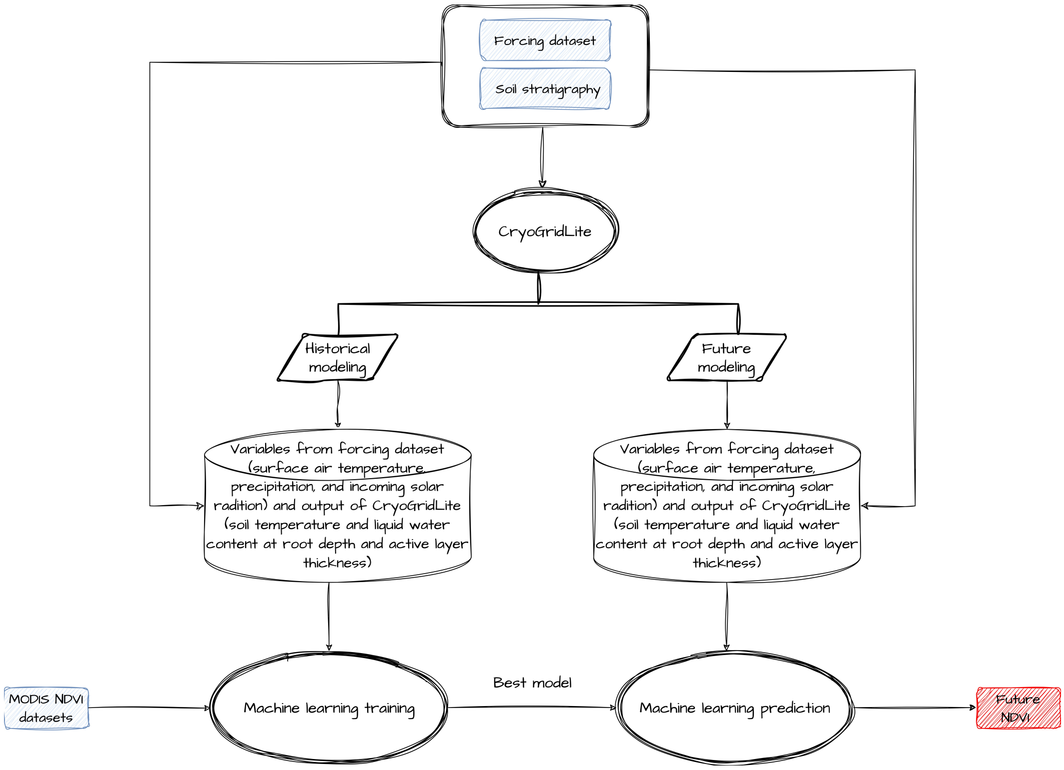

Figure 2. Flowchart of the process used to estimate the future vegetation change

areas well. Compared with the model capability on the MAGT, there was a poorer relationship between simulated and observed ALT, with a Pearson correlation coefficient of 0.17 (Figure 3 (b)). Similarly, the model exhibited a trend of underestimating the measured ALT compared to the observed values (Bias = -0.03 m), which aligns with the simulated cold bias for MAGT. The deviations between measured and modeled ALT were likely to be explained by inadequate forcing and soil dataset, shortcomings of the model (Langer et al., 2024), the cooling effect of shallow snow cover (0.1m), and high spatial heterogeneity of ALT on the TP (B. Cao et al., 2017; Ni et al., 2021). Nevertheless, our model reproduced the observed ALT on the TP, with modeled ALT deviations of $\pm 1\,m$ for most sites (59.1 %). A more detailed model evaluation was conducted for the soil temperature at upper soil depth across the TP due to the soil temperature at the root zone as an input index in machine learning (see Supporting Information Table S4 and Figure S3). In this research, CryoGridLite, driven by CMFD data, was employed to model the distribution of permafrost across the TP during the historical period (Figure 3 (c)). To demonstrate the capability of CryoGridLite to reproduce spatial permafrost occurrence, we juxtaposed our simulation results with five contemporary maps of permafrost distribution based on different approaches, thereby providing a comprehensive comparison and validation of our modeling results (Zou et al. (2017); Ran et al. (2018); Obu et al. (2019); Ni et al. (2021); Z. Cao et al. (2023); Figure 3 (d-h)). The comparison largely confirmed that the projected area of permafrost was consistent between our results and those of previous studies. Our modeling results indicated that the most likely permafrost areas on the TP were $1.10 \times 10^{6}\,km^2$ for the period 2000–2018 (excluding lakes and glaciers), which agreed well with other five studies (1.04–$1.28 \times 10^{6}\,km^2$). However, local differences were found between our results and other permafrost maps, which were most pronounced in the southern TP and along the southeast margin of the zone of continuous permafrost. It can be explained in several parts, first, spatial resolution and study period differences; lower resolutions (i.e., 0.1 °) make it difficult to capture the dynamics of permafrost changes at the boundaries of permafrost zones (Ni et al., 2021) and study period leads a slight discrepancy for the modeled results. Second, simulated approach differences; our results offer a dynamic, transient modeling perspective. In contrast, other models, such as the temperature at the top of the permafrost model and the surface frost number model, while simpler and requiring less data input, are not as equipped to capture transient effects or to project the evolution of permafrost accurately (Smith et al., 2022). Besides, the permafrost-modeled results of the machine learning model have data dependence and the risk of overfitting (Ni et al., 2021). Third, the definition of permafrost differences; we diagnose the absence or presence of permafrost relying on the MAGT at the zero depth of annual amplitude. Other studies adopt different criteria to determine the permafrost exists (e.g., the MAGT at the top of permafrost or the $10\,m$ depth). In summary, despite limitations our model provides a reasonable basis for describing spatially and temporally transient conditions of permafrost on the TP as input variable for the following analysis.

3.1.2 Machine learning model

We utilized the pre-partitioned test dataset to evaluate the performance of two machine-learning algorithms in modeling the NDVI_{GS} over the permafrost and non-permafrost areas of the TP (Figure 4). A comparison analysis of the two results (Figure 4 (a-b)) revealed that each algorithm proficiently captured the satellite-derived NDVI_{GS} values on the permafrost areas. The performance metrics (with $\text{R}^2 >= 0.65$, $\text{BIAS} <= 0.01$, $\text{RMSE} <= 0.08$, and $\text{KGE} >= 0.59$) suggested each model demonstrated robust capabilities in capturing the NDVI_{GS} dynamics over the permafrost regions of the TP. In comparison, the LightGBM model has better performance. Consequently, we selected the lightGBM model for further analysis of the spatial and temporal variability of NDVI_{GS} and its underlying drivers under different future climate scenarios. Additionally, complimentary assessments conducted for NDVI_{GS} over the non-permafrost areas underscored the simulation ability of both algorithms were remarkably similar and both can well repeat the changes in NDVI_{GS} (Figure 4 (c-d)).

3.2 Spatial and temporal patterns of the permafrost dynamics on the TP

To elucidate the spatiotemporal dynamics of permafrost variability on the TP throughout this century, we executed four distinct simulations driven by the AWI-CM-1-1-MR (Figure 5) and MPI-ESM1-2-HR (Supporting Information Figure S4) models, under both the SSP1–2.6 and SSP5–8.5 scenarios. Our findings revealed that spatial variability of permafrost distribution under the AWI-CM-1-1-MR, particularly by mid-century (2041–2060), manifested as a moderate reduction relative to the baseline period (2000–2018). This reduction was predominantly observed along the northern boundary of the continuous permafrost zone, southern regions of the TP, and the Three Rivers Sources (TRS) region (the red box in Figure 1 (a)), with negligible disparities between the lower and higher emission pathways (Figure 5 (a, c, e, g)). In contrast, by the end of the century (2081–2100), the majority of the permafrost areas were projected to remain relatively intact under SSP1-2.6, while areas that experienced permafrost thaw by mid-century continued to show visible degradation (Figure 5 (b, f)). Under a scenario of intensified climate warming, substantial thawing of existing permafrost was anticipated, particularly in the southwestern and southern parts of the TP, where the MAGT at the depth of zero annual amplitude was likely to approach or even exceed $0\ ^\circ C$ (Figure 5 (d, h)). The TRS region, in particular, was expected to undergo extensive permafrost degradation. Conversely, the northwestern areas of the Changtang Plateau and the Qilian Mountains were projected to maintain their permafrost coverage (Figure 5 (d, h)). In examining the projected changes in MAGT under the AWI-CM-1-1-MR, significant spatial heterogeneity

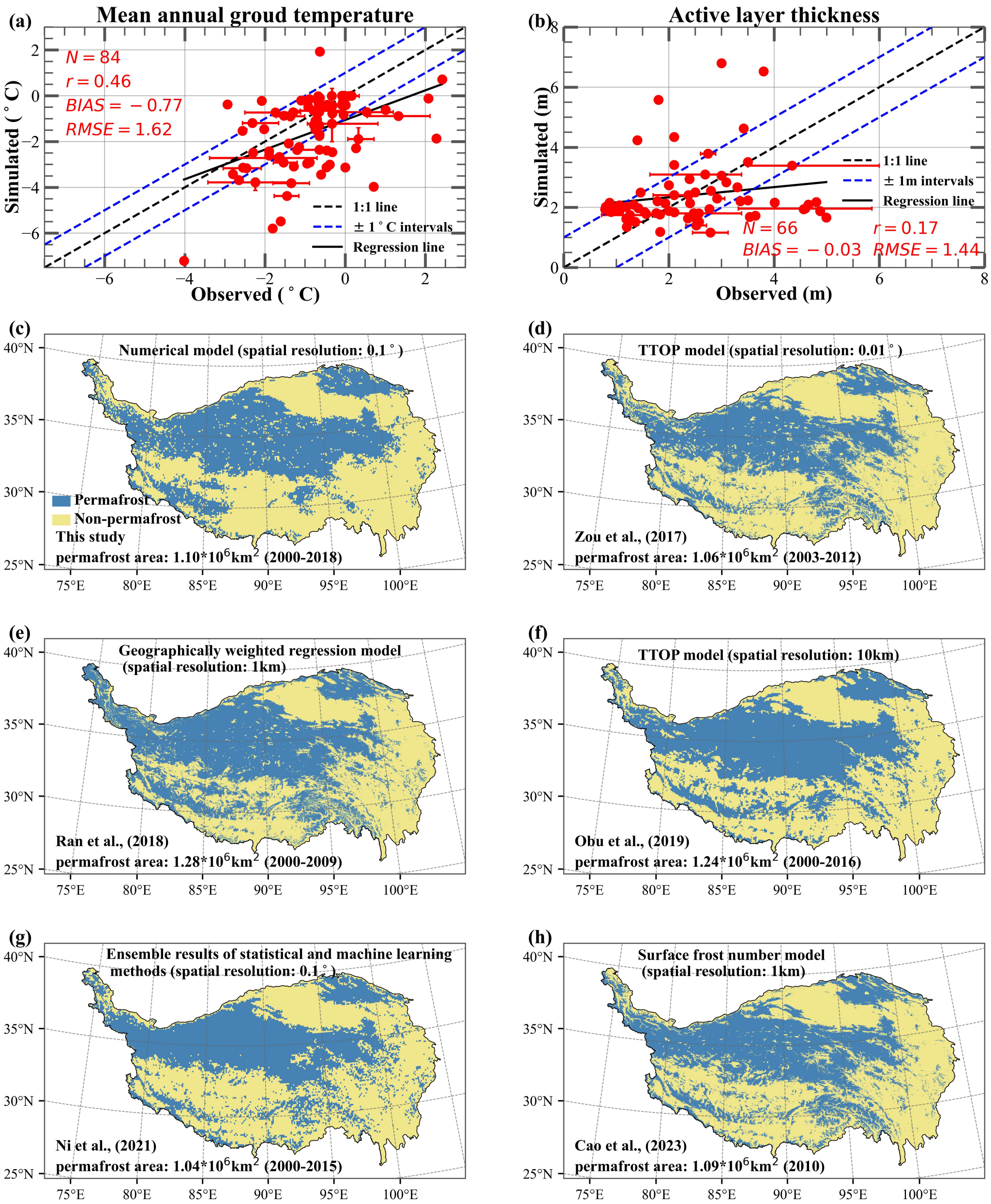

Figure 3. (a) Scatter plot illustrates the comparison results between the observed and simulated mean annual ground temperature (MAGT) for 151 records located within 84 different grid cells. (b) Scatter plot compares the observed and modeled active layer thickness (ALT) for 86 records located within 66 different grid cells. (c) Spatial distribution of permafrost during 2000–2018 over the Tibetan Plateau based on CryoGridLite model. (d-h) Spatial distribution of permafrost on the Tibetan Plateau from other studies. In (a) and (b), each point indicates the average value of observed and modeled MAGT/ALT in the same grid cell. The horizontal error bars represent the range of all observed MAGT/ALT located in the same grid cell, and vertical error bars indicate the range of simulated MAGT/ALT in the same grid cell.

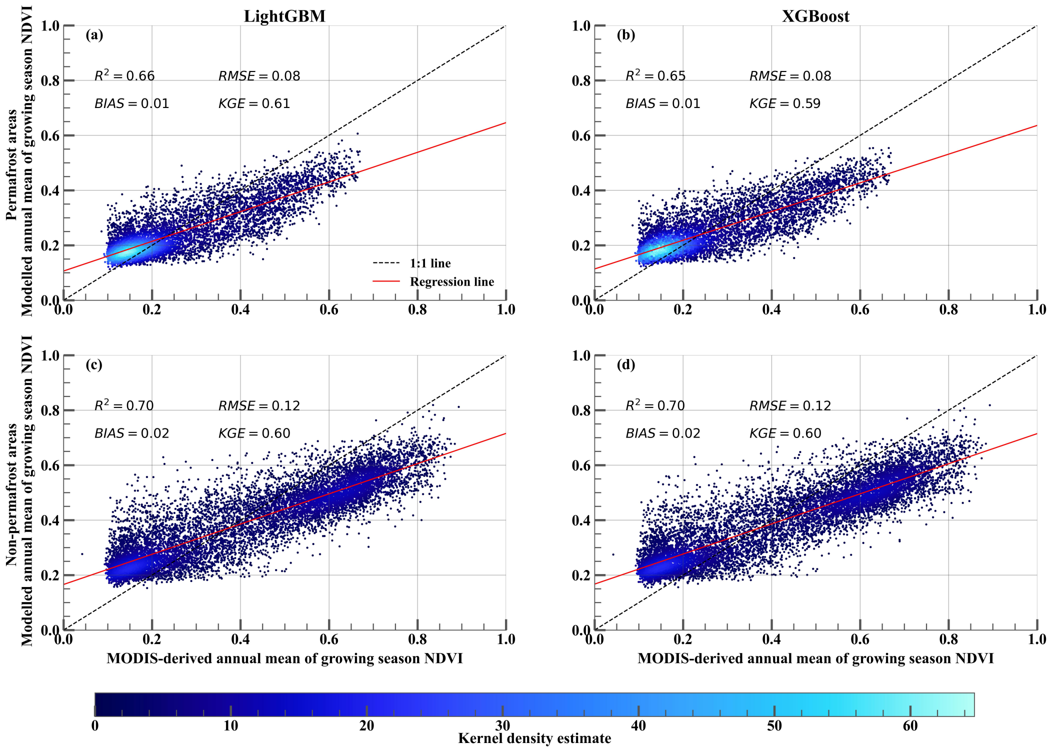

Figure 4. Density scatter plot for comparison between observed and modeled mean annual NDVI_{GS} in the permafrost and non-permafrost areas from 2015 to 2018. (a, c) LightGBM, (b, d) XGBoost. The black dashed line indicates a 1:1 line. The red line represents the regression line.

was observed across the permafrost regions. Under the SSP1–2.6 scenarios, this variability contrasted with the SSP5–8.5 scenarios; specifically, the eastern permafrost regions were trending warmer, whereas the central Changtang Plateau and the Pamir Mountains experiencing cooling trends (Figure 5 (a-b)). The future dynamics of MAGT in these permafrost areas were expected to be largely influenced by the extent of climatic warming (Figure 5 (c-d)). Figure 5 (e-h) depicts the changes in ALT across the permafrost areas on the TP under the AWI-CM-1-1-MR for both mid-century and end-century, under two contrasting scenarios, relative to the 2000–2018 baseline period. The pattern of ALT changes mirrored that of MAGT, with a notable increase in ALT observed in the TRS region and along the Qinghai-Tibet Engineering Corridor (QTEC), throughout the century under both scenarios. Therefore, additional actions are needed to maintain the stability of infrastructure in the QTEC in the future. However, in the western TP, the evolutionary trajectory of ALT was contingent upon the extent of climate warming, i.e. ALT was likely to decrease under stable climatic conditions, while it tended to increase in scenarios of ongoing climate warming. The spatial distribution of MAGT, ALT, and permafrost areas under both scenarios under the MPI-ESM1-2-HR was in correspondence with the results from AWI-CM-1-1-MR (Supporting Information Figure S4).

We further detected the time evolution of permafrost areas, MAGT, and ALT across the TP from 2019 to 2100 under SSP1–2.6 and SSP5–8.5 scenarios (Figure 5 (i-k)). The projected permafrost area consistently showed a decreasing trend across different climate scenarios; however, the rate of this decline varied. Permafrost areas decreased gradually from $1.06 \pm 0.00 \times 10^{6}\,km^2$ (mean ± standard deviation) to $0.87 \pm 0.04 \times 10^{6}\,km^2$ under SSP1-2.6 and $0.49 \pm 0.02 \times 10^{6}\,km^2$ under SSP5-8.5 during 2019–2100 at a rate of $-0.02 \pm 0.00 \times 10^{6}\,km^2$ per decade (SSP1-2.6) and $-0.07 \pm 0.00 \times 10^{6}\,km^2$ per decade (SSP5-8.5) under the lower and higher emission pathway, respectively (Figure 5 (i)). By 2100, the permafrost areas, under SSP1-2.6 and SSP5-8.5, were projected to decrease by $22 \pm 3\,\%$ and $56 \pm 2\,\%$, respectively, compared to the baseline period.

Figure 5 (j) presents the changes in MAGT during the period 2019–2100. Although projected MAGT based on AWI-CM-1-1-MR and MPI-ESM1-2-HR varies considerably under SSP1–2.6, MAGT increases slightly in the first half-century and decreases further until the end of the century, with insignificant changes in MAGT throughout the century. Under SSP5–8.5 scenarios, MAGT increased significantly to around $-1.0\,^{\circ}C$ by 2100. Relative to the mean MAGT ($-2.26 \pm 0.17\,^{\circ}C$) in the baseline period, MAGT decreased by about $-0.07 \pm 0.18\,^{\circ}C$ and $-0.26 \pm 0.15\,^{\circ}C$ under SSP1–2.6 by mid-century (2041–2060) and end-century (2081–2100), respectively, while, under SSP5–8.5, MAGT increases by about $0.28 \pm 0.03\,^{\circ}C$ and $1.20 \pm 0.05\,^{\circ}C$ by the period 2041–2060 and 2081–2100, respectively.

The time series of simulated ALT in the permafrost areas are shown in Figure 5 (k). The temporal variation of ALT was different in both climate scenarios. Under the lower emission pathway, ALT had no evident change throughout this century, while increasing to around 5.0 m by 2100 under severe climate warming. By the middle of this century, ALT in the permafrost areas of the TP increased by approximately 0.03 ± 0.17 m to 0.37 ± 0.07 m under SSP1–2.6 and SSP5–8.5 scenarios, respectively. However, ALT decreased by about 0.24 ± 0.11 m under SSP1–2.6 and increased by about 1.87 ± 0.14 m under SSP5–8.5 by the end of this century.

3.3 Spatial and temporal patterns of the vegetation in the permafrost areas on the TP

Analysis of satellite imagery data at the grid cell level (i.e. $0.1\,^{\circ}$) revealed that, during the period from 2000 to 2018, $NDVI_{GS}$ trends in the majority of permafrost areas (67.17%) on the TP did not exhibit significant changes (p-value > 0.05). A portion of the permafrost areas, constituting 31.55%, displayed an increase in $NDVI_{GS}$ (p-value <

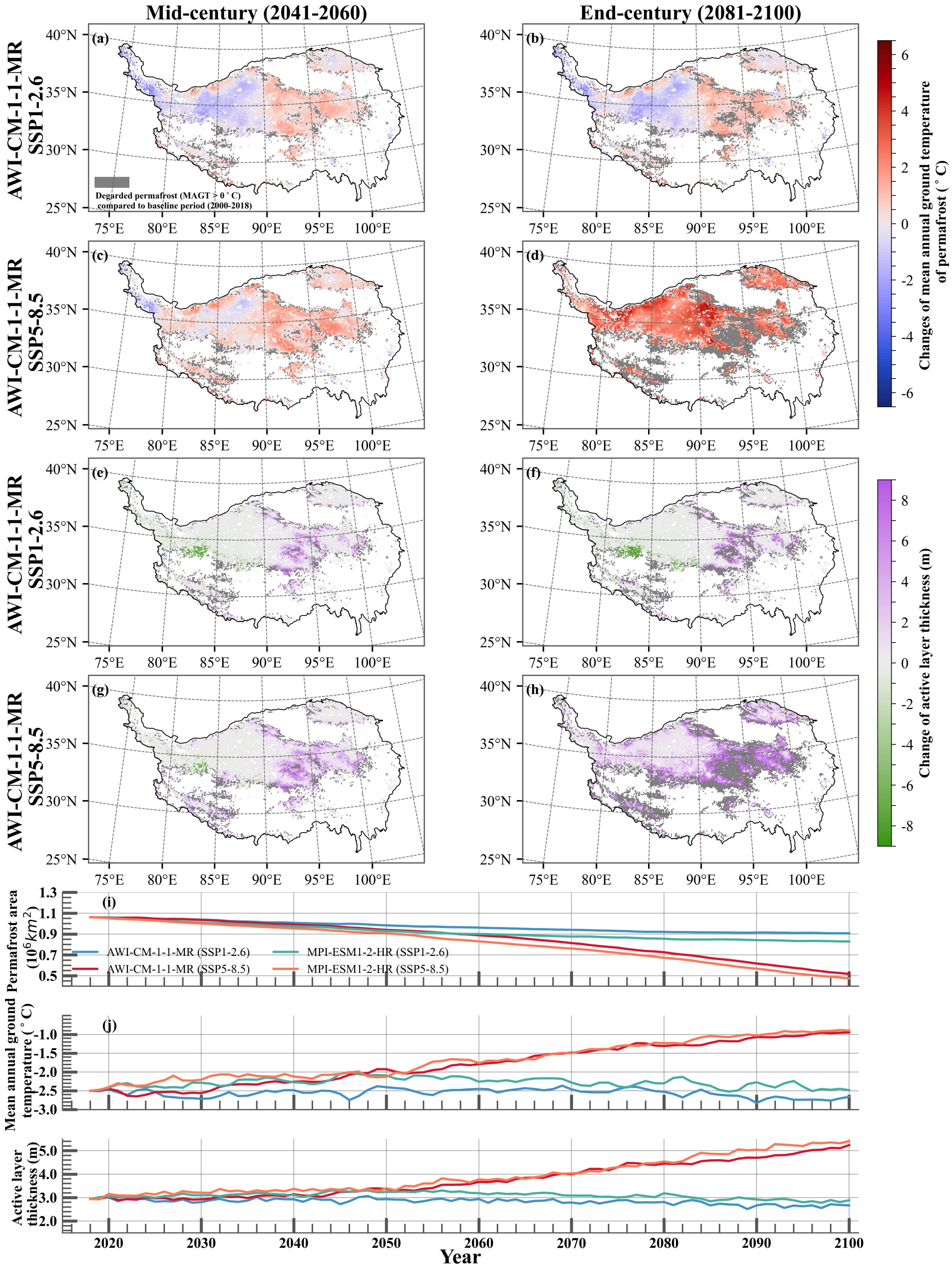

Figure 5. Spatial changes of the mean annual ground temperature (a-d) and active layer thickness (e-h) on the Tibetan Plateau by mid-century (2041–2060) and end-century(2081–2100) under SSP1–2.6 and SSP5–8.5 scenarios from AWI-CM-1-1-MR, related to the baseline period (2000–2018), respectively. (i-k) Time evolution of the changes in permafrost areas, mean annual ground temperature, and active layer thickness from 2019 to 2100 under the SSP1-2.6 and SSP5-8.5 scenarios. The grey area indicates degraded permafrost areas compared with the baseline by the mid-century (2041–2060) and end-century (2081–2100), and the blue, red, green, and orange lines represent the SSP1–2.6 and SSP5–8.5 scenarios from AWI-CM-1-1-MR and SSP1–2.6 and SSP5–8.5 scenarios from MPI-ESM1-2-HR, respectively.

0.05), whereas a minimal area, representing only 1.28% experienced a decline in NDVI$_{GS}$ (p-value < 0.05) (Figure 6 (c)). Within the non-permafrost areas, 18.96% and 2.24% proportion of the area experienced an increased and decreased NDVI$_{GS}$, respectively, during the same period (Figure 6 (d)). Although we utilized data from both permafrost and non-permafrost areas across all grid cells to construct our training dataset, the predictive accuracy for extrapolations beyond the training data range was notably constrained, especially under the high-emission SSP5–8.5 scenarios, due to the inherent data dependency in machine learning. To enhance the robustness of our future NDVI change simulations, we narrowed down our predictions to 2050. Our machine learning analysis, based on the SSP1–2.6 scenarios using two ESMs, indicated a stable NDVI$_{GS}$ (ensemble mean) across the permafrost areas, with no significant alterations anticipated from 2019 through 2050 (p-value > 0.05), maintaining an average NDVI$_{GS}$ of 0.25 ± 0.03 (Figure 6 (a); blue and green line). Spatial distribution analysis of the mean annual NDVI$_{GS}$ trend under both ESMs showed no considerable shifts in vegetation conditions over 85–97% of the permafrost regions up to the middle of the century (Figure 6 (e) and Supporting Information Figure S5 (a)), this stability likely attributable to the relatively stable climatic conditions associated with lower emission trajectories. In contrast, under the SSP5–8.5 scenarios, results from the Mann-Kendall test suggested a marginally increasing trend in the ensemble mean of the NDVI$_{GS}$ anomaly time series ($0.05 <$ p-value < 0.10), with a rate of 0.01 ± 0.00 per decade (Figure 6 (a); orange and red line). Moreover, over 7–29% of the permafrost areas exhibited increased NDVI$_{GS}$, while a significant decrease in NDVI$_{GS}$ was observed in only about 0.33–1.17% of the area under both scenarios (Figure 6 (g) and Supporting Information Figure S5 (c)). Consequently, our findings hint at a potential slightly increased NDVI$_{GS}$ within the permafrost areas over the TP, amidst the ongoing severe climate warming projected by the middle of the century. Figure 6 (b, f, h) and Supporting Information Figure S5 (b, d) outline the time series of the NDVI$_{GS}$ anomaly and spatial distribution of the mean annual NDVI$_{GS}$ trend across the non-permafrost areas. From 2019 to 2050, the ensemble mean of the time series for mean annual NDVI$_{GS}$ anomaly in the majority of non-permafrost areas was expected to remain relatively stable under SSP1–2.6 scenarios (p-value > 0.05), while a slight increase in NDVI$_{GS}$ trend, similar with the permafrost areas, is anticipated under SSP5–8.5 scenarios ($0.05 <$ p-value < 0.10). Spatially, 1.90–5.03% permafrost and 6.10–8.77% non-permafrost areas showed an increasing trend under the SSP1–2.6 and SSP5–8.5 scenarios, respectively. In summary, NDVI$_{GS}$ trends in most permafrost and non-permafrost areas were expected to remain stable under lower emission pathways till the midpoint of this century. Conversely, under higher emission pathways, NDVI$_{GS}$ was likely to exhibit an increasing trend in permafrost and non-permafrost areas. According to the vegetation types dataset of the TP Zhou et al. (2022), the alpine meadow and alpine steppe constituted the primary vegetation in the permafrost areas. We further detected the annual NDVI$_{GS}$ change for different vegetation types (alpine steppe and alpine meadow) in the permafrost areas (Supporting Information Figure S6). Our results showed that areas with increased mean annual NDVI$_{GS}$ outnumbered those with decreased mean annual NDVI$_{GS}$ for both vegetation types, although the extent of this disparity varied under the two scenarios.

3.4 Important features of spatiotemporal variability of the vegetation in the permafrost areas on the TP

The evolution of vegetation is influenced by an interplay of various climatic and terrestrial factors (Hawinkel et al., 2016; Y. Wei et al., 2022; Higgins et al., 2023). We performed ridge regression for both permafrost and non-permafrost areas to identify the absolute values of the contribution of each explanatory factor and detect the most important variables to NDVI$_{GS}$ change. For the baseline period, climate variables (i.e. SAT$_{GS}$, PRE$_{GS}$, and SIN$_{GS}$) contributed notably (59.34% of permafrost areas and 68.65% of non-permafrost areas) to the NDVI$_{GS}$ change, specifically, the contribution of SAT$_{GS}$ was the largest (22.99%) in the permafrost and was the secondary important factor (21.53%)

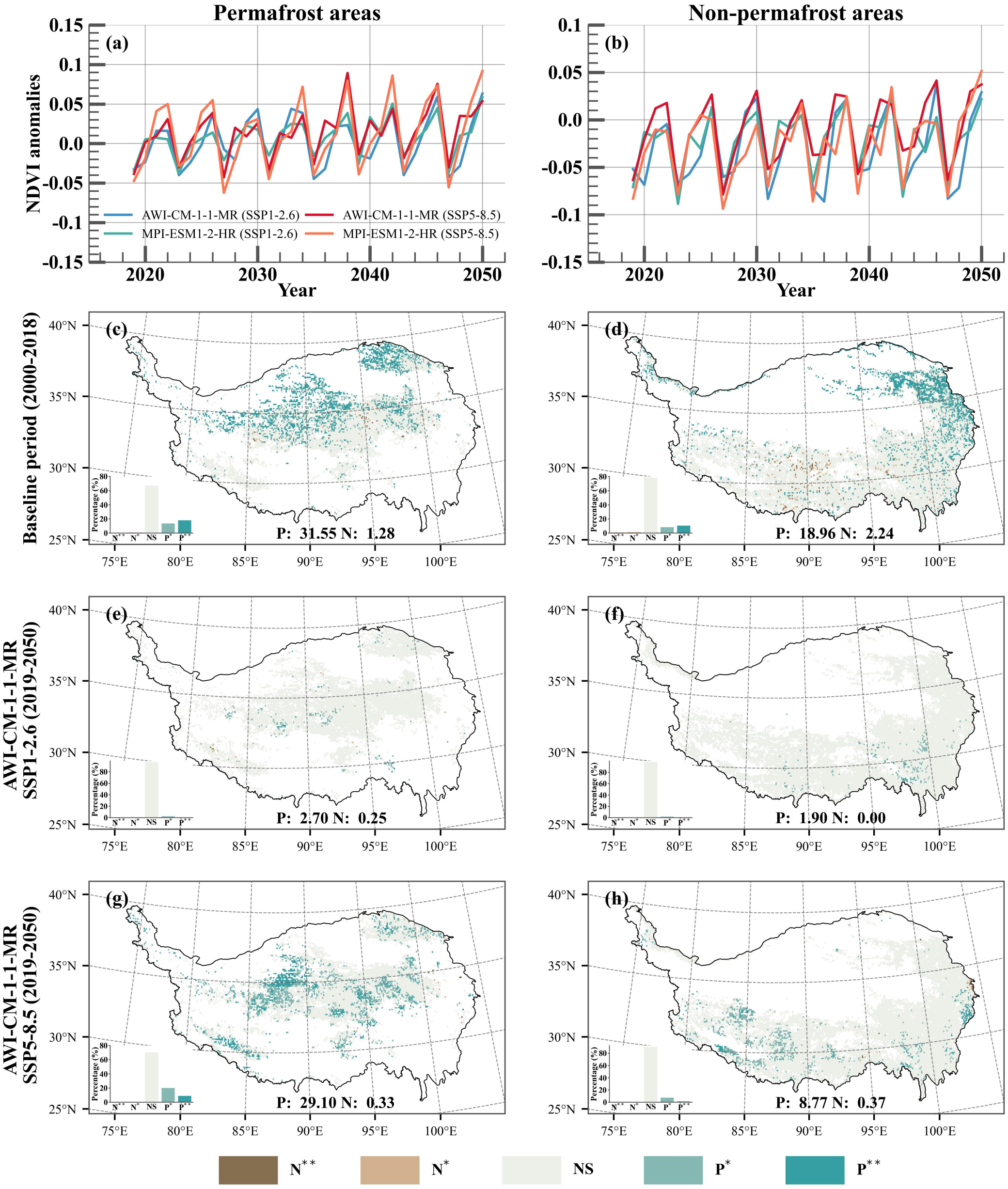

Figure 6. (a-b) Time series of mean annual NDVI$_{GS}$ anomalies (minus the mean value during 2000–2018) from 2019 to 2050 under the future climate conditions on the permafrost and non-permafrost areas over the TP. The blue, red, green, and orange lines represent SSP1–2.6 and SSP5–8.5 scenarios from AWI-CM-1-1-MR and MPI-ESM1-2-HR, respectively. (c-h) Spatial patterns of mean annual NDVI$_{GS}$ trend across the permafrost and non-permafrost areas during the baseline (2000–2018) and future periods (2019–2050) under different climate scenarios from AWI-CM-1-1-MR. N, NS, and P indicate negative, non-significant, and positive trends. * and ** represent significance at p-value < 0.05 and 0.01, respectively

in the non-permafrost area of the plateau, the PRE_{GS} was identified as the third important factor and made similar contributions (17.52% and 19.67%) in the permafrost and non-permafrost areas, the SIN_{GS} had more contributions to the NDVI_{GS} change in the non-permafrost areas (27.45%) than that of in the permafrost areas (18.84%) (Figure 7 (a-d)). For the terrestrial variables (i.e. ST_{GS}, LWC_{GS}, and ALT_{GS} [excluded in non-permafrost areas]), they contributed to the NDVI_{GS} change of approximately 40% of the permafrost areas and 30% of the non-permafrost areas. We used the same method to examine the dominant factors controlling the change of annual NDVI_{GS} during 2019–2050 under different climate scenarios and different ESMs (Figure 7 (e-l) and Supporting Information Figure S7 (a-h)). The results revealed that predominant factors affecting the future NDVI_{GS} changes in permafrost and non-permafrost areas under the different scenarios remained largely consistent. That is, under the SSP1–2.6 and SSP5–8.5 scenarios, it was found that SAT_{GS} and LWC_{GS} emerged as the primary determinants of the interannual variability in NDVI_{GS} across permafrost areas, influencing between 61.24% and 76.26% of these areas. In non-permafrost areas on the TP, SIN_{GS} was identified as the predominant driver behind NDVI_{GS} interannual variability, affecting 33.38% to 45.59% of the areas under both scenarios. Supporting Information Figure S8 depicts the spatial patterns and relative importance of each explanatory variable across diverse vegetation types. The NDVI_{GS} interannual variation in both vegetation types was responsive to variations of climatic factors in the baseline period (approximately 60%). Aiming at the future periods, SAT_{GS} and LWC_{GS} explained a much larger portion of the NDVI_{GS} variations than other factors in both vegetation types (Supporting Information Figure S8 (e-l)). Overall, the interannual variability of the NDVI_{GS} tended to be predominantly controlled by the climate variables in both permafrost and non-permafrost areas from 2000 to 2018. Compared to the baseline period, our study indicated that SAT_{GS}, LWC_{GS} and SIN_{GS} were the main contributors to the NDVI_{GS} change in the permafrost and non-permafrost areas in the future periods (Figure 7 (e-l), Supporting Information Figure S7 (a-h)). Consequently, surface air temperature, liquid water content at the root zone, and incoming solar radiation played an important role in future NDVI_{GS} evolution on the TP.

4 Discussion

4.1 Comparison with previous modeling studies of the permafrost state and vegetation conditions on the TP

In this study, we utilized a computationally efficient numerical permafrost model (CryoGridLite) driven by climatic forcing data to simulate the thermal state of permafrost and ALT over the TP from 1979 to 2100. Table S5 summarizes the simulation results of the thermal state of permafrost and ALT on the TP under present and future climate conditions in the past 10 years based on different approaches. For the historical period, our results fell within the range of these studies for the permafrost state (MAGT: [-3.32° C, -1.35° C]; Permafrost areas: [$1.01 \times 10^6\,km^2$, $1.66 \times 10^6\,km^2$]) and ALT [1.24m, 3.23m]. As previously mentioned, the differences among these simulation results can be attributed to spatial resolution and study period, study approaches, and the definition of the permafrost state and ALT, etc. For the future period, although there were variations in magnitude and trends for the permafrost state and ALT between our study and others, all demonstrated that permafrost degradation over the TP would be an inevitable consequence in the 21st century under the SSP5–8.5/Representative Concentration Pathway (RCP) 8.5 scenarios. Meanwhile, under the SSP1–2.6/RCP2.6 scenarios, permafrost was anticipated to exhibit relative stability or only slight warming until the end of the century and was most likely aggradation in the northwest of the plateau due to the cooling surface air temperature under the SSP1-2.6 scenarios. In addition to the reasons mentioned above, the divergence in projections could largely be explained by the disparities among the ESMs employed in these studies. For instance, G. Zhang et al. (2022) used

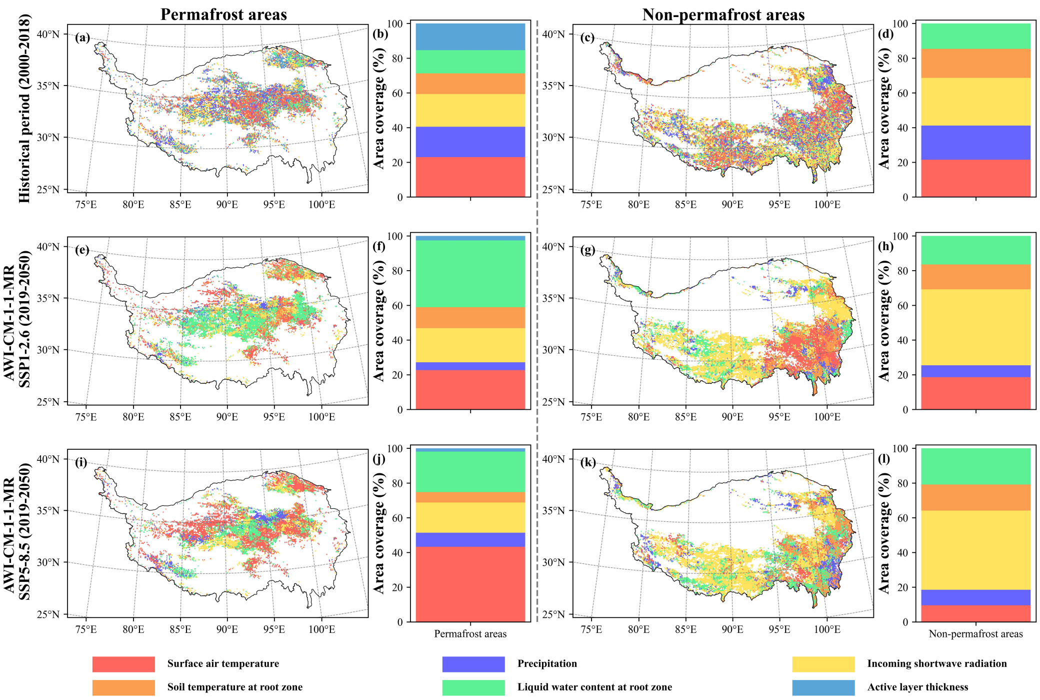

Figure 7. Spatial distribution of the dominant factors to the $NDVI_{GS}$ changes over different periods in the permafrost and non-permafrost areas. (a, c) Baseline period (2000–2018). (e, g) Future period (SSP1–2.6; AWI-CM-1-1-MR). (i,k) Future period (SSP5–8.5; AWI-CM-1-1-MR). The barplot (b, d, f, h, j, l) represents the proportion of the contribution of each variable in the permafrost and non-permafrost areas under AWI-CM-1-1-MR.

the Noah-LSM driven by five ESMs to project permafrost stability on the TP throughout this century. Their findings revealed significant variances among the ESMs' projections under identical scenarios (e.g. under the SSP5-8.5 scenarios, simulations driven by CESM2 and EC-Earth3 suggested that permafrost was highly likely to vanish by 2100, while, projections based on MPI-ESM1-2-HR (also used in our study) indicated that approximately $0.5 \times 10^{6}\, km^2$ (similar with our results) of permafrost might persist by the end of the century).

To project the NDVI in the future on the TP, we employed statistical models trained by machine-learning algorithms under two contrasting climate scenarios in this study. For the historical period (2000–2018), MODIS imagery indicated that the $NDVI_{GS}$ showed an increasing trend over the TP, with a rate of 0.01 per decade, and 24% proportion of the area covered by plants exhibits greening (Supporting Information Figure S2 (a-c)). In addition to the MODIS NDVI data, other ecological indicators (e.g. LAI, NPP, EVI, fractional vegetation coverage [FVC]) demonstrated that vegetation greenness increased on the TP since 2000 (Piao et al., 2020; M. Shen et al., 2022; Yang et al., 2023; X. Zhang & Li, 2023). Regarding vegetation evolution in the future, although few studies have elucidated the magnitude and trends of NDVI in the permafrost areas on the TP (H. Li et al., 2024), studies based on other vegetation factors and methods showed that under the background of future climate change, there was a potential for vegetation greening on the TP (Q. Gao et al., 2016; Mahowald et al., 2016; W. Liu et al., 2020; Cuo et al., 2022; M. Shen et al., 2022; Kong et al., 2023), which aligns with our study. For example, Q. Gao et al. (2016) and Cuo et al. (2022) applied the Lund-Potsdam-Jena dynamic global vegetation model (LPJ-DGVM) to quantify the annual NPP changes on the TP under CMIP5/CMIP6 scenarios. Their findings indicated a general increase in annual NPP, with a notable shift in the dominant vegetation, as alpine shrubs are projected to replace alpine meadows and steppes. The simulation results from ESMs (CMIP5) and regional climate models indicated a continued increasing trend of LAI by the end of the century in the northern temperate region (25–50° N: including the TP) and TP (Mahowald et al., 2016; W. Liu et al., 2020). Kong et al. (2023) constructed a framework of machine learning algorithms to predict the evolution trajectory of FVC in China under four SSP scenarios from 2019 to 2060, with FVC showing an increasing trend except for the east region of China. H. Li et al. (2024) indicated that under the various climate scenarios, along with significant permafrost degradation, the TP exhibited a greening (NDVI) trend in vegetation which persists until the end of the century. In addition to employing the vegetation indices to analyze future vegetation greenness, a recent review summarized the potential plant phenology changes on the TP in this century, which included the advanced start of the growing season and the delayed end of the growing season, causing vegetation greening on the TP (M. Shen et al., 2022). Besides, we would like to point out that there are ongoing debates regarding the continued vegetation greening phenomenon that occurs on the TP and the prospect of the TP becoming a net carbon sink in the future, especially considering carbon released by thawing permafrost and enhanced soil and plant respiration (X. Jin et al., 2021; D. Wei et al., 2021; Ehlers et al., 2022; T. Wang et al., 2022). Consequently, an enhanced focus on the vegetation conditions within the permafrost regions of the Tibetan Plateau is warranted in future studies.

4.2 Important features of vegetation greening

In our study, we used ridge regression to discern the absolute values of the contributions of the driving factors for the NDVI changes on the TP. For the baseline period, the climatic variables were the important features of $NDVI_{GS}$ on the TP in both permafrost (approximately 60%) and non-permafrost areas (approximately 70%) (Figure 7, Supporting Information Figure S7). Piao et al. (2020) noted that dynamic global vegetation models suggested that CO_2 fertilization (a phenomenon widely acknowledged for enhancing vegetation growth) continued to be the predominant factor driving vegetative greening on a global scale. However, in northern high latitudes and the TP, it is the increasing temperatures that primarily contributed to the observed greening trends (LAI). Statistical analysis (Teng et al., 2021; X. Li et al., 2022; M. Shen et al., 2022; T. Wang et al., 2022) and sensitivity experiments (Y. Wang et al., 2023) also demonstrated that climate change played an important role in vegetation growth over the past 40 years on the TP, albeit with contributions of varying magnitudes. This variability in quantitative contributions was attributed to the differential impact of various input explanatory variables (e.g. climate variables, terrain, soil properties) and different data sources (e.g. MODIS data, Global Inventory Modeling and Mapping Studies NDVI product [GIMMS NDVI], and SPOT VEGETATION imagery [SPOT-VEG NDVI]). For the future period, our findings indicated that, compared with the baseline period, NDVI_{GS} showed a potential increasing trend likely occurring in the permafrost areas under the SSP5–8.5 scenarios, mainly attributed to the change of SAT_{GS} and LWC_{GS}. Supporting Information Figure S9 and S10 indicate the spatiotemporal distribution of LWC_{GS} and SAT_{GS} in the permafrost areas from 2019 to 2050. In the vast majority of permafrost regions, both the SATGS and the LWCGS have exhibited an increasing trend. This was in agreement with the results from J. Gao et al. (2017), who combined the LPJ-DGVM with the geographical regression, and R. Cao et al. (2023), who conducted multiple sensitivity experiments based on machine learning algorithms. All indicated that temperature would more significantly affect vegetation changes over the TP. One potential explanation is that warmer temperatures extend the duration of growing seasons, enhance photosynthetic activity, and lead to greater biomass accumulation ((J. Gao et al., 2017; X. Li et al., 2022; M. Shen et al., 2022)). Additionally, our results emphasized the important role of LWC_{GS} in vegetation growing in the permafrost areas. Besides, it is important to acknowledge that in this study we only considered the impact of a few variables on NDVI_{GS} change over the TP, without taking into account other factors. Future studies should synthesize more driving factors and implement more analysis methods (e.g. partial correlation analysis or structural equation model) to improve our understanding of the vegetation change on the TP.

4.3 Model limitation and uncertainty

While the CryoGridLite model capably replicates the mean state (Figure 3 (a-b), Table S4) and temporal evolution (Supporting Information Figure S3) of the permafrost thermal regime across the TP, there is a need for further development and enhancements to diminish the uncertainty of simulations. For instance, the single offline simulation driven by singular meteorological forcing data (He et al., 2020) and soil stratigraphy datasets (Y. Dai, Xin, et al., 2019; Y. Dai, Wei, et al., 2019) and a fixed maximum snow depth (i.e., 0.1 m) and snow density (i.e., $150\,kg\,m^{-3}$) for all grid cells may introduce a large degree of uncertainty for simulation (W. Wang et al., 2016; Lu et al., 2020; Langer et al., 2024). Hence, conducting ensemble parameter simulations (including forcing, soil, and snow properties datasets) should be the direction of our subsequent research endeavors (Nitzbon et al., 2023; Langer et al., 2024). This approach is crucial for a more accurate quantification of the permafrost thermal state across the TP. Furthermore, compared with Nitzbon et al. (2023) and Langer et al. (2024), in this tailored version of CryoGridLite, we implemented the surface energy balance (Supporting Information Text S1.1) and "bucket" scheme (Supporting Information Text S1.2) to calculate the dynamics of upper boundary conditions and groundwater changes, respectively. However, as pointed out by Langer et al. (2024), the model calculated the ground freezing by an enthalpy–temperature relation of free water instead of accurate soil freezing characteristic curves, and the model does not account for the interactions between permafrost and vegetation (Stuenzi, Boike, Cable, et al., 2021; Stuenzi, Boike, Gädeke, et al., 2021), subsidence processes following excess ice melting (Nitzbon et al., 2019), and sub-grid lateral fluxes (Nitzbon et al., 2021), which are known to affect permafrost thaw trajectories in complex landscapes. Further detailed descriptions of model limitation and uncertainty can be found in Langer et al. (2024). Moreover, for future permafrost simulations, we employed two ESMs (AWI-CM-

1-1-MR and MPI-ESM1-2-HR) to drive our CryoGridLite model. These ESMs have demonstrated their capability in accurately reproducing mean annual and seasonal surface air temperatures over recent decades (R. Chen, Li, et al., 2022). However, significant discrepancies were observed in their representation of precipitation changes (R. Chen, Duan, et al., 2022), introducing a notable degree of uncertainty into our permafrost projections. This is due to the permafrost's thermal state being highly sensitive not only to air temperature but also to precipitation; increased rainfall can significantly mitigate permafrost degradation on the Tibetan Plateau (TP) (G. Zhang et al., 2021; Hamm et al., 2023). Therefore, to enhance our understanding of permafrost evolution on the TP, it is imperative to conduct additional simulations using a variety of ESMs

Regarding the NDVI changes predicted by our model, we acknowledge a certain degree of uncertainty inherent in the outputs of our machine learning algorithms. Primarily, these models are challenged by their reliance on data-driven approaches, which may lack a solid physical basis, transparency, interpretability, and a heightened sensitivity to outliers, potentially leading to instability or inaccurate predictions (G. Zhang et al., 2022; C. Shen et al., 2023). Therefore, in our study, although we implemented several strategies to overcome the inherent shortcomings of machine learning algorithms, to make our results more robust, we extrapolated the predicted NDVI only to 2050. In addition, while NDVI data are extensively utilized for assessing the vegetative state of the TP (Teng et al., 2021; T. Wang et al., 2022; Yang et al., 2023), the reliability of this satellite-derived data is considerably impacted by factors such as sensor characteristics, atmospheric interference, and soil background effects (Sha et al., 2020). Therefore, it is crucial for future research to incorporate a broad spectrum of vegetation indices (e.g. LAI, EVI, NPP, soil-adjusted vegetation index) and apply more data to feed machine learning model to reduce these errors and enable a more comprehensive analysis of vegetative dynamics on the TP, particularly against the backdrop of ongoing climatic warming. Moreover, we would like to point out that NDVI_{GS} predictions in this study were based on MODIS satellite imagery. Owing to the data dependency of the machine learning model, the use of alternative NDVI products as response variables might yield divergent results. This is particularly evident in the study of Yang et al. (2023), which employed multi-source data to investigate vegetation changes on the TP since 2000, revealing significant spatiotemporal discrepancies among MODIS data, GIMMS NDVI, and SPOT-VEG NDVI (e.g. SPOT-VEG NDVI ($p < 0.001$) and MODIS NDVI ($p < 0.05$) indicated a significant increasing trend, while GIMMS NDVI data ($p < 0.534$) did not show a significant increasing trend in NDVI on the TP). Meanwhile, the selection of explanatory variables significantly influences the determination of the quantitative contributions of predominant factors. Additionally, vegetation browning events induced by abrupt permafrost thaw (Heijmans et al., 2022) and vegetation greening occurring in thermokarst-drained lake basins (Y. Chen et al., 2023) are not considered in our study, which play an important role in controlling vegetation growth. Despite several shortcomings in our permafrost model and machine learning algorithms, our results attempt to provide a framework for exploring future vegetation changes in cold regions and identified limitations give opportunities for future improvements in our modeling approach.

5 Conclusions

In this study, we combined a numerical permafrost model (CryoGridLite) with machine-learning algorithms to analyze the vegetation conditions in the permafrost areas over the TP under various climate scenarios. Our model simulations, when compared with observational data, efficiently captured the spatiotemporal patterns of permafrost across the TP during the baseline period (2000–2018), and the machine learning algorithm effectively reproduced the interannual NDVI_{GS} for the testing period (2015–2018). Forced by different climate conditions, our CryoGridLite model projected a continual decline in the permafrost areas on the TP in response to future climate warming. Under the SSP1-

2.6 scenario, mean annual ground temperature and active layer thickness appeared stable on average, but with regionally different responses i.e mean annual ground temperature and active layer thickness tended to increase in the Three River Source region and Qinghai-Tibet Engineering Corridor and decrease in the northwest of TP. However, under the SSP5-8.5 scenarios, there was a notable increase in both mean annual ground temperature and active layer thickness. Remote sensing imagery from MODIS suggested that approximately 30% of the permafrost areas on the TP showed an increasing trend in $NDVI_{GS}$ over the baseline period. The results of machine learning indicated that under the low emission scenario (SSP1–2.6), no significant change in $NDVI_{GS}$ was expected for >85% permafrost areas in the future. In contrast, under the high emission scenario, an increasing trend in $NDVI_{GS}$ in the future in about 7.31–29.10% of the permafrost areas, with less than 2% of the area experiencing a significantly decreased NDVI. Analysis of the contributory factors revealed that climatic factors during the growing season were the primary influence on NDVI alterations within the permafrost areas for the baseline period (2000–2018). For the future periods (2019–2050), it was found that the surface air temperature and liquid water content at the root zone during the growing season were anticipated to play a crucial, undeniable role in the $NDVI_{GS}$ changes within the permafrost areas. Although our approach has not yet fully accounted for the processes affecting the thermal state of permafrost and vegetation growth on the TP, the coupling of process-based and data-driven models provides a potential and meaningful pathway for detecting future vegetation evolution on the plateau. Our future research will aim to address the limitations of our methodology and deliver more accurate predictions, thereby enhancing our understanding of the carbon budget of the TP.

Open Research Section

The China Meteorological Forcing Dataset is available at `https://data.tpdc.ac.cn/zh-hans/data/8028b944-daaa-4511-8769-965612652c49`. The AWI-CM-1-1-MR and MPI-ESM1-2-HR datasets are available at `https://esgf-data.dkrz.de/search/cmip6-dkrz/`. The Vegetation types data is available at `https://www.resdc.cn/data.aspx?DATAID=122`. The shapefile of the boundary of the Tibetan Plateau is available at `https://www.geodoi.ac.cn/WebCn/doi.aspx?Id=135`. The shape file of lakes on the Tibetan Plateau is available at `https://www.tpdc.ac.cn/zh-hans/data/da4ffc9a-91fb-4ae9-8da5-c57aa92c8d2b`. The shape file of the glacier on the Tibetan Plateau is available at `https://www.tpdc.ac.cn/zh-hans/data/f92a4346-a33f-497d-9470-2b357ccb4246`. The Global high-resolution dataset of soil hydraulic and thermal parameters dataset is available at `http://globalchange.bnu.edu.cn/research/soil5.jsp`. The Global watertable depth dataset is available at `https://glowasis.deltares.nl/thredds/catalog/opendap/opendap/Equilibrium_Water_Table/catalog.html`. The Terrestrial heat flow dataset is available at `https://doi.org/10.1029/2019GC008389`. The ERA5-Land dataset is available at `https://cds.climate.copernicus.eu/cdsapp#!/dataset/reanalysis-era5-land?tab=overview`. The MODIS NDVI (MOD13A2, Version 6.1) is available from Google Earth Engine at `https://developers.google.com/earth-engine/datasets/catalog/MODIS_061_MOD13A2`. The CryoGridLite model code, machine-learning algorithms, and ridge regression method used for the simulations and analysis in this work are archived on Zenodo (`https://doi.org/10.5281/zenodo.10928146`).

Acknowledgments

Rui Chen was supported by the China Scholarship Council (No. 201904910442). Simone M. Stuenzi was supported by the Bundesministerium für Bildung und Forschung (grant no. 03F0931A).

References

Baral, P., Allen, S., Steiner, J. F., Gurung, T. R., & McDowell, G. (2023). Climate change impacts and adaptation to permafrost change in high mountain asia: a comprehensive review. *Environmental Research Letters*, *18*, 093005. doi: https://doi.org/10.1088/1748-9326/acf1b4

Cao, B., Gruber, S., Zhang, T., Li, L., Peng, X., Wang, K., ... Guo, H. (2017). Spatial variability of active layer thickness detected by ground-penetrating radar in the qilian mountains, western china. *Journal of Geophysical Research: Earth Surface*, *122*, 574–591. doi: https://doi.org/10.1002/2016JF004018

Cao, R., Ling, X., Liu, L., Wang, W., Li, L., & Shen, M. (2023). Remotely sensed vegetation green-up onset date on the tibetan plateau: Simulations and future predictions. *IEEE Journal of Selected Topics in Applied Earth Observations and Remote Sensing*, *16*, 8125–8134. doi: https://doi.org/10.1109/JSTARS.2023.3310617

Cao, Z., Nan, Z., Hu, J., Chen, Y., & Zhang, Y. (2023). A new 2010 permafrost distribution map over the qinghai–tibet plateau based on subregion survey maps: a benchmark for regional permafrost modeling. *Earth System Science Data*, *15*, 3905–3930. doi: https://doi.org/10.5194/essd-15-3905-2023

Chang, X., Jin, H., Zhang, Y., He, R., Luo, D., Wang, Y., ... Zhang, Q. (2015). Thermal impacts of boreal forest vegetation on active layer and permafrost soils in northern da xing'anling (hinggan) mountains, northeast china. *Arctic, Antarctic, and Alpine Research*, *47*, 267–279. doi: https://doi.org/10.1657/AAAR00C-14-016

Chen, C., Peng, X., Frauenfeld, O. W., Chu, X., Chen, G., Huang, Y., ... Tian, W. (2024). Simulations and prediction of historical and future maximum freeze depth in the northern hemisphere. *Journal of Geophysical Research: Atmospheres*, *129*, e2023JD039420. doi: https://doi.org/10.1029/2023JD039420

Chen, F., Zhang, X., & Chen, Z. (2023). High-temperature exposure and land transactions in china. *Earth's Future*, *11*, e2022EF003008. doi: https://doi.org/10.1029/2022EF003008

Chen, H., Nan, Z., Zhao, L., Ding, Y., Chen, J., & Pang, Q. (2015). Noah modelling of the permafrost distribution and characteristics in the west kunlun area, qinghai-tibet plateau, china. *Permafrost and Periglacial Processes*, *26*, 160–174. doi: https://doi.org/10.1002/ppp.1841

Chen, J., Zhao, L., Sheng, Y., Li, J., Wu, X., Du, E., ... Pang, Q. (2016). Some characteristics of permafrost and its distribution in the gaize area on the qinghai-tibet plateau, china. *Arctic, Antarctic, and Alpine Research*, *48*, 395–409. doi: https://doi.org/10.1657/AAAR0014-023

Chen, R., Duan, K., Shang, W., Shi, P., Meng, Y., & Zhang, Z. (2022). Increase in seasonal precipitation over the tibetan plateau in the 21st century projected using cmip6 models. *Atmospheric Research*, *277*, 106306. doi: https://doi.org/10.1016/j.atmosres.2022.106306

Chen, R., Li, H., Wang, X., Gou, X., Yang, M., & Wan, G. (2022). Surface air temperature changes over the tibetan plateau: Historical evaluation and future projection based on cmip6 models. *Geoscience Frontiers*, *13*, 101452. doi: https://doi.org/10.1016/j.gsf.2022.101452

Chen, R., von Deimling, T. S., Boike, J., Wu, Q., & Langer, M. (2023). Simulating the thermal regime of a railway embankment structure on the tibetan plateau under climate change. *Cold Regions Science and Technology*, *212*, 103881. doi: https://doi.org/10.1016/j.coldregions.2023.103881

Chen, T., & Guestrin, C. (2016). Xgboost: A scalable tree boosting system. In *Proceedings of the 22nd acm sigkdd international conference on knowledge discovery and data mining* (p. 785–794). New York, NY, USA: Association for Computing Machinery. Retrieved from `https://doi.org/10.1145/2939672.2939785` doi: 10.1145/2939672.2939785

Chen, Y., Cheng, X., Liu, A., Chen, Q., & Wang, C. (2023). Tracking lake drainage events and drained lake basin vegetation dynamics across the arctic. *Nature Communications*, *14*, 7359. doi: https://doi.org/10.1038/s41467-023-43207-0

Cuo, L., Zhang, Y., & Li, N. (2022). Historical and future vegetation changes in the degraded frozen soil and the entire tibetan plateau and climate drivers. *Journal of Geophysical Research: Biogeosciences*, *127*, e2022JG006987. doi: https://doi.org/10.1029/2022JG006987

Dai, L., Che, T., Xie, H., & Wu, X. (2018). Estimation of snow depth over the qinghai-tibetan plateau based on amsr-e and modis data. *Remote Sensing*, *10*, 1989. doi: https://doi.org/10.3390/rs10121989

Dai, Y., Shangguan, W., Duan, Q., Liu, B., Fu, S., & Niu, G. (2013). Development of a china dataset of soil hydraulic parameters using pedotransfer functions for land surface modeling. *Journal of Hydrometeorology*, *14*, 869–887.

Dai, Y., Wei, N., Yuan, H., Zhang, S., Shangguan, W., Liu, S., … Xin, Y. (2019). Evaluation of soil thermal conductivity schemes for use in land surface modeling. *Journal of Advances in Modeling Earth Systems*, *11*, 3454–3473. doi: https://doi.org/10.1029/2019MS001723

Dai, Y., Xin, Q., Wei, N., Zhang, Y., Shangguan, W., Yuan, H., … Lu, X. (2019). A global high-resolution data set of soil hydraulic and thermal properties for land surface modeling. *Journal of Advances in Modeling Earth Systems*, *11*, 2996–3023. doi: https://doi.org/10.1029/2019MS001784

de Vrese, P., Georgievski, G., Rouco, J. F. G., Notz, D., Stacke, T., Steinert, N. J., … Brovkin, V. (2023). Representation of soil hydrology in permafrost regions may explain large part of inter-model spread in simulated arctic and subarctic climate. *The Cryosphere*, *17*, 2095–2118. doi: https://doi.org/10.5194/tc-17-2095-2023

Didan, K. (2015). *Mod13a2 modis/terra vegetation indices 16-day l3 global 1km sin grid v006.* doi: https://doi.org/10.5067/MODIS/MOD13A2.061

Ding, J., Chen, L., Ji, C., Hugelius, G., Li, Y., Liu, L., … Yang, Y. (2017). Decadal soil carbon accumulation across tibetan permafrost regions. *Nature Geoscience*, *10*, 420–424. doi: https://doi.org/10.1038/ngeo2945

Ehlers, T. A., Chen, D., Appel, E., Bolch, T., Chen, F., Diekmann, B., … Zhu, L. (2022). Past, present, and future geo-biosphere interactions on the tibetan plateau and implications for permafrost. *Earth-Science Reviews*, *234*, 104197. doi: https://doi.org/10.1016/j.earscirev.2022.104197

Fan, Y., Li, H., & Miguez-Macho, G. (2013). Global patterns of groundwatertable depth. *Science*, *339*, 940–943. doi: https://doi.org/10.1126/science.1229881

Gagnon, M., Domine, F., & Boudreau, S. (2019). The carbon sink due to shrub growth on arctic tundra: a case study in a carbon-poor soil in eastern canada. *Environmental Research Communications*, *1*, 091001. doi: https://doi.org/10.1088/2515-7620/ab3cdd

Gao, J., Jiao, K., Wu, S., Ma, D., Zhao, D., Yin, Y., & Dai, E. (2017). Past and future effects of climate change on spatially heterogeneous vegetation activity in china. *Earth's Future*, *5*, 679–692. doi: https://doi.org/10.1002/2017EF000573

Gao, Q., Guo, Y., Xu, H., Ganjurjav, H., Li, Y., Wan, Y., … Liu, S. (2016). Climate change and its impacts on vegetation distribution and net primary productivity of the alpine ecosystem in the qinghai-tibetan plateau. *Science of The Total Environment*, *554–555*, 34–41. doi: https://doi.org/10.1016/j.scitotenv.2016.02.131

Gao, T., Zhang, Y., Kang, S., Abbott, B. W., Wang, X., Zhang, T., … Gustafsson, Ö. (2021). Accelerating permafrost collapse on the eastern tibetan plateau. *Environmental Research Letters*, *16*, 054023. doi: https://doi.org/10.1088/1748-9326/abf7f0

Gao, Y., Luo, D., Chen, F., Lei, W., & Jin, H. (2023). Characteristics of the thermal regime and freeze-thaw cycles on the ground surface in permafrost regions in the headwater area of the yellow river. *Acta Geographica Sinica*, *78*, 604–619. doi: https://geog.com.cn/EN/10.11821/dlxb202303007

Grünberg, I., Wilcox, E. J., Zwieback, S., Marsh, P., & Boike, J. (2020). Linking tundra vegetation, snow, soil temperature, and permafrost. *Biogeosciences*, *17*, 4261–4279. doi: https://doi.org/10.5194/bg-17-4261-2020

Guo, D., & Wang, H. (2013). Simulation of permafrost and seasonally frozen ground conditions on the tibetan plateau, 1981–2010. *Journal of Geophysical Research: Atmospheres*, *118*, 5216–5230. doi: https://doi.org/10.1002/jgrd.50457

Guo, J., Zhai, L., Sang, H., Cheng, S., & Li, H. (2023). Effects of hydrothermal factors and human activities on the vegetation coverage of the qinghai-tibet plateau. *Scientific Reports*, *13*, 12488. doi: https://doi.org/10.1038/s41598-023-39761-8

Guo, W., Liu, S., Xu, J., Wu, L., Shangguan, D., Yao, X., ... Jiang, Z. (2015). The second chinese glacier inventory: data, methods and results. *Journal of Glaciology*, *61*, 357–372. doi: https://doi.org/10.3189/2015JoG14J209

Gupta, H. V., Kling, H., K, K., Yilmaz, & Martinez, G. F. (2009). Decomposition of the mean squared error and nse performance criteria: Implications for improving hydrological modelling. *Journal of Hydrology*, *377*, 80–91. doi: https://doi.org/10.1016/j.jhydrol.2009.08.003

Hamm, A., Magnússon, R. Í., Khattak, A. J., & Frampton, A. (2023). Continentality determines warming or cooling impact of heavy rainfall events on permafrost. *Nature Communications*, *14*, 3578. doi: https://doi.org/10.1038/s41467-023-39325-4

Hawinkel, P., Thiery, W., Lhermitte, S., Swinnen, E., Verbist, B., Orshoven, J. V., & Muys, B. (2016). Vegetation response to precipitation variability in east africa controlled by biogeographical factors. *Journal of Geophysical Research: Biogeosciences*, *121*, 2422–2444. doi: https://doi.org/10.1002/2016JG003436

He, J., Yang, K., Tang, W., Lu, H., Qin, J., Chen, Y., & Li, X. (2020). The first high-resolution meteorological forcing dataset for land process studies over china. *Scientific Data*, *7*, 25. doi: https://doi.org/10.1038/s41597-020-0369-y

Heijmans, M. M. P. D., Magnússon, R. Í., Lara, M. J., Frost, G. V., Myers-Smith, I. H., van Huissteden, J., ... Limpens, J. (2022). Tundra vegetation change and impacts on permafrost. *Nature Reviews Earth & Environment*, *3*, 68–84. doi: https://doi.org/10.1038/s43017-021-00233-0

Higgins, S. I., Conradi, T., & Muhoko, E. (2023). Shifts in vegetation activity of terrestrial ecosystems attributable to climate trends. *Nature Geoscience*, *16*, 147–153. doi: https://doi.org/10.1038/s41561-022-01114-x

Jin, X., Jin, H., Iwahana, G., Marchenko, S. S., Luo, D., Li, X., & Liang, S. (2021). Impacts of climate-induced permafrost degradation on vegetation: A review. *Advances in Climate Change Research*, *12*, 29–47. doi: https://doi.org/10.1016/j.accre.2020.07.002

Jin, Z., You, Q., Zuo, Z., Li, M., Sun, G., Pepin, N., & Wang, L. (2023). Weakening amplification of grassland greening to transpiration fraction of evapotranspiration over the tibetan plateau during 2001-2020. *Agricultural and Forest Meteorology*, *341*, 109661. doi: https://doi.org/10.1016/j.agrformet.2023.109661

Ke, G., Meng, Q., Finley, T., Wang, T., Chen, W., Ma, W., ... Liu, T. (2017). Lightgbm: A highly efficient gradient boosting decision tree. In *Proceedings of the 31st international conference on neural information processing systems* (pp. 3149–3157). Red Hook, NY, USA: Curran Associates Inc.

Kondylatos, S., Prapas, I., Ronco, M., Papoutsis, I., Camps-Valls, G., Piles, M., ... Carvalhais, N. (2022). Wildfire danger prediction and understanding with deep learning. *Geophysical Research Letters*, e2022GL099368. doi: https://doi.org/10.1029/2022GL099368

Kong, Z., Liang, H., Deng, M., Han, F., Yan, J., Deng, X., ... Wang, W. (2023).

Past and projected future patterns of fractional vegetation coverage in china. *Science of The Total Environment*, *902*, 166133. doi: https://doi.org/10.1016/j.scitotenv.2023.166133

Langer, M., Nitzbon, J., Groenke, B., Assmann, L.-M., von Deimling, T. S., Stuenzi, S. M., & Westermann, S. (2024). The evolution of arctic permafrost over the last 3 centuries from ensemble simulations with the cryogridlite permafrost model. *The Cryosphere*, *18*, 363–385. doi: https://doi.org/10.5194/tc-18-363-2024

Langer, M., von Deimling, T. S., Westermann, S., Rolph, R., Ralph, R., Antonova, S., ... Grosse, G. (2023). Thawing permafrost poses environmental threat to thousands of sites with legacy industrial contamination. *Nature Communications*, *14*, 1721. doi: https://doi.org/10.1038/s41467-023-37276-4

Lawrence, D. M., & Swenson, S. C. (2011). Permafrost response to increasing arctic shrub abundance depends on the relative influence of shrubs on local soil cooling versus large-scale climate warming. *Environmental Research Letters*, *6*, 045504. doi: https://doi.org/10.1088/1748-9326/6/4/045504

Li, H., Pan, X., Washakh, R. M. A., & Nie, X. (2024). A new method of diagnosing the historical and projected changes in permafrost on the tibetan plateau. *Earth's Future*, *12*, e2023EF003897. doi: https://doi.org/10.1029/2023EF003897

Li, J., Wu, C., nuelas, J. P., Ran, Y., & Zhang, Y. (2023). The start of frozen dates over northern permafrost regions with the changing climate. *Global Change Biology*, *29*, 4556–4568. doi: https://doi.org/10.1111/gcb.16752

Li, X., Zhang, K., & Li, X. (2022). Responses of vegetation growth to climate change over the tibetan plateau from 1982 to 2018. *Environmental Research Communications*, *4*, 045007.

Liu, L., Zhuang, Q., Zhao, D., Zheng, D., Kou, D., & Yang, Y. (2022). Permafrost degradation diminishes terrestrial ecosystem carbon sequestration capacity on the qinghai-tibetan plateau. *Global Biogeochemical Cycles*, *36*, e2021GB007068. doi: https://doi.org/10.1029/2021GB007068

Liu, W., Wang, G., Yu, M., Chen, H., & Jiang, Y. (2020). Multimodel future projections of the regional vegetation-climate system over east asia: Comparison between two ensemble approaches. *Journal of Geophysical Research: Atmospheres*, *125*, e2019JD031967. doi: https://doi.org/10.1029/2019JD031967

Loranty, M. M., Abbott, B. W., Blok, D., Douglas, T. A., Epstein, H. E., Forbes, B. C., ... Walker, D. A. (2018). Reviews and syntheses: Changing ecosystem influences on soil thermal regimes in northern high-latitude permafrost regions. *Biogeosciences*, *15*, 5287–5313. doi: https://doi.org/10.5194/bg-15-5287-2018

Lu, H., Zheng, D., Yang, K., & Yang, F. (2020). Last-decade progress in understanding and modeling the land surface processes on the tibetan plateau. *Hydrology and Earth System Sciences*, *24*, 5745–5758. doi: https://doi.org/10.5194/hess-24-5745-2020

Lucazeau, F. (2019). Analysis and mapping of an updated terrestrial heat flow data set. *Geochemistry, Geophysics, Geosystems*, *20*, 4001–4024. doi: https://doi.org/10.1029/2019GC008389

Luo, D., Jin, H., Jin, X., He, R., Li, X., Muskett, R. R., ... Romanovsky, V. E. (2018). Elevation-dependent thermal regime and dynamics of frozen ground in the bayan har mountains, northeastern qinghai-tibet plateau, southwest china. *Permafrost and Periglacial Processes*, *29*, 257–270. doi: https://doi.org/10.1002/ppp.1988

Mahowald, N., Lo, F., Zheng, Y., Harrison, L., Funk, C., Lombardozzi, D., & Goodale, C. (2016). Projections of leaf area index in earth system models. *Earth System Dynamics*, *7*, 211–229. doi: https://doi.org/10.5194/esd-7-211-2016

Mauclet, E., Agnan, Y., Hirst, C., Monhonval, A., Pereira, B., Vandeuren, A., ...

Opfergelt, S. (2022). Changing sub-arctic tundra vegetation upon permafrost degradation: impact on foliar mineral element cycling. *Biogeosciences*, *19*, 2333–2351. doi: https://doi.org/10.5194/bg-19-2333-2022

Mekonnen, Z. A., Riley, W. J., & Grant, R. F. (2018). Accelerated nutrient cycling and increased light competition will lead to 21st century shrub expansion in north american arctic tundra. *Journal of Geophysical Research: Biogeosciences*, *123*, 1683–1701. doi: https://doi.org/10.1029/2017JG004319

Mu, C., Abbott, B. W., Norris, A. J., Mu, M., Fan, C., Chen, X., ... Wu, X. (2020). The status and stability of permafrost carbon on the tibetan plateau. *Earth-Science Reviews*, *211*, 103433. doi: https://doi.org/10.1016/j.earscirev.2020.103433

Mu, C., Abbott, B. W., Zhao, Q., Su, H., Wang, S., Wu, Q., ... Wu, X. (2017). Permafrost collapse shifts alpine tundra to a carbon source but reduces n_2o and ch_4 release on the northern qinghai-tibetan plateau. *Geophysical Research Letters*, *44*, 8945–8952. doi: https://doi.org/10.1002/2017GL074338

Mu, C., & Peng, X. (2022). *A synthesis dataset of frozen ground and soil carbon in heihe river basin qilian mountainous (2011–2020).* National Tibetan Plateau Data Center. doi: https://doi.org/10.11888/Cryos.tpdc.272840

Müller, W. A., Jungclaus, J. H., Mauritsen, T., Baehr, J., Bittner, M., Budich, R., ... Marotzke, J. (2018). A higher-resolution version of the max planck institute earth system model (mpi-esm1.2-hr). *Journal of Advances in Modeling Earth Systems*, *10*, 1383–1413. doi: https://doi.org/10.1029/2017MS001217

Muñoz-Sabater, J., Dutra, E., Agustí-Panareda, A., Albergel, C., Arduini, G., Balsamo, G., ... Thépaut, J.-N. (2021). Era5-land: a state-of-the-art global reanalysis dataset for land applications. *Earth System Science Data*, *13*, 4349–4383. doi: https://doi.org/10.5194/essd-13-4349-2021

Myers-Smith, I. H., Kerby, J. T., Phoenix, G. K., Bjerke, J. W., Epstein, H. E., Assmann, J. J., ... Wipf, S. (2020). Complexity revealed in the greening of the arctic. *Nature Climate Change*, *10*, 106–117. doi: https://doi.org/10.1038/s41558-019-0688-1

Ni, J., Wu, T., Zhu, X., Hu, G., Zou, D., Wu, X., ... Yang, C. (2021). Simulation of the present and future projection of permafrost on the qinghai-tibet plateau with statistical and machine learning models. *Journal of Geophysical Research: Atmospheres*, *126*, e2020JD033402. doi: https://doi.org/10.1029/2020JD033402

Nitzbon, J., Krinner, G., von Deimling, T. S., Werner, M., & Langer, M. (2023). First quantification of the permafrost heat sink in the earth's climate system. *Geophysical Research Letters*, *50*, e2022GL102053. doi: https://doi.org/10.1029/2022GL102053

Nitzbon, J., Langer, M., Martin, L. C. P., Westermann, S., von Deimling, T. S., & Boike, J. (2021). Effects of multi-scale heterogeneity on the simulated evolution of ice-rich permafrost lowlands under a warming climate. *The Cryosphere*, *15*, 1399–1422. doi: https://doi.org/10.5194/tc-15-1399-2021

Nitzbon, J., Langer, M., Westermann, S., Martin, L., Aas, K. S., & Boike, J. (2019). Pathways of ice-wedge degradation in polygonal tundra under different hydrological conditions. *The Cryosphere*, *13*, 1089–1123. doi: https://doi.org/10.5194/tc-13-1089-2019

Nitze, I., Grosse, G., Jones, B. M., Romanovsky, V. E., & Boike, J. (2018). Remote sensing quantifies widespread abundance of permafrost region disturbances across the arctic and subarctic. *Nature Communications*, *9*, 5423. doi: https://doi.org/10.1038/s41467-018-07663-3

Obu, J., Westermann, S., Bartsch, A., Berdnikov, N., Christiansen, H. H., Dashtseren, A., ... Zou, D. (2019). Northern hemisphere permafrost map based on ttop modelling for 2000–2016 at 1km^2 scale. *Earth-Science Reviews*, *193*, 299–316. doi: https://doi.org/10.1016/j.earscirev.2019.04.023

Orsolini, Y., Wegmann, M., Dutra, E., Liu, B., Balsamo, G., Yang, K., … Arduini, G. (2019). Evaluation of snow depth and snow cover over the tibetan plateau in global reanalyses using in situ and satellite remote sensing observations. *The Cryosphere*, *13*, 2221–2239. doi: https://doi.org/10.5194/tc-13-2221-2019

Pang, G., Chen, D., Wang, X., & Lai, H. (2022). Spatiotemporal variations of land surface albedo and associated influencing factors on the tibetan plateau. *Science of The Total Environment*, *804*, 150100. doi: https://doi.org/10.1016/j.scitotenv.2021.150100

Pang, Y., Zou, K., Guo, X., Chen, Y., Zhao, J., Zhou, F., … Yang, G. (2022). Geothermal regime and implications for basin resource exploration in the qaidam basin, northern tibetan plateau. *Journal of Asian Earth Sciences*, *239*, 105400. doi: https://doi.org/10.1016/j.jseaes.2022.105400

Pearson, R. G., Phillips, S. J., Loranty, M. M., Beck, P. S. A., Damoulas, T., Knight, S. J., & Goetz, S. J. (2013). Shifts in arctic vegetation and associated feedbacks under climate change. *Nature Climate Change*, *3*, 673–677. doi: https://doi.org/10.1038/nclimate1858

Piao, S., Wang, X., Park, T., Chen, C., Lian, X., He, Y., … Myneni, R. B. (2020). Characteristics, drivers and feedbacks of global greening. *Nature Reviews Earth & Environment*, *1*, 14–27. doi: https://doi.org/10.1038/s43017-019-0001-x

Prager, C. M., Boelman, N. T., Eitel, J. U. H., Gersony, J. T., Greaves, H. E., Heskel, M. A., … Griffin, K. L. (2020). A mechanism of expansion: arctic deciduous shrubs capitalize on warming-induced nutrient availability. *Oecologia*, *192*, 671–685. doi: https://doi.org/10.1007/s00442-019-04586-8

Qin, Y., Wu, T., Zhao, L., Wu, X., Li, R., Xie, C., … Hao, J. (2017). Numerical modeling of the active layer thickness and permafrost thermal state across qinghai-tibetan plateau. *Journal of Geophysical Research: Atmospheres*, *122*, 11604–11620. doi: https://doi.org/10.1002/2017JD026858

Ran, Y., Cheng, G., Dong, Y., Hjort, J., Lovecraft, A. L., Kang, S., … Li, X. (2022). Permafrost degradation increases risk and large future costs of infrastructure on the third pole. *Communications Earth & Environment*, *3*, 238. doi: https://doi.org/10.1038/s43247-022-00568-6

Ran, Y., Li, X., & Cheng, G. (2018). Climate warming over the past half century has led to thermal degradation of permafrost on the qinghai–tibet plateau. *The Cryosphere*, *12*, 595–608. doi: https://doi.org/10.5194/tc-12-595-2018

Ran, Y., Li, X., Cheng, G., Che, J., Aalto, J., Karjalainen, O., … Chang, X. (2022). New high-resolution estimates of the permafrost thermal state and hydrothermal conditions over the northern hemisphere. *Earth System Science Data*, *14*, 865–884. doi: https://doi.org/10.5194/essd-14-865-2022

Ran, Y., Li, X., Cheng, G., Nan, Z., Che, J., Sheng, Y., … Wu, X. (2021). Mapping the permafrost stability on the tibetan plateau for 2005–2015. *Science China Earth Sciences*, *64*, 62–79. doi: https://doi.org/10.1007/s11430-020-9685-3

Semmler, T., Danilov, S., Gierz, P., Goessling, H. F., Hegewald, J., Hinrichs, C., … Jung, T. (2020). Simulations for cmip6 with the awi climate model awi-cm-1-1. *Journal of Advances in Modeling Earth Systems*, *12*, e2019MS002009. doi: https://doi.org/10.1029/2019MS002009

Sha, H., Lina, T., P, H. J., Yang, W., & Guofan, S. (2020). A commentary review on the use of normalized difference vegetation index (ndvi) in the era of popular remote sensing. *Journal of Forestry Research*, *32*, 1–6. doi: https://doi.org/10.1007/s11676-020-01155-1

Shen, C., Appling, A. P., Gentine, P., Bandai, T., Gupta, H., Tartakovsky, A., … Lawson, K. (2023). Differentiable modelling to unify machine learning and physical models for geosciences. *Nature Reviews Earth & Environment*, *4*, 552–567. doi: https://doi.org/10.1038/s43017-023-00450-9

Shen, M., Wang, S., Jiang, N., Sun, J., Cao, R., Ling, X., … Fu, B. (2022). Plant phenology changes and drivers on the qinghai–tibetan plateau. *Nature Re-*

views Earth & Environment, *3*, 633–651. doi: https://doi.org/10.1038/s43017-022-00317-5

Shi, S., Wang, P., Zhan, X., Han, J., Guo, M., & Wang, F. (2023). Warming and increasing precipitation induced greening on the northern qinghai-tibet plateau. *Catena*, *233*, 107483. doi: https://doi.org/10.1016/j.catena.2023.107483

Smith, S. L., O'Neill, H. B., Isaksen, K., Noetzli, J., & Romanovsky, V. E. (2022). The changing thermal state of permafrost. *Nature Reviews Earth & Environment*, *3*, 10–23. doi: https://doi.org/10.1038/s43017-021-00240-1

Song, L., Wang, L., Zhou, J., Luo, D., & Li, X. (2022). Divergent runoff impacts of permafrost and seasonally frozen ground at a large river basin of tibetan plateau during 1960–2019. *Environmental Research Letters*, *17*, 124038. doi: https://doi.org/10.1088/1748-9326/aca4eb

Stuenzi, S. M., Boike, J., Cable, W., Herzschuh, U., Kruse, S., Pestryakova, L. A., . . . Langer, M. (2021). Variability of the surface energy balance in permafrost-underlain boreal forest. *Biogeosciences*. doi: https://doi.org/10.5194/bg-18-343-2021

Stuenzi, S. M., Boike, J., Gädeke, A., Herzschuh, U., Kruse, S., Pestryakova, L. A., . . . Langer, M. (2021). Sensitivity of ecosystem-protected permafrost under changing boreal forest structures. *Environmental Research Letters*, *16*, 085045. doi: https://doi.org/10.1088/1748-9326/ac153d

Teng, H., Luo, Z., Chang, J., Shi, Z., Chen, S., Zhou, Y., . . . Tian, H. (2021). Climate change-induced greening on the tibetan plateau modulated by mountainous characteristics. *Environmental Research Letters*, *16*, 064064. doi: https://doi.org/10.1088/1748-9326/abfeeb

Ukkonen, P., & Mäkelä, A. (2019). Evaluation of machine learning classifiers for predicting deep convection. *Journal of Advances in Modeling Earth Systems*, *11*, 1784–1802. doi: https://doi.org/10.1029/2018MS001561

van der Kolk, H.-J., Heijmans, M. M. P. D., van Huissteden, J., Pullens, J. W. M., & Berendse, F. (2016). Potential arctic tundra vegetation shifts in response to changing temperature, precipitation and permafrost thaw. *Biogeosciences*, *13*, 6229–6245. doi: https://doi.org/10.5194/bg-13-6229-2016

Veigel, N., Kreibich, H., & Cominola, A. (2023). Interpretable machine learning reveals potential to overcome reactive flood adaptation in the continental us. *Earth's Future*, *11*, e2023EF003571. doi: https://doi.org/10.1029/2023EF003571

Wang, J., & Liu, D. (2022). Vegetation green-up date is more sensitive to permafrost degradation than climate change in spring across the northern permafrost region. *Global Change Biology*, *28*, 1569–1582. doi: https://doi.org/10.1111/gcb.16011

Wang, T., Yang, D., Yang, Y., Piao, S., Li, X., Cheng, G., & Fu, B. (2020). Permafrost thawing puts the frozen carbon at risk over the tibetan plateau. *Science Adcances*, *6*, eaaz3513. doi: https://doi.org/10.1126/sciadv.aaz3513

Wang, T., Yang, D., Yang, Y., Zheng, G., Jin, H., Li, X., . . . Cheng, G. (2023). Pervasive permafrost thaw exacerbates future risk of water shortage across the tibetan plateau. *Earth's Future*, *11*, e2022EF003463. doi: https://doi.org/10.1029/2022EF003463

Wang, T., Yang, D., Zheng, G., & Shi, R. (2022). Possible negative effects of earlier thaw onset and longer thaw duration on vegetation greenness over the tibetan plateau. *Agricultural and Forest Meteorology*, *326*, 109192. doi: https://doi.org/10.1016/j.agrformet.2022.109192

Wang, W., Rinke, A., Moore, J. C., Cui, X., Ji, D., Li, Q., . . . Decharme, B. (2016). Diagnostic and model dependent uncertainty of simulated tibetan permafrost area. *The Cryosphere*, *10*, 287–306. doi: https://doi.org/10.5194/tc-10-287-2016

Wang, W., Yang, K., Zhao, L., Zheng, Z., Lu, H., Mamtimin, A., . . . Moore, J. C.

(2020). Characterizing surface albedo of shallow fresh snow and its importance for snow ablation on the interior of the tibetan plateau. *Journal of Hydrometeorology*, *21*, 815–827. doi: https://doi.org/10.1175/JHM-D-19-0193.1

Wang, X., Ran, Y., Pang, G., Chen, D., Su, B., Chen, R., … Luo, D. (2022). Contrasting characteristics, changes, and linkages of permafrost between the arctic and the third pole. *Earth-Science Reviews*, *230*, 104042. doi: https://doi.org/10.1016/j.earscirev.2022.104042

Wang, Y., Xiao, J., Ma, Y., Ding, J., Chen, X., Ding, Z., & Luo, Y. (2023). Persistent and enhanced carbon sequestration capacity of alpine grasslands on earth's third pole. *Science Advances*, *9*, eade6875. doi: https://doi.org/10.1126/sciadv.ade6875

Wang, Z., Wang, Q., Zhao, L., Wu, X., Yue, G., Zou, D., … Zhang, Y. Z. . L. (2016). Mapping the vegetation distribution of the permafrost zone on the qinghai-tibet plateau. *Journal of Mountain Science*, *13*, 1035–1046. doi: https://doi.org/10.1007/s11629-015-3485-y

Wei, D., Qi, Y., Ma, Y., & Wang, X. (2021). Plant uptake of co_2 outpaces losses from permafrost and plant respiration on the tibetan plateau. *Proceedings of the National Academy of Sciences*, *118*, e2015283118. doi: https://doi.org/10.1073/pnas.2015283118

Wei, Y., Lu, H., Wang, J., Wang, X., & Sun, J. (2022). Dual influence of climate change and anthropogenic activities on the spatiotemporal vegetation dynamics over the qinghai-tibetan plateau from 1981 to 2015. *Earth's Future*, *10*, e2021EF002566. doi: https://doi.org/10.1029/2021EF002566

Westermann, S., Ingeman-Nielsen, T., Scheer, J., Aalstad, K., Aga, J., Chaudhary, N., … Langer, M. (2023). The cryogrid community model (version 1.0) – a multi-physics toolbox for climate-driven simulations in the terrestrial cryosphere. *Geoscientific Model Development*, *16*, 2607–2647. doi: https://doi.org/10.5194/gmd-16-2607-2023

Westermann, S., Langer, M., Boike, J., Heikenfeld, M., Peter, M., Etzelmüller, B., & Krinner, G. (2016). Simulating the thermal regime and thaw processes of ice-rich permafrost ground with the land-surface model cryogrid3. *Geoscientific Model Development*, *9*, 523–546. doi: https://doi.org/10.5194/gmd-9-523-2016

Wu, M., Chen, S., Chen, J., Xue, K., Chen, S., Wang, X., … Wang, Y. (2021). Reduced microbial stability in the active layer is associated with carbon loss under alpine permafrost degradation. *Proceedings of the National Academy of Sciences*, *118*, e2025321118. doi: https://doi.org/10.1073/pnas.2025321118

Wu, Q., & Zhang, T. (2008). Recent permafrost warming on the qinghai-tibetan plateau. *Journal of Geophysical Research: Atmospheres*, *113*, D13108. doi: https://doi.org/10.1029/2007JD009539

Wu, Q., & Zhang, T. (2010). Changes in active layer thickness over the qinghai-tibetan plateau from 1995 to 2007. *Journal of Geophysical Research: Atmospheres*, *115*, D09107. doi: https://doi.org/10.1029/2009JD012974

Wu, Q., Zhang, T., & Liu, Y. (2020). Thermal state of the active layer and permafrost along the qinghai-xizang (tibet) railway from 2006 to 2010. *The Cryosphere*, *31*, 417–428. doi: https://doi.org/10.1002/ppp.2059

Xia, Z., Huang, L., Fan, C., Jia, S., Lin, Z., Liu, L., … Zhang, T. (2022). Retrogressive thaw slumps along the qinghai–tibet engineering corridor: a comprehensive inventory and their distribution characteristics. *Earth System Science Data*, *14*, 3875–3887. doi: https://doi.org/10.5194/essd-14-3875-2022

Yan, F., Shangguan, W., Zhang, J., & Hu, B. (2020). Depth-to-bedrock map of china at a spatial resolution of 100 meters. *Scientific Data*, *7*, 2. doi: https://doi.org/10.1038/s41597-019-0345-6

Yang, J., Xin, Z., Huang, Y., & Liang, X. (2023). Multi-source remote sensing data shows a significant increase in vegetation on the tibetan plateau since 2000.

Progress in Physical Geography: Earth and Environment, *47*, 597–624. doi: https://doi.org/10.1177/03091333221148052

Yi, S., Wang, X., Qin, Y., Xiang, B., & Ding, Y. (2014). Responses of alpine grassland on qinghai–tibetan plateau to climate warming and permafrost degradation: a modeling perspective. *Environmental Research Letters*, *9*, 074014. doi: https://doi.org/10.1088/1748-9326/9/7/074014

Yin, G., Niu, F., Lin, Z., Luo, J., & Liu, M. (2021). Data-driven spatiotemporal projections of shallow permafrost based on cmip6 across the qinghai–tibet plateau at 1 km^2 scale. *Advances in Climate Change Research*, *12*, 814—827. doi: https://doi.org/10.1016/j.accre.2021.08.009

Zhang, G., Luo, W., Chen, W., & Zheng, G. (2019). A robust but variable lake expansion on the tibetan plateau. *Science Bulletin*, *64*, 1306–1309. doi: https://doi.org/10.1016/j.scib.2019.07.018

Zhang, G., Nan, Z., Hu, N., Yin, Z., Zhao, L., Cheng, G., & Mu, C. (2022). Qinghai-tibet plateau permafrost at risk in the late 21st century. *Earth's Future*, *10*, e2022EF002652. doi: https://doi.org/10.1029/2022EF002652

Zhang, G., Nan, Z., Zhao, L., Liang, Y., & Cheng, G. (2021). Qinghai-tibet plateau wetting reduces permafrost thermal responses to climate warming. *Earth and Planetary Science Letters*, *562*, 116858. doi: https://doi.org/10.1016/j.epsl.2021.116858

Zhang, Q., Kong, D., Shi, P., Singh, V. P., & Sun, P. (2018). Vegetation phenology on the qinghai-tibetan plateau and its response to climate change (1982–2013). *Agricultural and Forest Meteorology*, *248*, 408–417. doi: https://doi.org/10.1016/j.agrformet.2017.10.026

Zhang, X., & Li, X. (2023). Three-dimensional differentiation of the contribution of climatic factors to vegetation change in the pan-tibetan plateau. *Journal of Geophysical Research: Biogeosciences*, *128*, e2022JG007244. doi: https://doi.org/10.1029/2022JG007244

Zhang, Y., Li, B., & Zheng, D. (2014). Datasets of the boundary and area of the tibetan plateau. *Acta Geographica Sinica*, *69*, 65–68. doi: https://doi.org/10.11821/dlxb2014S012

Zhang, Z., Wu, Q., Jiang, G., Gao, S., Chen, J., & Liu, Y. (2020). Changes in the permafrost temperatures from 2003 to 2015 in the qinghai-tibet plateau. *Cold Regions Science and Technology*, *169*, 102904. doi: https://doi.org/10.1016/j.coldregions.2019.102904

Zhao, L., Zou, D., Hu, G., Wu, T., Du, E., Liu, G., ... Cheng, G. (2021). A synthesis dataset of permafrost thermal state for the qinghai–tibet (xizang) plateau, china. *Earth System Science Data*, *13*, 4207–4218. doi: https://doi.org/10.5194/essd-13-4207-2021

Zhou, J., Zheng, Y., Song, C., Cheng, C., Gao, P., & Ye, S. (2022). *Vegetation map of qinghai tibet plateau in 1980s.* National Tibetan Plateau Data Center. doi: https://doi.org/10.11888/Terre.tpdc.272385

Zou, D., Zhao, L., Sheng, Y., Chen, J., Hu, G., Wu, T., ... Cheng, G. (2017). A new map of permafrost distribution on the tibetan plateau. *The Cryosphere7*, *11*, 2527–2542. doi: https://doi.org/10.5194/tc-11-2527-2017

Supporting Information for "Potential vegetation changes in the permafrost areas over the Tibetan Plateau under future climate warming"

Rui Chen[1,2], Jan Nitzbon[1], Thomas Schneider von Deimling[1], Simone Maria Stuenzi[1], Ngai-Ham Chan[1], Julia Boike[1,2], and Moritz Langer[1,3]

[1]Permafrost Research Section, Alfred Wegener Institute Helmholtz Centre for Polar and Marine Research, Potsdam, Germany

[2]Geography Department, Humboldt-Universität zu Berlin, Berlin, Germany

[3]Department of Earth Sciences, Vrije Universiteit Amsterdam, Amsterdam, the Netherlands

Contents of this file

Text S1. Description of surface energy balance and hydrology scheme in CryoGridLite

S1.1 The surface energy balance scheme

In comparison to the CryoGridLite model, as described in (Langer et al., 2024), where the upper boundary conditions to the heat conduction equation were set by the air temperature, the CryoGridLite version used in this study solves the surface energy balance equation to calculate the ground heat flux Q_g and translates it into a surface temperature T_surf:

$$T_\mathrm{surf} = T_1 + \frac{Q_\mathrm{g}\Delta z_1}{2\,k_1} \tag{1}$$

where T_1 is the current temperature, Δz_1 is the thickness, and k_1 is the current thermal conductivity of the uppermost grid cell (soil or snow). For this, Q_g is calculated as the residual of the heat fluxes at the surface:

$$Q_\mathrm{g} = Q_\mathrm{net} - Q_\mathrm{h} - Q_\mathrm{e} \tag{2}$$

where Q_net is the net radiation, Q_h the sensible and Q_e the latent turbulent heat flux. In Eq. (2), Q_net is calculated from the incoming and outgoing fluxes of short- and longwave radiation:

$$Q_\mathrm{net} = S_\mathrm{in} + S_\mathrm{out} + L_\mathrm{in} + L_\mathrm{out} \tag{3}$$

where S_{in} and L_{in} are incoming shortwave and longwave radiation provided by the forcing data, and S_{out} and L_{out} are the outgoing shortwave and longwave radiation calculated by albedo and Kirchhoff's and Stefan-Boltzmann's law:

$$S_\mathrm{out} = -\alpha S_\mathrm{in} \tag{4}$$

$$L_\mathrm{out} = -\epsilon\,\sigma\,{T_\mathrm{surf}^{t-1}}^4 - (1-\epsilon)L_\mathrm{in} \tag{5}$$

with α the albedo and ϵ the emissivity, both depending on the surface condition (see table Table S1 for values), and σ the Stefan-Boltzmann constant.

In Eq. (2), the turbulent fluxes are calculated according to the Monin-Obukhov similarity theory where Q_h and Q_e are parameterized based on the gradients of temperature and absolute humidity between the surface and a certain height above it. Differing from the scheme used by Westermann et al. (2016), we adopted Byun's scheme (Byun, 1990) to calculate the Obukhov stability parameter $L^\star$, using the parameterizations of the atmospheric stability functions suggested by Businger, Wyngaard, Izumi, and Bradley (1971).

Similar to Nitzbon et al. (2019), we reduced the latent heat flux Q_e during the snow-free season according to the availability of liquid water content (θ) close to the surface:

$$Q_\mathrm{e} = \beta\, Q_\mathrm{e}^\mathrm{pot} \tag{6}$$

where the water availability factor $\beta \in [0, 1]$ is obtained by summing the following weighting factors Θ_* over the subsurface grid cells 1 to N:

$$\beta = \textstyle\sum_{i=1}^{N} \Theta_{T_i}\, \Theta_{\theta_i}\, \Theta_{z_i} \tag{7}$$

$$\text{where} \quad \Theta_{T_i} = \begin{cases} 1 & \text{if } T_i > 0°\mathrm{C} \\ 0 & \text{else,} \end{cases} \tag{8}$$

$$\Theta_{\theta_i} = \begin{cases} 1 & \text{if } \theta_i > \theta_\mathrm{fc} \\ 0.25\left(1-\cos\left(\frac{\pi\theta_i}{\theta_\mathrm{fc}}\right)\right)^2 & \text{else,} \end{cases} \tag{9}$$

$$\Theta_{z_i} = \frac{e^{-\frac{z_i}{d_\mathrm{E}}}\Delta z_i}{\sum_i e^{-\frac{z_i}{d_\mathrm{E}}}\Delta z_i} \tag{10}$$

Here Θ_{T_i} ensures that only unfrozen grid cells are considered, Θ_{θ_i} reduces the water availability if the liquid water content is below field capacity θ_fc, and Θ_{z_i} is a depth-weighting according to the evaporation depth d_E and the denominator a normalization such that $\beta \in [0, 1]$.

S1.1 The surface energy balance scheme

In this tailored version of the CryoGridLite model, we largely followed (Nitzbon et al., 2019) to incorporate a simple 'bucket' scheme to calculate the dynamics of soil water content. The hydrology scheme is run at the hourly timestep ($\Delta t = 1\,\mathrm{hour}$) of the model and only in the absence of a snowpack. First, the potential water to be infiltrated into or removed from the soil column (ΔI (m)) is determined by taking the difference between rainfall (P_{rain}) and evapotranspiration.

$$\Delta I = P_{\mathrm{rain}}\Delta t - \frac{Q_e\,\Delta t}{\rho_{\mathrm{w}}\,L_{\mathrm{sl}}} \tag{11}$$

If $\Delta I > 0$, the distribution of soil water content along the vertical soil profile is derived from the infiltration process under the influence of gravity: if the water content in a cell exceeds the given value of maximum water content, the water is routed to the layer below until it eventually reaches a frozen grid cell. If there is still excess water present, the soil layers will commence saturation from the bottom upwards. In scenarios where excess water remains even after completely saturating the pore space of soil, it is then removed as surface runoff.

If $\Delta I < 0$, soil water is successively removed in a similar procedure, by reducing the water content to at least a residual water content (θ_{rs}) starting from the first subsurface layer and continuing downwards until the water deficit is applied.

References

Businger, J. A., Wyngaard, J. C., Izumi, Y., & Bradley, E. F. (1971). Flux-profile relationships in the atmospheric surface layer. *Journal of the Atmospheric Sciences*, *28*, 181–189. doi: https://doi.org/10.1175/1520-0469(1971)028⟨0181:FPRITA⟩2.0.CO;2

Byun, D. W. (1990). On the analytical solutions of flux-profile relationships for the atmospheric surface layer. *Journal of Applied Meteorology and Climatology*, *29*, 652–657. doi: https://doi.org/10.1175/1520-0450(1990)029⟨0652:OTASOF⟩2.0.CO;2

Chang, Y., Lyu, S., Luo, S., Li, Z., Fang, X., Chen, B., ... Chen, S. (2018). Estimation of permafrost on the tibetan plateau under current and future climate conditions using the cmip5 data. *International Journal of Climatology*, *38*, 5659–5676. doi: https://doi.org/10.1002/joc.5770

Chen, H., Nan, Z., Zhao, L., Ding, Y., Chen, J., & Pang, Q. (2015). Noah modelling of the permafrost distribution and characteristics in the west kunlun area, qinghai-tibet plateau, china. *Permafrost and Periglacial Processes*, *26*, 160–174. doi: https://doi.org/10.1002/ppp.1841

Chen, J., Zhao, L., Sheng, Y., Li, J., Wu, X., Du, E., ... Pang, Q. (2016). Some characteristics of permafrost and its distribution in the gaize area on the qinghai-tibet plateau, china. *Arctic, Antarctic, and Alpine Research*, *48*, 395–409. doi: https://doi.org/10.1657/AAAR0014-023

Cuo, L., Zhang, Y., & Li, N. (2022). Historical and future vegetation changes in the degraded frozen soil and the entire tibetan plateau and climate drivers. *Journal of Geophysical Research: Biogeosciences*, *127*, e2022JG006987. doi: https://doi.org/

10.1029/2022JG006987

Dai, L., Che, T., Xie, H., & Wu, X. (2018). Estimation of snow depth over the qinghai-tibetan plateau based on amsr-e and modis data. *Remote Sensing*, *10*, 1989. doi: https://doi.org/10.3390/rs10121989

Gao, Y., Luo, D., Chen, F., Lei, W., & Jin, H. (2023). Characteristics of the thermal regime and freeze-thaw cycles on the ground surface in permafrost regions in the headwater area of the yellow river. *Acta Geographica Sinica*, *78*, 604–619. doi: https://geog.com.cn/EN/10.11821/dlxb202303007

Guo, D., & Wang, H. (2013). Simulation of permafrost and seasonally frozen ground conditions on the tibetan plateau, 1981–2010. *Journal of Geophysical Research: Atmospheres*, *118*, 5216–5230. doi: https://doi.org/10.1002/jgrd.50457

Guo, D., & Wang, H. (2016). Cmip5 permafrost degradation projection:a comparison among different regions. *Journal of Geophysical Research: Atmospheres*, *121*, 4499–4517. doi: https://doi.org/10.1002/2015JD024108

Ji, F., Fan, L., Kuang, X., Li, X., Cao, B., Cheng, G., ... Zheng, C. (2022). How does soil water content influence permafrost evolution on the qinghai-tibet plateau under climate warming? *Environmental Research Letters*, *17*, 064012. doi: https://doi.org/10.1088/1748-9326/ac6c9a

Langer, M., Nitzbon, J., Groenke, B., Assmann, L.-M., von Deimling, T. S., Stuenzi, S. M., & Westermann, S. (2024). The evolution of arctic permafrost over the last 3 centuries from ensemble simulations with the cryogridlite permafrost model. *The Cryosphere*, *18*, 363–385. doi: https://doi.org/10.5194/tc-18-363-2024

Li, H., Pan, X., Washakh, R. M. A., & Nie, X. (2024). A new method of diagnosing the historical and projected changes in permafrost on the tibetan plateau. *Earth's Future*, *12*, e2023EF003897. doi: https://doi.org/10.1029/2023EF003897

Li, R., Zhang, M., Andreeva, V., Pei, W., Zhou, Y., Misailov, I., & Basharin, N. (2023). Impact of climate warming on permafrost changes in the qinghai-tibet plateau. *Cold Regions Science and Technology*, *205*, 103692. doi: https://doi.org/10.1016/j.coldregions.2022.103692

Lu, Q., Zhao, D., & Wu, S. (2017). Simulated responses of permafrost distribution to climate change on the qinghai–tibet plateau. *Scientific Reports*, *7*, 3845. doi: https://doi.org/10.1038/s41598-017-04140-7

Luo, D., Jin, H., Jin, X., He, R., Li, X., Muskett, R. R., ... Romanovsky, V. E. (2018). Elevation-dependent thermal regime and dynamics of frozen ground in the bayan har mountains, northeastern qinghai-tibet plateau, southwest china. *Permafrost and Periglacial Processes*, *29*, 257–270. doi: https://doi.org/10.1002/ppp.1988

Mu, C., & Peng, X. (2022). *A synthesis dataset of frozen ground and soil carbon in heihe river basin qilian mountainous (2011–2020).* National Tibetan Plateau Data Center. doi: https://doi.org/10.11888/Cryos.tpdc.272840

Ni, J., Wu, T., Zhu, X., Hu, G., Zou, D., Wu, X., ... Yang, C. (2021). Simulation of the present and future projection of permafrost on the qinghai-tibet plateau with statistical and machine learning models. *Journal of Geophysical Research: Atmospheres*, *126*, e2020JD033402. doi: https://doi.org/10.1029/2020JD033402

Nitzbon, J., Langer, M., Westermann, S., Martin, L., Aas, K. S., & Boike, J. (2019). Pathways of ice-wedge degradation in polygonal tundra under different hydrological conditions. *The Cryosphere*, *13*, 1089–1123. doi: https://doi.org/10.5194/tc-13-1089

-2019

Qin, Y., Wu, T., Zhao, L., Wu, X., Li, R., Xie, C., ... Hao, J. (2017). Numerical modeling of the active layer thickness and permafrost thermal state across qinghai-tibetan plateau. *Journal of Geophysical Research: Atmospheres*, *122*, 11604–11620. doi: https://doi.org/10.1002/2017JD026858

Ran, Y., Cheng, G., Dong, Y., Hjort, J., Lovecraft, A. L., Kang, S., ... Li, X. (2022). Permafrost degradation increases risk and large future costs of infrastructure on the third pole. *Communications Earth & Environment*, *3*, 238. doi: https://doi.org/10.1038/s43247-022-00568-6

Ran, Y., Li, X., & Cheng, G. (2018). Climate warming over the past half century has led to thermal degradation of permafrost on the qinghai–tibet plateau. *The Cryosphere*, *12*, 595–608. doi: https://doi.org/10.5194/tc-12-595-2018

Ran, Y., Li, X., Cheng, G., Nan, Z., Che, J., Sheng, Y., ... Wu, X. (2021). Mapping the permafrost stability on the tibetan plateau for 2005–2015. *Science China Earth Sciences*, *64*, 62–79. doi: https://doi.org/10.1007/s11430-020-9685-3

Shen, T., Jiang, P., Ju, Q., Yu, Z., Chen, X., Lin, H., & Zhang, Y. (2023). Changes in permafrost spatial distribution and active layer thickness from 1980 to 2020 on the tibet plateau. *Science of The Total Environment*, *859*, 160381. doi: https://doi.org/10.1016/j.scitotenv.2022.160381

Wang, W., Yang, K., Zhao, L., Zheng, Z., Lu, H., Mamtimin, A., ... Moore, J. C. (2020). Characterizing surface albedo of shallow fresh snow and its importance for snow ablation on the interior of the tibetan plateau. *Journal of Hydrometeorology*, *21*, 815–827. doi: https://doi.org/10.1175/JHM-D-19-0193.1

Westermann, S., Langer, M., Boike, J., Heikenfeld, M., Peter, M., Etzelmüller, B., & Krinner, G. (2016). Simulating the thermal regime and thaw processes of ice-rich permafrost ground with the land-surface model cryogrid3. *Geoscientific Model Development*, *9*, 523–546. doi: https://doi.org/10.5194/gmd-9-523-2016

Wu, Q., Zhang, T., & Liu, Y. (2020). Thermal state of the active layer and permafrost along the qinghai-xizang (tibet) railway from 2006 to 2010. *The Cryosphere*, *31*, 417–428. doi: https://doi.org/10.1002/ppp.2059

Wu, X., Nan, Z., Zhao, S., Zhao, L., & Cheng, G. (2018). Spatial modeling of permafrost distribution and properties on the qinghai-tibet plateau. *Permafrost and Periglacial Processes*, *29*, 86–99. doi: https://doi.org/10.1002/ppp.1971v

Xu, X., & Wu, Q. (2021). Active layer thickness variation on the qinghai-tibetan plateau: Historical and projected trends. *Journal of Geophysical Research: Atmospheres*, *126*, e2021JD034841. doi: https://doi.org/10.1029/2021JD034841

Yin, G., Niu, F., Lin, Z., Luo, J., & Liu, M. (2021). Data-driven spatiotemporal projections of shallow permafrost based on cmip6 across the qinghai–tibet plateau at 1 km^2 scale. *Advances in Climate Change Research*, *12*, 814—827. doi: https://doi.org/10.1016/j.accre.2021.08.009

Zhang, G., Nan, Z., Hu, N., Yin, Z., Zhao, L., Cheng, G., & Mu, C. (2022). Qinghai-tibet plateau permafrost at risk in the late 21st century. *Earth's Future*, *10*, e2022EF002652. doi: https://doi.org/10.1029/2022EF002652

Zhang, W., Ren, Z., Yao, L., Zhou, C., & Zhu, Y. (2016). Numerical modeling and prediction of future response of permafrost to different climate change scenarios on the qinghai–tibet plateau. *International Journal of Digital Earth*, *9*, 442–456. doi:

https://doi.org/10.1080/17538947.2015.1041431

Zhang, Z., Wu, Q., Jiang, G., Gao, S., Chen, J., & Liu, Y. (2020). Changes in the permafrost temperatures from 2003 to 2015 in the qinghai-tibet plateau. *Cold Regions Science and Technology*, *169*, 102904. doi: https://doi.org/10.1016/j.coldregions.2019.102904

Zhao, L., Zou, D., Hu, G., Wu, T., Du, E., Liu, G., ... Cheng, G. (2021). A synthesis dataset of permafrost thermal state for the qinghai–tibet (xizang) plateau, china. *Earth System Science Data*, *13*, 4207–4218. doi: https://doi.org/10.5194/essd-13-4207-2021

Zou, D., Zhao, L., Sheng, Y., Chen, J., Hu, G., Wu, T., ... Cheng, G. (2017). A new map of permafrost distribution on the tibetan plateau. *The Cryosphere7*, *11*, 2527–2542. doi: https://doi.org/10.5194/tc-11-2527-2017

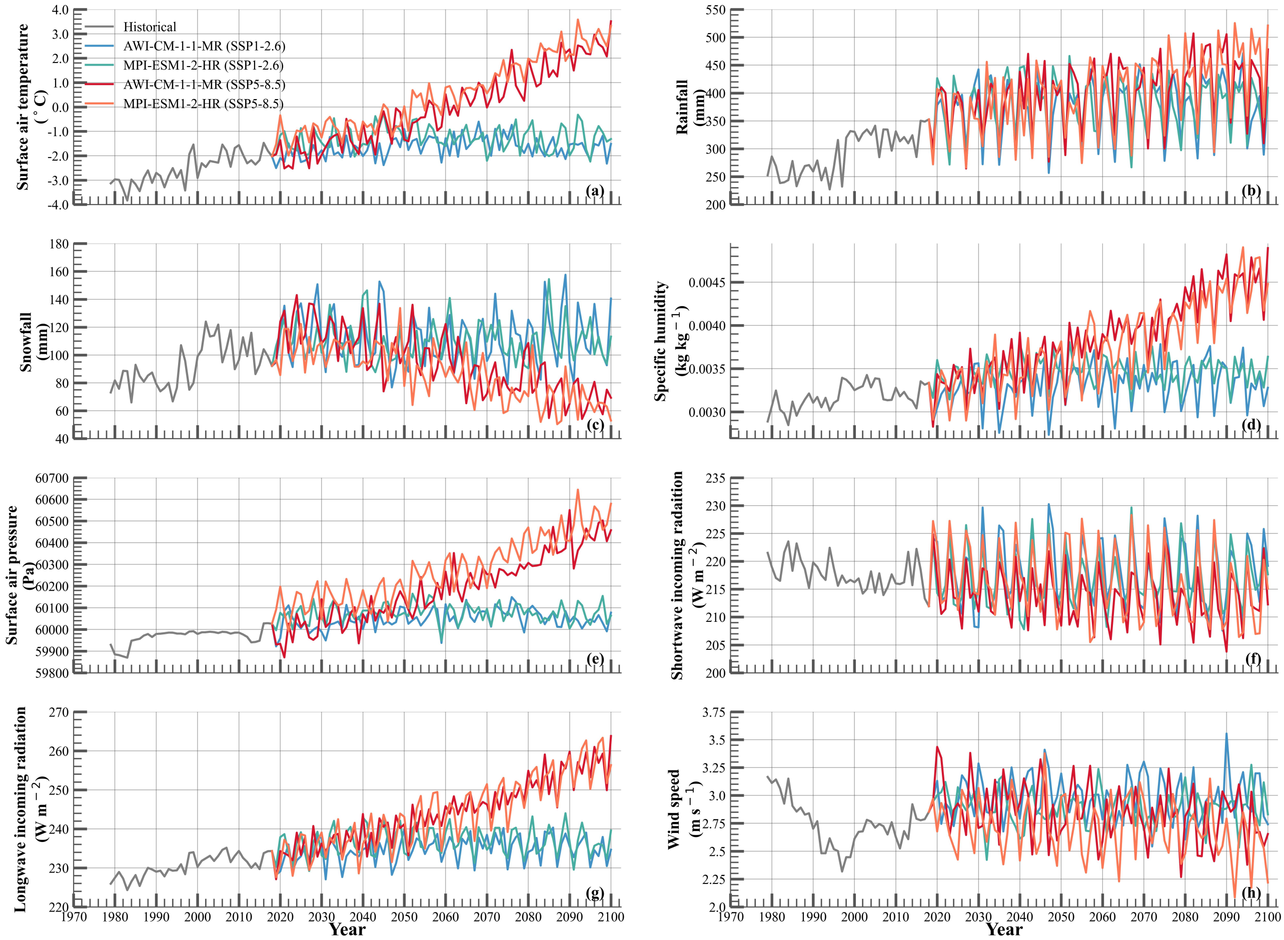

Figure S1. Timeseries of forcing variables (surface air temperature (a), rainfall (b), snowfall (c), specific humidity, surface air pressure (d), incoming shortwave radiation (e), incoming longwave radiation (f), and wind speed (g)) during 1979–2100 over the Tibetan Plateau under two different scenarios and two Global Climate Models.

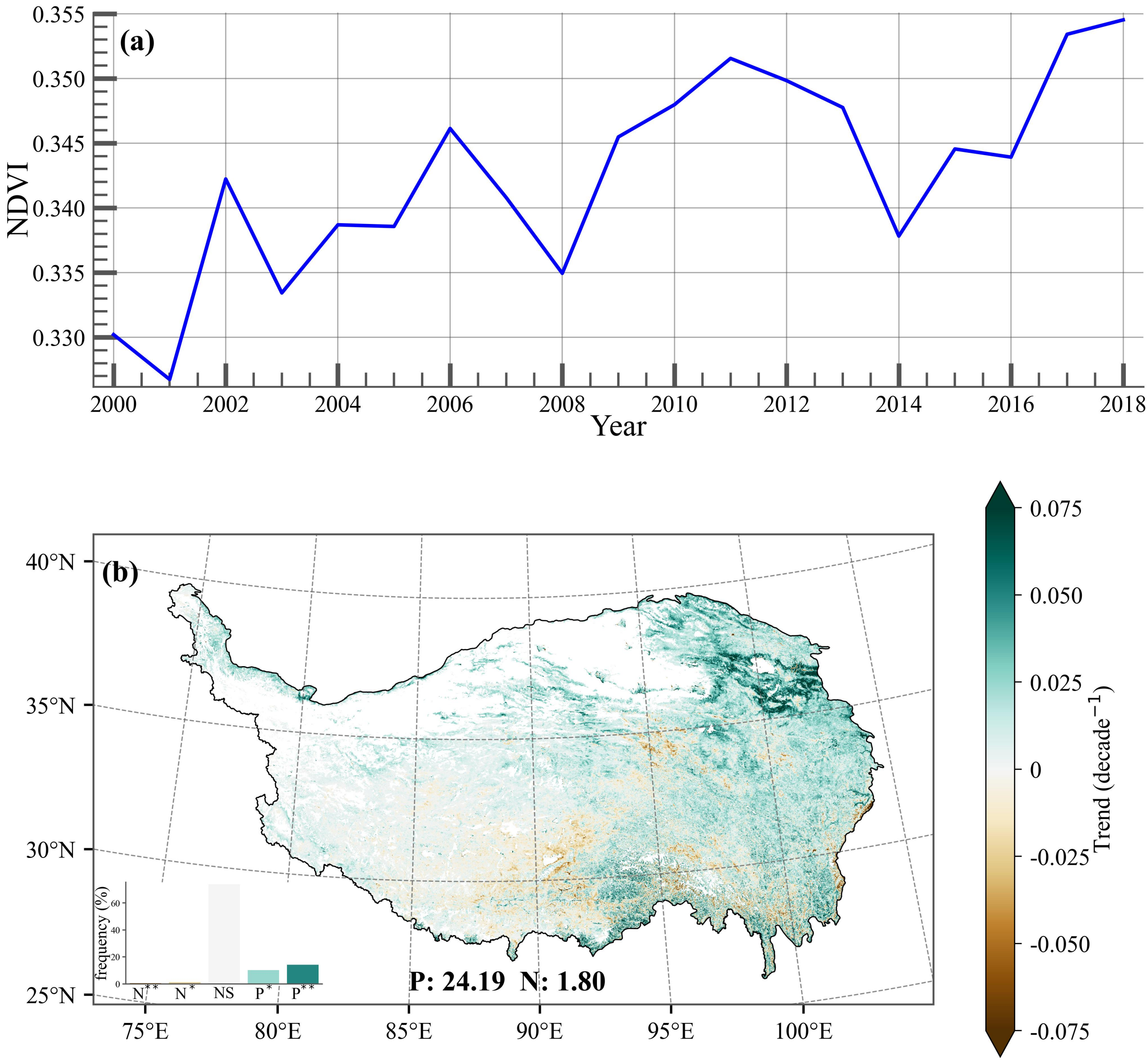

Figure S2. Spatiotemporal patterns of the changes of the growing season (May to September) NDVI on the Tibetan Plateau at 1km^2 from MODIS satellite imagery. (a) Time evolution of the growing season NDVI on the Tibetan Plateau. (b) spatial distribution of the trend of the growing season NDVI on the Tibetan Plateau. The sub-barplot represents the percentage of the number of grid cells of NDVI in each significant level to the total number of grid cells. N, NS, and P indicate negative, non-significant, and positive trends, respectively. $*$ and $**$ represent significance at p-value $\leq$0.05 and $\leq$0.01, respectively.

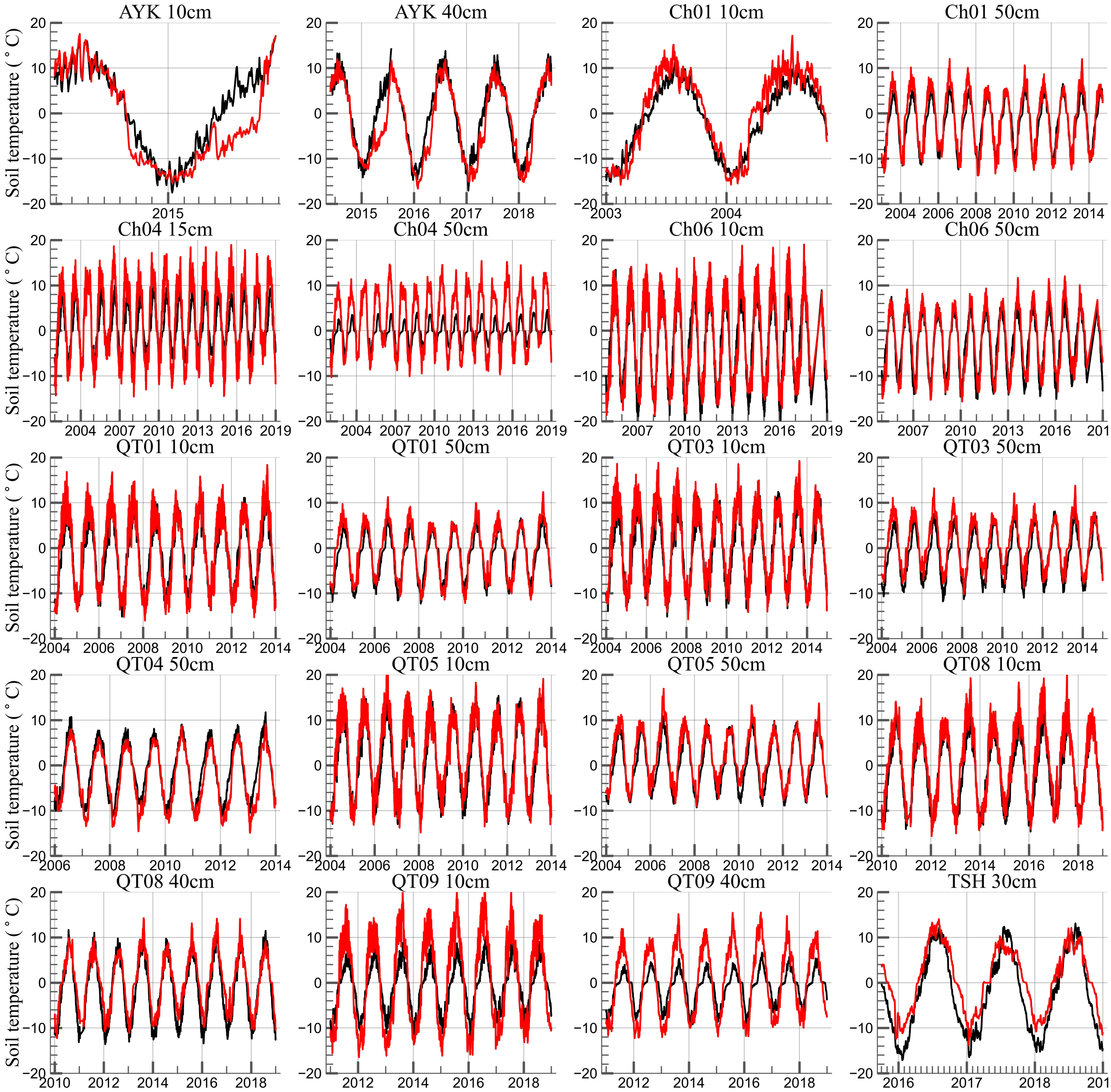

Figure S3. Comparison of the simulated and observed soil temperature in the upper soil layer (above 50cm). Observed soil temperature derived from Zhao et al. (2021).

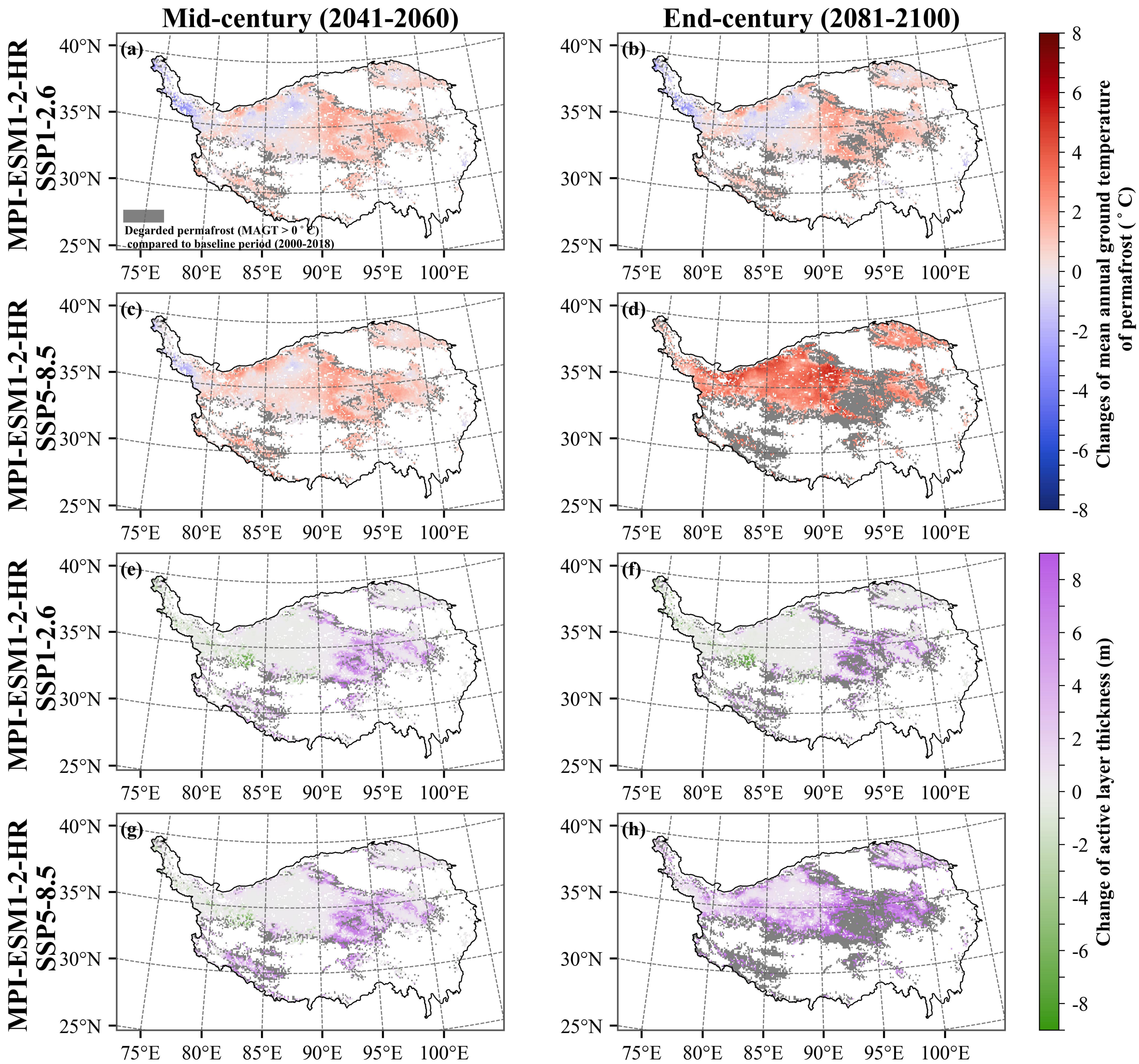

Figure S4. Spatial changes of the mean annual ground temperature (a-d) and active layer thickness (e-h) on the Tibetan Plateau by mid-century (2041–2060) and end-century(2081–2100) under SSP1–2.6 and SSP5–8.5 scenarios from MPI-ESM1-2-HR, related to the baseline period (2000–2018), respectively.

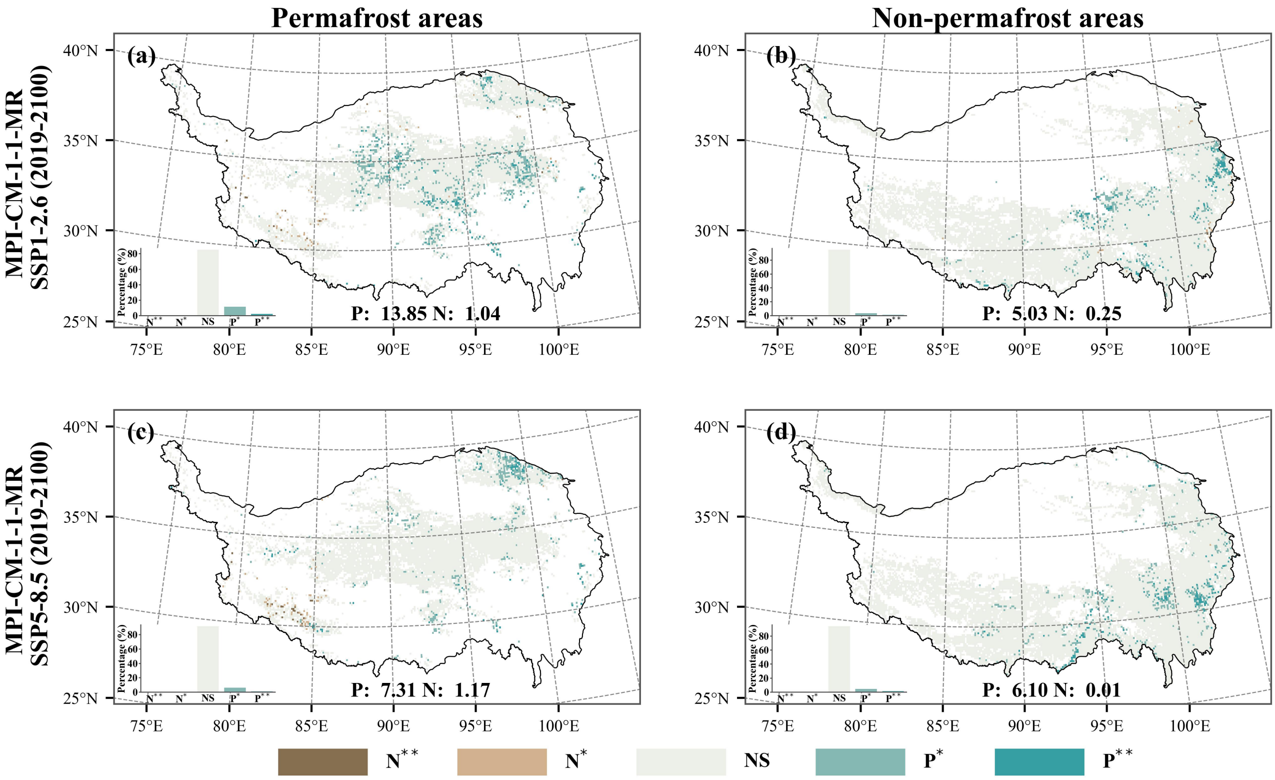

Figure S5. Spatial patterns of annual NDVI$_{GS}$ trend across the permafrost areas during the historical (2000–2018) and future periods (2019–2050) from MPI-ESM1-2-HR. N, NS, and P indicate negative, non-significant, and positive trends. * and ** represent significance at p-value < 0.05 and 0.01, respectively.

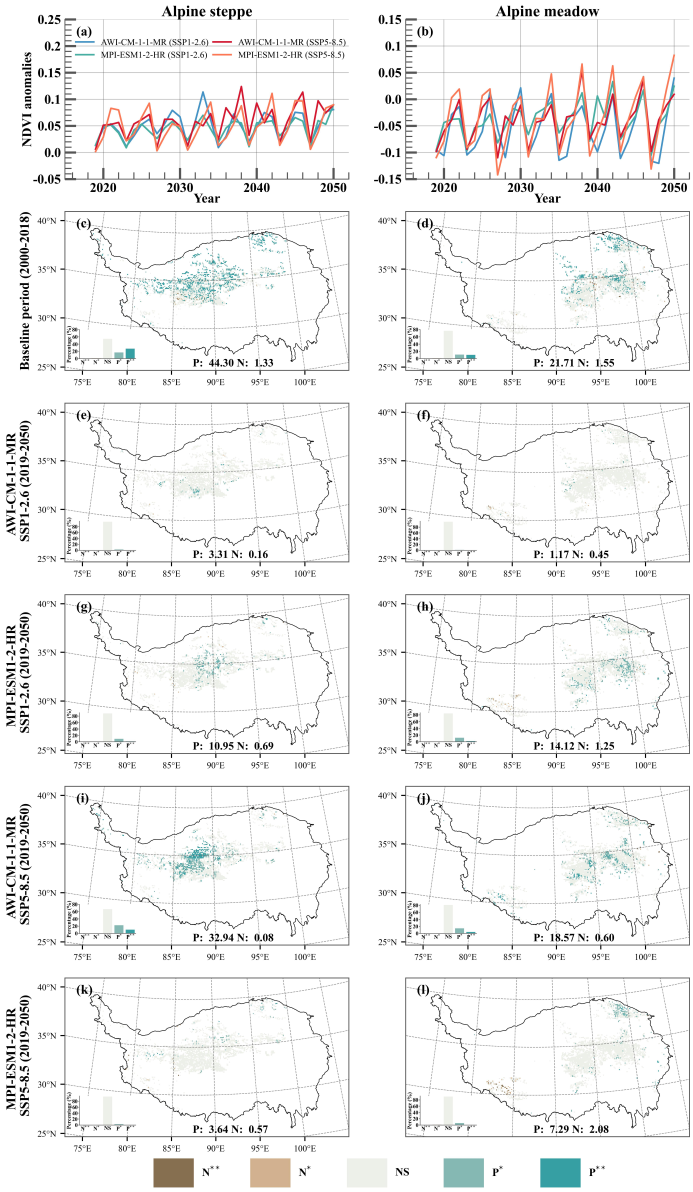

Figure S6. (a-b) Time series of annual NDVI$_{GS}$ anomalies (minus the mean value from 2000–2018) from 2019 to 2050 under the future climate conditions on the alpine meadow and alpine steppe on the permafrost areas over the Tibetan Plateau. The blue, red, green, and orange lines represent SSP1–2.6 and SSP5–8.5 scenarios from AWI-CM-1-1-MR and MPI-ESM1-2-HR, respectively. (c-l) Spatial patterns of annual NDVI$_{GS}$ trend during the historical (2000–2018) and future periods (2019–2050) under different climate scenarios from AWI-CM-1-1-MR and MPI-ESM1-2-HR. N, NS, and P indicate negative, non-significant, and positive trends. * and ** represent significance at p-value $<$ 0.05 and 0.01, respectively.

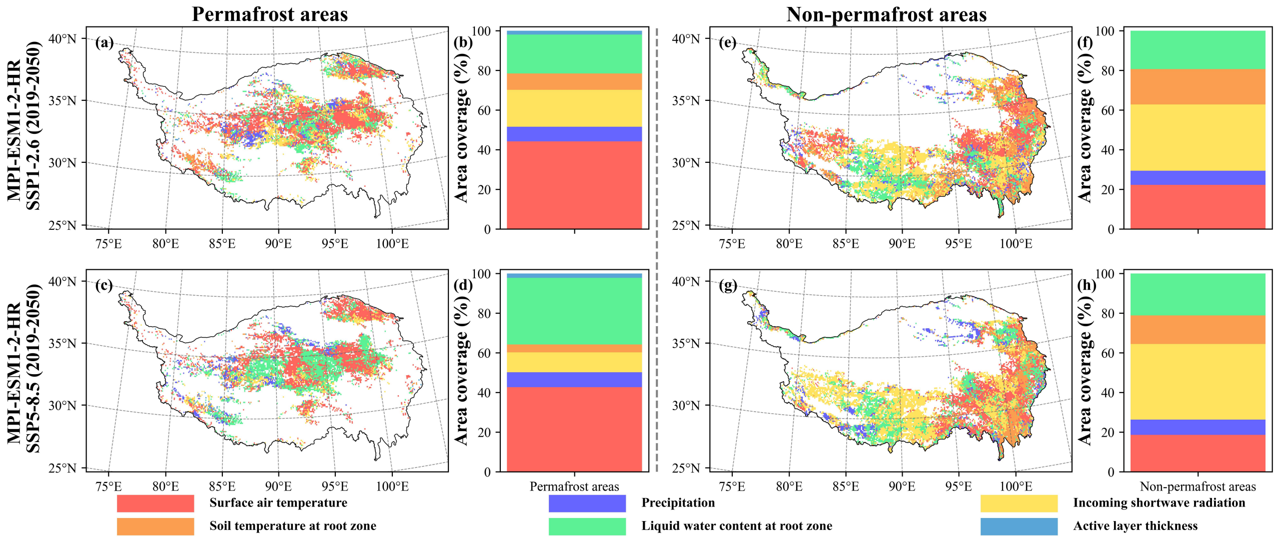

Figure S7. Spatial distribution of the dominant factors to the NDVI$_{GS}$ changes over different periods in the permafrost and non-permafrost areas. (a-d) Future period (SSP1–2.6; 2019–2050; MPI-ESM1-2-HR). (e-h) Future period (SSP5–8.5; 2019–2050; MPI-ESM1-2-HR). The barplot (b, d, f, h) represents the proportion of the contribution of each variable in the permafrost and non-permafrost areas with significantly increased NDVI$_{GS}$ from MPI-ESM1-2-HR.

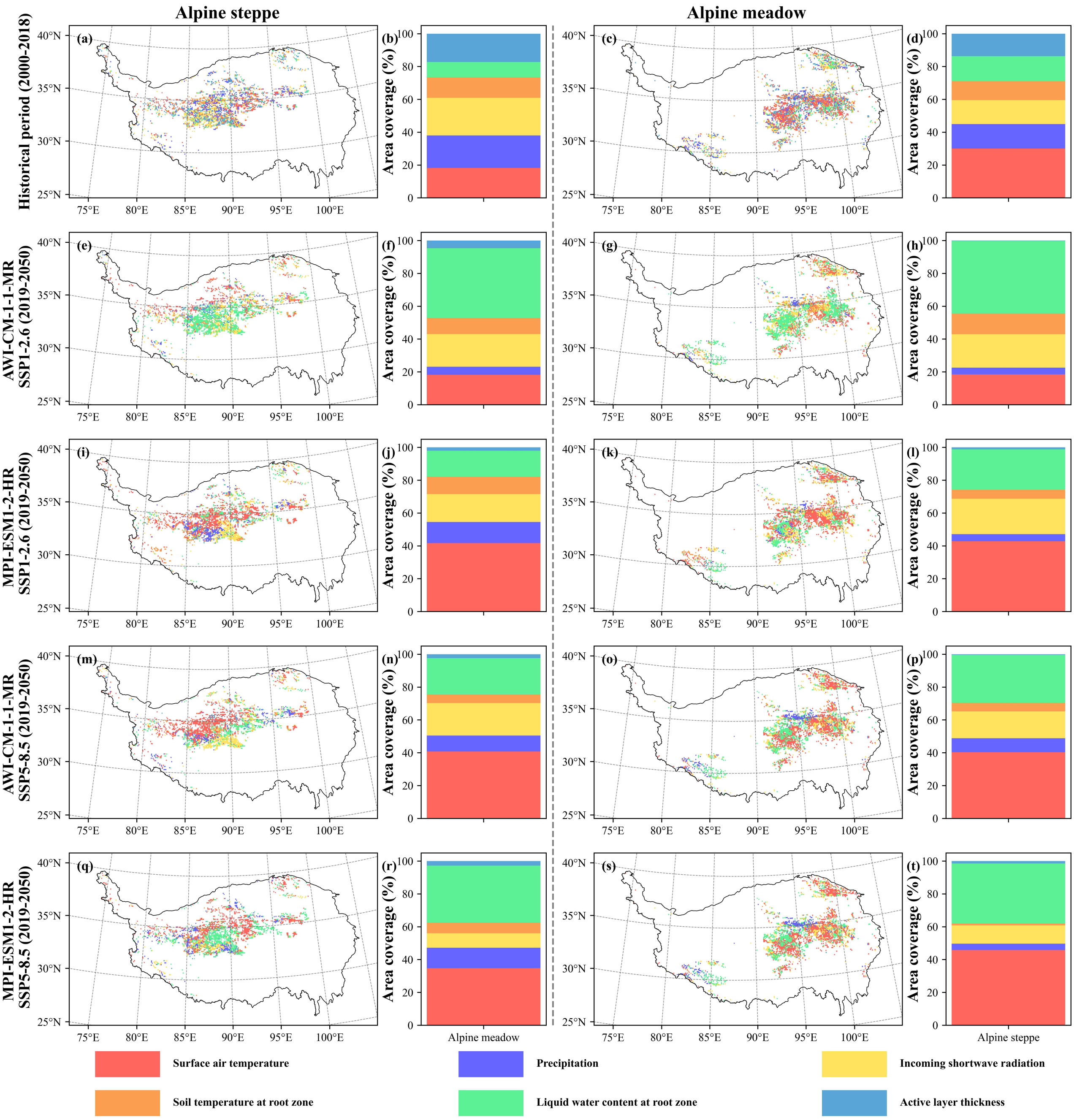

Figure S8. Spatial distribution of the dominant factors to the NDVI$_{GS}$ changes over different periods in the alpine meadow and alpine steppe over the permafrost areas. (a-d) Historical period (2000–2018). (e-h) Future period (SSP1–2.6; AWI-CM-1-1-MR). (i-l) Future period (SSP1–2.6; MPI-ESM1-2-HR). (m-p) Future period (SSP5–8.5; AWI-CM-1-1-MR). (q-t) Future period (SSP5–8.5; MPI-ESM1-2-HR). The barplot (b, d, f, h, j, l, n, p, r, t) represents the proportion of the contribution of each variable in the permafrost and non-permafrost with significantly increased NDVI$_{GS}$ from AWI-CM-1-1-MR and MPI-ESM1-2-HR.

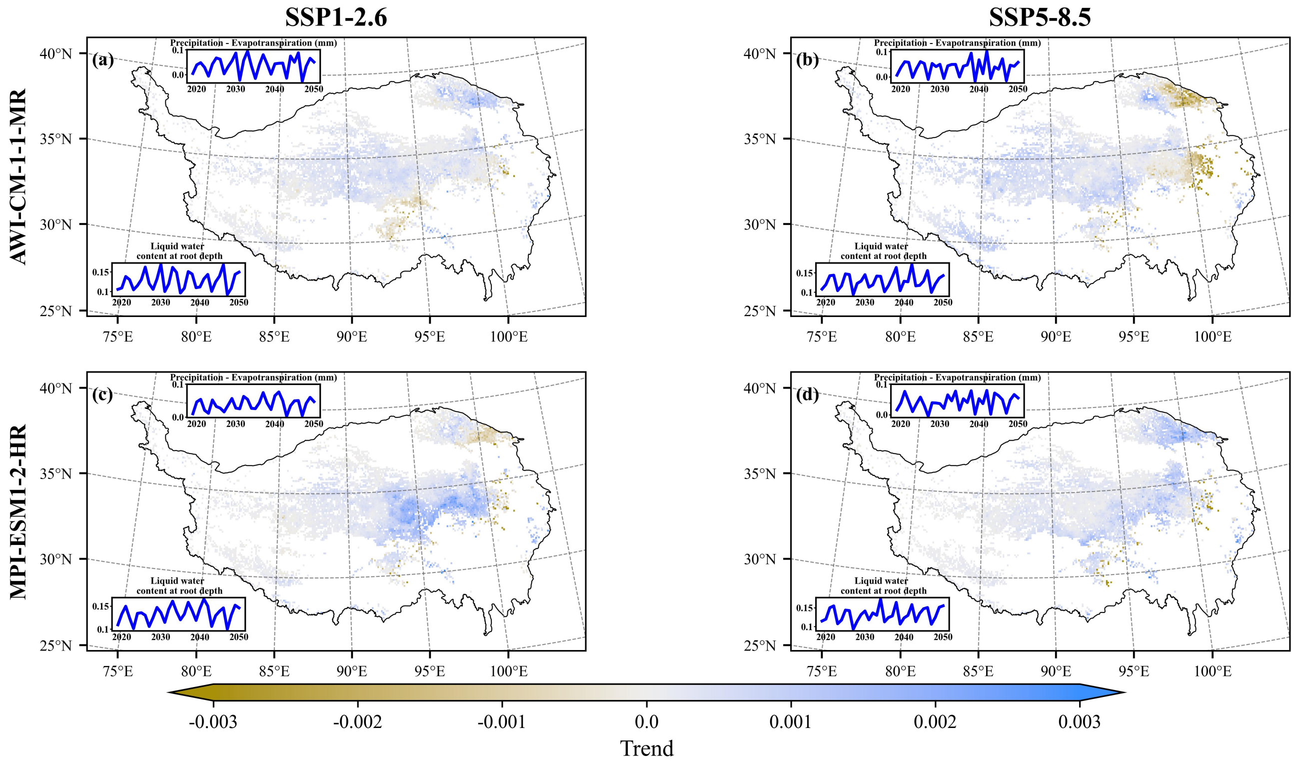

Figure S9. Spatiotemporal patterns of the changes of liquid water content at root zone across the permafrost areas during 2019–2050 under different scenarios. (a-b) AWI-CM-1-1-MR. (c-d) MPI-ESM1-2-HR. The line plots at each subplot indicate the time series of liquid water content at the root zone (bottom left) and precipitation minus evapotranspiration over the permafrost areas (top).

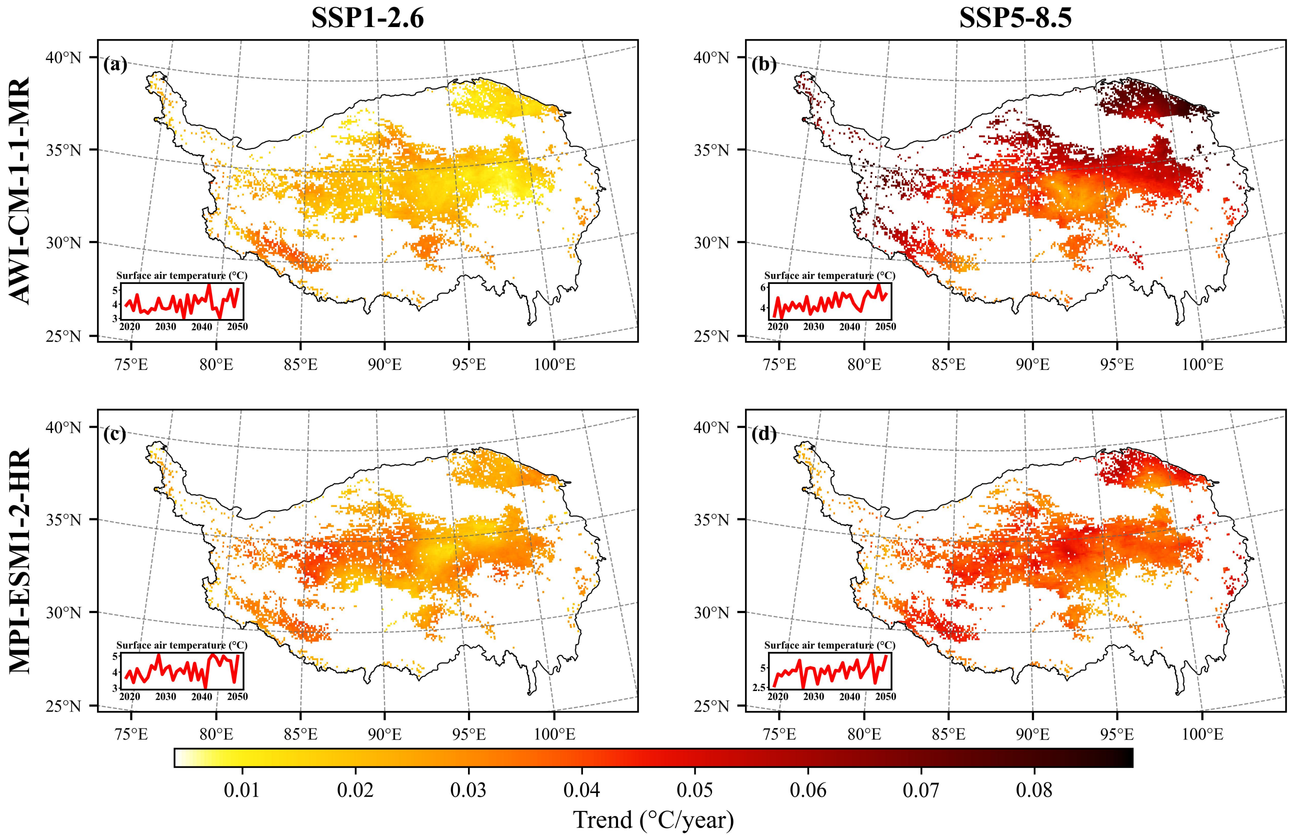

Figure S10. Spatiotemporal patterns of the changes of surface air temperature across the permafrost areas during 2019–2050 under different scenarios. (a-b) AWI-CM-1-1-MR. (c-d) MPI-ESM1-2-HR. The line plots at each subplot indicate the time series of surface air temperature.

Table S1. Overview of the CryoGridLite parameters used

Parameter	Symbol	Value	Unit	Source
Natural constants				
Atmospheric pressure at sea level	P	1.005×10^5	Pa	—
Gravitational acceleration	g	9.81	$\mathrm{m\,s^{-2}}$	—
Von Kármán constant	κ	0.4	—	—
Stefan-Boltzmann constant	σ	5.6704×10^{-8}	$\mathrm{W\,m^{-2}\,K^{-4}}$	—
Specific gas constant of air	R	287.058	$\mathrm{J^{-1}\,kg^{-1}}$	—
Surface properties				
Albedo of fresh snow	$\alpha_{\mathrm{snow,max}}$	0.82	—	Wang et al. (2020)
Albedo of old snow	$\alpha_{\mathrm{snow,min}}$	0.5	—	Westermann et al. (2016)
Albedo of soil	α_{soil}	0.20	—	Westermann et al. (2016)
Albedo of water surface	α_{water}	0.07	—	Westermann et al. (2016)
Albedo of ice	α_{ice}	0.20	—	Westermann et al. (2016)
Emissivity of snow	$\varepsilon_{\mathrm{snow}}$	0.99	—	Westermann et al. (2016)
Emissivity of soil	$\varepsilon_{\mathrm{soil}}$	0.97	—	Westermann et al. (2016)
Emissivity of water surface	$\varepsilon_{\mathrm{water}}$	0.99	—	Westermann et al. (2016)
Emissivity of ice	$\varepsilon_{\mathrm{ice}}$	0.98	—	Westermann et al. (2016)
Resistance at snow surface	$r_{\mathrm{s,snow}}$	0	$\mathrm{s\,m{-1}}$	Westermann et al. (2016)
Resistance at soil surface	$r_{\mathrm{s,soil}}$	50	$\mathrm{s\,m{-1}}$	Westermann et al. (2016)
Resistance at water surface	$r_{\mathrm{s,water}}$	0	$\mathrm{s\,m{-1}}$	Westermann et al. (2016)
Resistance at ice surface	$r_{\mathrm{s,ice}}$	0	$\mathrm{s\,m{-1}}$	Westermann et al. (2016)
Material properties				
Density of snow	ρ_{snow}	150	$\mathrm{kg\,m^{-3}}$	Dai, Che, Xie, and Wu (2018)
Density of water	ρ_{water}	1000	$\mathrm{kg\,m^{-3}}$	Westermann et al. (2016)
Density of ice	ρ_{ice}	1000	$\mathrm{kg\,m^{-3}}$	Westermann et al. (2016)
Density of air at sea level	ρ_{air}	1.293	$\mathrm{kg\,m^{-3}}$	Westermann et al. (2016)
Evaporation Depth	d_{E}	0.2	m	—
Volumetric heat capacity of water	C_{water}	4.2×10^6	$\mathrm{J\,K^{-1}\,m^{-3}}$	Westermann et al. (2016)
Volumetric heat capacity of ice	C_{ice}	1.9×10^6	$\mathrm{J\,K^{-1}\,m^{-3}}$	Westermann et al. (2016)
Volumetric heat capacity of air	C_{air}	1.25×10^3	$\mathrm{J\,K^{-1}\,m^{-3}}$	Westermann et al. (2016)
Volumetric heat capacity of mineral soil	C_{minear}	2.0×10^6	$\mathrm{J\,K^{-1}\,m^{-3}}$	Westermann et al. (2016)
Volumetric heat capacity of organic soil	C_{organic}	2.5×10^6	$\mathrm{J\,K^{-1}\,m^{-3}}$	Westermann et al. (2016)
Thermal conductivity of water	k_{water}	0.57	$\mathrm{W\,m^{-1}\,K^{-1}}$	Westermann et al. (2016)
Thermal conductivity of ice	k_{ice}	2.2	$\mathrm{W\,m^{-1}\,K^{-1}}$	Westermann et al. (2016)
Thermal conductivity of air	k_{air}	0.025	$\mathrm{W\,m^{-1}\,K^{-1}}$	Westermann et al. (2016)
Thermal conductivity of mineral soil	k_{mineral}	3.00	$\mathrm{W\,m^{-1}\,K^{-1}}$	Westermann et al. (2016)
Thermal conductivity of organic soil	k_{organic}	0.25	$\mathrm{W\,m^{-1}\,K^{-1}}$	Westermann et al. (2016)
Specific latent heat of fusion water	L_{sl}	0.334×10^6	$\mathrm{J\,kg^{-1}}$	Westermann et al. (2016)
Specific latent heat of vaporization	L_{lg}	2.501×10^6	$\mathrm{J\,kg^{-1}}$	Westermann et al. (2016)

Table S2. Overview of the hyperparameter settings for the different machine learning models

Model	Hyperparameter	Searching space	Best parameter	
			permafrost	non-permafrost
LightGBM	n_estimators	[100, 2000]	1850	1880
	max_depth	[3, 20]	19	20
	learning_rate	[0.001, 0.3]	0.062	0.069
	num_leaves	[5, 1000]	788	860
	colsample_bytree	[0.4, 1]	0.957	0.947
	subsample	[0.4, 1]	0.917	0.986
	subsample_freq	[1, 7]	4	4
	min_child_samples	[5, 100]	35	7
	reg_alpha	[1×10^{-8}, 10]	0.108	$1.037\times10-6$
	reg_lambda	[1×10^{-8}, 10]	0.002	1.463×10^{-6}
	max_bin	[255, 511]	353	290
XGBoost	n_estimators	[100, 2000]	1395	1583
	max_depth	[3, 15]	15	15
	learning_rate	[0.001, 0.3]	0.015	0.019
	min_child_weight	[1, 20]	2	14
	colsample_bytree	[0.4, 1]	0.936	0.983
	subsample	[0.4, 1]	0.878	0.763
	reg_alpha	[1×10^{-8}, 10]	1.425×10^{-6}	5.357×10^{-8}
	reg_lambda	[1×10^{-8}, 10]	3.657×10^{-4}	2.977×10^{-6}
	gamma	[1×10^{-8}, 10]	1.382×10^{-6}	5.202×10^{-6}

Note: Searching space of weight parameters for both models is from 1 to 100.

Table S3. Information on MAGT and ALT boreholes from 2000–2015 was used for validating the modeled results

Variables	Sites	Lon ($^{\circ}E$)	Lat ($^{\circ}N$)	Altitude (m)	Reference/ Source	Sites	Longitude ($^{\circ}E$)	Latitude ($^{\circ}N$)	Altitude (m)	Reference/ Source
	K512	79.39	35.86	4766	H. Chen et al. (2015)	YH	70.40	35.77	4850	H. Chen et al. (2015)
	K521	79.42	35.79	4928	Qin et al. (2017)	K572	79.46	35.72	4690	Qin et al. (2017)
	K529	79.46	35.72	4952	H. Chen et al. (2015)	MPQT	79.49	35.68	5175	H. Chen et al. (2015)
	TSH	79.55	35.36	4834	H. Chen et al. (2015)	TSHGT	79.55	35.36	—	Zhao et al. (2021)
	K610	79.64	35.08	4926	Qin et al. (2017)	SLMC	80.39	34.56	5050	H. Chen et al. (2015)
	LN2	80.39	34.63	5001	Qin et al. (2017)	NLMC	80.39	34.64	5016	H. Chen et al. (2015)
	MPJS	80.42	34.54	5117	H. Chen et al. (2015)	LZL	81.33	34.80	5009	H. Chen et al. (2015)
	LZL3	81.33	34.81	5009	Qin et al. (2017)	DLSW	84.18	33.00	4919	Qin et al. (2017)
	NO.GZ	85.13	33.80	4990	Qin et al. (2017)	GM	85.63	33.39	5095	Qin et al. (2017)
	FCKGT	88.57	37.46	—	Zhao et al. (2021)	STG	88.60	37.58	4500	Qin et al. (2017)
	AYK2	88.61	37.52	4645	Qin et al. (2017)	AYKGT	88.61	37.52	—	Zhao et al. (2021)
	AYK3	88.70	37.51	4500	Qin et al. (2017)	NO.72	91.40	33.01	4930	Qin et al. (2017)
	AD2	91.58	32.31	4814	Q. Wu et al. (2020)	NO.39	91.53	32.42	4995	Qin et al. (2017)
	TJ1	91.53	32.51	4868	Q. Wu et al. (2020)	TJ2	91.62	32.39	4887	Q. Wu et al. (2020)
	QTB18	91.74	31.82	—	Zhao et al. (2021)	TG4	91.75	33.07	4974	Q. Wu et al. (2020)
	ZNHW	91.86	35.49	4768	Qin et al. (2017)	TG3	91.80	33.09	4926	Q. Wu et al. (2020)
	TG2	91.87	33.30	4841	Q. Wu et al. (2020)	WQ	91.90	33.10	4960	Qin et al. (2017)
	TGLGT	91.94	33.07	—	Zhao et al. (2021)	WQ1	91.94	33.47	4778	Q. Wu et al. (2020)
	WQ2	91.95	33.40	4817	Q. Wu et al. (2020)	ZNHGT	91.96	35.49	—	Zhao et al. (2021)
	ZNH5	91.96	35.49	4784	Qin et al. (2017)	NO.64	92.14	33.46	4620	Qin et al. (2017)
	No.62	92.20	34.01	4680	Qin et al. (2017)	NO.61	92.26	34.13	4550	Qin et al. (2017)
	KKXL1	92.28	35.53	4701	Qin et al. (2017)	TT2	92.20	33.76	4647	Q. Wu et al. (2020)
	TT1	92.23	33.88	4640	Q. Wu et al. (2020)	KL1	92.34	34.01	4672	Q. Wu et al. (2020)
	KL3	92.34	33.96	4622	Q. Wu et al. (2020)	KL5	92.34	33.94	4622	Q. Wu et al. (2020)
	NO.59	92.44	34.29	4579	Qin et al. (2017)	NO.34	92.44	34.29	4583	Qin et al. (2017)
	NO.56	92.47	34.37	4714	Qin et al. (2017)	NO.32	92.56	34.49	4634	Qin et al. (2017)
	NO.31	92.57	34.51	4595	Qin et al. (2017)	QTB11	92.66	34.39	—	Zhao et al. (2021)
	YM2	92.73	34.53	4616	Q. Wu et al. (2020)	YM1	92.74	34.58	4654	Q. Wu et al. (2020)
MAGT	WL1	92.73	34.48	4587	Q. Wu et al. (2020)	FH3	92.78	34.61	4715	Q. Wu et al. (2020)
	FH2	92.90	34.67	4894	Q. Wu et al. (2020)	NO.11	92.93	34.82	4637	Qin et al. (2017)
	NO.9	92.95	34.85	4592	Qin et al. (2017)	KKXL3	92.96	35.48	4554	Qin et al. (2017)
	NO.54	93.02	35.04	4570	Qin et al. (2017)	NO.53	93.03	35.08	4731	Qin et al. (2017)
	NO.52	93.07	35.12	4610	Qin et al. (2017)	NO.4	93.07	35.21	4635	Qin et al. (2017)
	HR3	93.03	35.07	4675	Q. Wu et al. (2020)	WD4	93.04	35.14	4734	Q. Wu et al. (2020)
	QTB09	93.03	35.13	—	Zhao et al. (2021)	QTB08	93.08	35.22	—	Zhao et al. (2021)
	WD3	93.11	35.20	4613	Q. Wu et al. (2020)	NO.50	93.27	35.22	4510	Qin et al. (2017)
	CM7	93.22	35.28	4589	Q. Wu et al. (2020)	QTB06	93.27	35.29	—	Zhao et al. (2021)
	NO.27	93.32	35.24	4487	Qin et al. (2017)	NO.21	93.45	35.31	4568	Qin et al. (2017)
	CM5	93.45	35.36	4507	Q. Wu et al. (2020)	CM6	93.45	35.36	4504	Q. Wu et al. (2020)
	QTB05	93.45	35.36	—	Zhao et al. (2021)	NO.46	93.58	35.33	4640	Qin et al. (2017)
	NO.66	93.78	35.52	4560	Qin et al. (2017)	QTB03	93.78	35.52	—	Zhao et al. (2021)
	CM3	93.96	35.55	4547	Q. Wu et al. (2020)	BD1	93.96	35.62	4636	Q. Wu et al. (2020)
	KLS	94.06	35.63	4753	Qin et al. (2017)	KM2	94.05	35.62	4757	Q. Wu et al. (2020)
	QTB02	94.06	35.63	—	Zhao et al. (2021)	QTB01	94.08	35.72	—	Zhao et al. (2021)
	XDTGT	94.13	35.72	—	Zhao et al. (2021)	QSH-1	97.15	33.78	4413	Luo et al. (2018)
	QSH-2	97.17	33.74	4395	Luo et al. (2018)	QSH-3	97.17	33.74	4403	Luo et al. (2018)
	K634–1	97.38	33.98	4532	Luo et al. (2018)	K634–2	97.38	33.98	4536	Luo et al. (2018)
	CLQ-1	97.56	34.04	4634	Luo et al. (2018)	CLQ-2	97.57	34.04	4614	Luo et al. (2018)
	BSKN	97.65	34.11	4744	Luo et al. (2018)	BSK	97.66	34.13	4833	Luo et al. (2018)
	CLP3	97.87	34.27	4663	Qin et al. (2017)	CLP-1	97.85	34.26	4721	Luo et al. (2018)
	CLP-2	97.85	34.26	4724	Luo et al. (2018)	CLP-3	97.87	34.27	4663	Luo et al. (2018)
	CLP4	97.90	34.31	4564	Qin et al. (2017)	YNG1	97.95	34.40	4452	Qin et al. (2017)
	NO.YNP3	97.97	34.50	4333	Qin et al. (2017)	CLP-4	97.90	34.31	4564	Luo et al. (2018)
	YNG-1	97.95	34.40	4446	Luo et al. (2018)	YNG-2	97.94	34.44	4395	Luo et al. (2018)
	YNG-3	97.97	34.50	4324	Luo et al. (2018)	MDB	98.44	34.85	4225	Luo et al. (2018)
	K445	98.55	34.97	4282	Luo et al. (2018)	ZK3	99.15	35.37	4228	Qin et al. (2017)
	ZK21	99.56	35.40	4602	Qin et al. (2017)					
	K512	79.39	35.86	4766	H. Chen et al. (2015)	YH	70.40	35.77	4850	H. Chen et al. (2015)
	K529	79.46	35.72	4952	H. Chen et al. (2015)	MPQT	79.49	35.68	5175	H. Chen et al. (2015)
	TSH	79.55	35.36	4834	H. Chen et al. (2015)	SLMC	80.39	34.56	5050	H. Chen et al. (2015)
	NLMC	80.39	34.64	5016	H. Chen et al. (2015)	MPJS	80.42	34.54	5117	H. Chen et al. (2015)
	LZL	81.33	34.80	5009	H. Chen et al. (2015)	AD2	91.58	32.31	4814	Q. Wu et al. (2020)
	TJ1	91.53	32.51	4868	Q. Wu et al. (2020)	TJ2	91.62	32.39	4887	Q. Wu et al. (2020)
	TG4	91.75	33.07	4974	Q. Wu et al. (2020)	TG3	91.80	33.09	4926	Q. Wu et al. (2020)
	TG2	91.87	33.30	4841	Q. Wu et al. (2020)	WQ1	91.94	33.47	4778	Q. Wu et al. (2020)
	WQ2	91.95	33.40	4817	Q. Wu et al. (2020)	TT1	92.23	33.88	4640	Q. Wu et al. (2020)
	TT1	92.23	33.88	4640	Z. Zhang et al. (2020)	CLP1	92.35	33.96	4627	Qin et al. (2017)
	KL1	92.34	34.01	4672	Q. Wu et al. (2020)	KL3	92.34	33.96	4622	Q. Wu et al. (2020)
	KL5	92.34	33.94	4622	Q. Wu et al. (2020)	KL3	92.34	33.96	4672	Z. Zhang et al. (2020)
	YM2	92.73	34.53	4616	Q. Wu et al. (2020)	YM1	92.74	34.58	4654	Q. Wu et al. (2020)
	WL1	92.73	34.48	4587	Q. Wu et al. (2020)	FH3	92.78	34.61	4715	Q. Wu et al. (2020)
	FHS1	98.89	34.73	4896	Qin et al. (2017)	FH2	92.90	34.67	4894	Q. Wu et al. (2020)
	BLR1	92.92	34.86	4633	Qin et al. (2017)	BL1	92.93	34.83	4635	Z. Zhang et al. (2020)
	FH4	92.90	34.68	4992	Z. Zhang et al. (2020)	WD4	93.04	35.14	4734	Q. Wu et al. (2020)
	HR3	93.03	35.07	4675	Q. Wu et al. (2020)	WD4	93.04	35.14	4734	Z. Zhang et al. (2020)
	WD3	93.11	35.20	4613	Q. Wu et al. (2020)	CM7	93.22	35.28	4589	Q. Wu et al. (2020)
ALT	CM5	93.45	35.36	4507	Q. Wu et al. (2020)	CM6	93.45	35.36	4504	Q. Wu et al. (2020)
	CM5	93.45	35.36	4507	Z. Zhang et al. (2020)	KKXL	93.60	35.45	4488	Qin et al. (2017)
	BD1	93.96	35.62	4636	Q. Wu et al. (2020)	CM3	93.96	35.55	4547	Q. Wu et al. (2020)
	S308_5	94.07	35.08	4512	Qin et al. (2017)	XDT2	94.09	35.71	4530	Qin et al. (2017)
	XDT1	94.04	35.71	4602	Qin et al. (2017)	KM2	94.05	35.62	4757	Q. Wu et al. (2020)
	ZD	94.40	32.82	4775	Qin et al. (2017)	S308_4	94.79	34.90	4475	Qin et al. (2017)
	S308_3	95.19	34.68	4661	Qin et al. (2017)	S308_2	95.97	34.16	4733	Qin et al. (2017)
	S308_1	96.96	33.77	4676	Qin et al. (2017)	ZLH2	97.31	34.69	4402	Qin et al. (2017)
	GST-51	97.38	33.98	4532	Gao et al. (2023)	GST-49	97.38	33.98	4536	Gao et al. (2023)
	GST-7	97.57	35.01	4299	Gao et al. (2023)	GST-6	97.58	35.02	4299	Gao et al. (2023)
	GST-46	97.65	34.11	4749	Gao et al. (2023)	CLP2	97.85	34.26	4717	Qin et al. (2017)
	GST-37	97.85	34.26	4724	Gao et al. (2023)	GST-31	97.87	34.27	4663	Gao et al. (2023)
	GST-8	98.44	34.85	4219	Gao et al. (2023)	PT1	98.75	38.78	4128	Mu and Peng (2022)
	PT2	98.78	38.83	3985	Mu and Peng (2022)	PT3	98.85	38.84	3827	Mu and Peng (2022)
	PT4	98.95	38.83	3770	Mu and Peng (2022)	PT5	99.03	38.81	3691	Mu and Peng (2022)
	PT6	98.96	38.95	4153	Mu and Peng (2022)	PT7	98.96	38.90	3970	Mu and Peng (2022)
	PT10	99.07	38.79	3681	Mu and Peng (2022)	Ebo TA	100.92	38.00	3691	Mu and Peng (2022)
	Ebo TB	100.91	38.00	3615	Mu and Peng (2022)	KHW	99.15	35.36	4166	Qin et al. (2017)
	KHE	99.28	35.33	4338	Qin et al. (2017)	JLLW	99.33	35.40	4324	Qin et al. (2017)
	ELS	99.50	35.49	4330	Qin et al. (2017)	ZK21	85.13	33.80	5020	J. Chen et al. (2016)
	ZK13	85.31	33.18	5120	J. Chen et al. (2016)	ZK14	85.35	33.21	5130	J. Chen et al. (2016)
	ZK18	85.36	33.39	5120	J. Chen et al. (2016)	ZK15	85.63	33.39	5130	J. Chen et al. (2016)
	ZK16	85.63	33.39	5120	J. Chen et al. (2016)	ZK17	85.63	33.39	5120	J. Chen et al. (2016)
	ZK19	85.65	33.35	5050	J. Chen et al. (2016)	ZK22	85.63	33.39	5120	J. Chen et al. (2016)

Table S4. Comparison of observed and modeled soil temperature at 0–40cm depth.

Sites	Longitude (° E)	Latitude (° N)	Altitude (m)	Period	Observation (° C)		Simulation (° C)		Bias (° C)
					Mean	Std	Mean	Std	
51886	90.85	38.25	2945	1988–2012	8.3	11.4	9.8	11.3	-1.5
52602	93.33	38.75	2770	1980–2012	7.6	11.5	8.5	11.8	-0.9
52633	98.42	38.80	3367	2004–2012	2.5	9.2	2.1	8.9	0.4
52657	100.25	38.18	2787	2004–2012	5.8	9.7	3.5	9.4	2.3
52707	93.68	36.80	2767	2004–2012	9.8	10.6	10.5	11.3	-0.7
52713	95.37	37.85	3173	2004–2012	8.6	11.1	9.0	12.0	-0.4
52737	97.37	37.37	2982	1980–2012	7.2	10.1	9.6	11.3	-2.4
52754	100.13	37.33	3345	1980–2012	3.6	8.0	2.9	8.3	0.7
52765	101.62	37.38	2938	1982–2012	4.6	8.2	4.0	9.3	0.6
52825	96.42	36.43	2790	2004–2012	9.2	11.3	12.6	11.8	-3.4
52833	98.48	36.92	2950	2004–2012	8.0	10.2	8.2	10.9	-0.2
52836	98.10	36.30	3191	2004–2012	6.6	9.1	7.3	10.4	-0.7
52856	100.62	36.27	2835	1982–2012	7.9	9.4	9.4	9.8	-1.5
52943	99.98	35.58	3323	1992–2012	5.5	8.1	7.5	8.6	-2.0
52955	100.75	35.58	3203	2004–2012	6.2	9.1	6.4	9.0	-0.2
52974	102.02	35.52	2491	2004–2012	9.1	8.7	11.1	9.0	-2.0
55228	79.59	32.11	4279	1994–2012	6.8	10.8	5.6	10.8	1.2
55248	84.25	32.09	4415	2007–2012	5.5	8.9	7.8	9.7	-2.3
55279	89.40	31.48	4700	2007–2012	4.6	7.0	5.3	7.8	-0.7
55294	91.06	32.21	4800	2006–2012	3.3	7.5	4.0	7.3	-0.7
55299	92.16	32.06	4507	2006-2012	4.8	7.0	-0.5	5.5	5.3
55437	81.15	30.17	4900	1994–2012	10.4	8.8	6.7	9.2	3.7
55472	83.8	30.57	4672	2007–2012	5.4	8.2	1.7	7.3	2.7
55493	91.05	30.29	4200	2006–2012	7.7	7.2	7.1	7.5	0.6
55569	87.38	29.05	4000	2007–2012	11.9	7.2	6.1	7.5	5.8
56021	95.78	34.13	4175	1982–2012	3.1	7.7	2.7	7.8	0.4
56029	97.02	33.02	3681	2004–2012	7.3	7.5	6.8	8.0	0.5
56033	98.22	34.92	4272	1980–2012	1.5	7.6	-0.9	8.6	2.4
56034	97.13	33.80	4415	2004–2012	1.5	6.5	-0.4	7.1	1.9
56043	100.25	34.47	3719	2004–2012	4.5	7.3	4.6	6.3	-0.1
56065	101.60	34.73	3670	1981–2012	3.9	7.0	3.0	8.4	0.9
56125	96.48	32.20	3644	1993–2012	8.6	7.3	6.8	7.9	1.8
56151	100.75	32.93	3530	2004–2012	7.2	7.1	5.5	7.7	1.7
56434	97.28	28.39	2328	2007–2012	15.0	5.9	7.4	4.9	7.6
S6	89.47	28.30	4450	2018	4.9	7.4	6.8	5.9	-1.9
S9	94.43	29.54	2992	2018	10.1	6.2	13.5	5.2	-3.4

Note: Study sites were selected based on their location and the observational periods. These sites need to be located in our model domain and within the period of historical simulation. Data derived from Cuo, Zhang, and Li (2022).

Table S5. Comparison of the average thermal state permafrost and active layer thickness over the Tibetan Plateau between this study and other research

Variables	Historical period	Mid-century				End-century				Methods	Reference
		SSP1-2.6 /RCP2.6	SSP2-4.5 /RCP4.5	SSP3-7.0 /RCP7.0	SSP5-8.5 /RCP8.5	SSP1-2.6 /RCP2.6	SSP2-4.5 /RCP4.5	SSP3-7.0 /RCP6.0	SSP5-8.5 /RCP8.5		
MAGT ($^\circ C$)	**-2.26±0.17**	**-2.33±0.20**	—	—	**-1.98±0.17**	**-2.52±0.18**	—	—	**-1.06±0.12**	**TNM**	**this study**
	-1.35±0.42	—	—	—	—	-0.66	-0.14	—	0.25	ML	Ni et al. (2021)
	-1.56	—	—	—	—	—	—	—	—	TNM	X. Wu et al. (2018)
	-1.72	-0.43	-0.17	0.02	0.33	-0.43	0.65	1.93	2.96	ML&EQM	Ran et al. (2022)
	-3.32	—	—	—	—	—	-2.52	-1.32	-0.72	TNM	G. Zhang et al. (2022)
ALT (m)	**3.04±0.09**	**3.07±0.18**	—	—	**3.41±0.19**	**2.80±0.14**	—	—	**4.91±0.29**	**TNM**	**this study**
	2.01	—	—	—	—	—	—	—	—	TNM	Guo and Wang (2013)
	2.30±0.60	—	—	—	—	2.50	2.50	—	2.70	ML	Ni et al. (2021)
	3.23	—	—	—	—	—	—	—	—	TNM	X. Wu et al. (2018)
	2.46	—	—	—	—	—	—	—	—	EQM	Xu and Wu (2021)
	1.35±0.33	—	—	—	—	—	—	—	—	TNM	Yin et al. (2021)
	2.11	2.65	2.74	2.80	2.90	2.65	3.00	3.42	3.73	ML&EQM	Ran et al. (2022)
	1.24	—	—	—	—	—	1.94	2.74	4.24	TNM	G. Zhang et al. (2022)
	2.54	—	—	—	—	2.78	2.95	—	3.91	EQM	Ji et al. (2022)
	2.43	—	—	—	—	—	—	—	—	ML	R. Li et al. (2023)
	2.39	—	—	—	—	—	—	—	—	ML&EQM	Shen et al. (2023)
PA ($\times 10^6 km^2$)	**1.10±0.02**	**0.96±0.03**	—	—	**0.92±0.04**	**0.88±0.04**	—	—	**0.59±0.06**	**TNM**	**this study**
	1.52									TNM	Guo and Wang (2013)
	1.24±0.03	—	—	—	—	0.67±0.13	0.40±0.11	0.34±0.12	0.09±0.06	EQM	Guo and Wang (2016)
	1.48	1.09	0.96	0.96	0.78	1.10	0.88	0.80	0.55	EQM	W. Zhang et al. (2016)
	1.66	1.26	1.12	1.21	0.97	1.29	0.93	0.89	0.59	EQM	Lu et al. (2017)
	1.06									EQM	Zou et al. (2017)
	1.27	1.06	1.01	1.12	0.93	1.06	0.85	0.87	0.53	EQM	Chang et al. (2018)
	1.29	—	—	—	—	—	—	—	—	TNM	X. Wu et al. (2018)
	1.11	—	—	—	—	—	—	—	—	EQM	Ran et al. (2018)
	1.04	—	—	—	—	0.91	0.62	—	0.44	ML	Ni et al. (2021)
	1.15	—	—	—	—	—	—	—	—	ML	Ran et al. (2021)
	1.42	—	—	—	—	1.04	0.57	—	0.28	TNM	Yin et al. (2021)
	1.01	—	—	—	—	—	—	—	—	ML&EQM	Ran et al. (2022)
	1.07	0.85	0.85	0.83	0.79	0.77	0.60	0.44	0.31	TNM	G. Zhang et al. (2022)
	1.34	—	—	—	—	—	—	—	—	ML	R. Li et al. (2023)
	1.04	—	—	—	—	—	—	—	—	ML&EQM	Shen et al. (2023)
	1.21±0.02	0.81±0.04	0.72±0.04	0.68±0.04	0.57±0.05	0.76±0.05	0.44±0.06	0.14±0.04	0.04±0.03	EQM	H. Li et al. (2024)

Note: The abbreviations MAGT, ALT, PA, TNM, EQM, and ML refer to mean annual ground temperature, active layer thickness, permafrost areas, transient numerical model, empirical equilibrium model, and machine learning algorithm, respectively. This study defines the historical period (2000–2018), mid-century (2041–2060), and end-century (2081–2100). Different studies have various definitions.